DISSERTATION

ADVANCES IN SINGLE-PIXEL IMAGING TOWARD BIOLOGICAL APPLICATIONS

Submitted by

David G. Winters

Department of Electrical & Computer Engineering

In partial fulfillment of the requirements

For the Degree of Doctor of Philosophy

Colorado State University

Fort Collins, Colorado

Summer 2014

Doctoral Committee:

Advisor: Randy Bartels

Mario C. Marconi
Ashok Prasad
Elliot R. Bernstein

ABSTRACT

ADVANCES IN SINGLE-PIXEL IMAGING TOWARD BIOLOGICAL APPLICATIONS

In this work, we discuss two new methods for single-pixel imaging. First, we leverage advances in laser metrology and frequency synthesis to measure small shifts in the center frequency of an optical pulse. Pulses acquire such shifts when probing a transient optical susceptibility, as in impulsive stimulated Raman scattering, which we use to demonstrate the technique. We analyze the limits of this technique with regard to fundamental noise, and predict detection sensitivity in these limiting cases.

We then present work on imaging in two dimensions, both x–y and x–z, using single element detectors. We accomplish this by multiplexing spatial frequency projections in time, allowing rapid two dimensional imaging without an imaging detector. As we eliminate the imaging detector, the sensitivity to scattering is dramatically decreased, allowing the method to be used deep in scattering tissue. Results are shown for several geometries and experimental configurations, demonstrating imaging capabilities across a variety of sample types, including fluorescent and biological samples.

ACKNOWLEDGEMENTS

I would first like to thank my adviser, Randy Bartels, for his guidance and inspiration on the projects described in this manuscript — among many others. It has been a pleasure to pursue this work in his research group and to learn from him. I would also like to thank my committee, Mario Marconi, Ashok Prasad, and Elliot Bernstein, for their time in reviewing this manuscript and hearing my defense.

Many people contributed to the work described herein. Jeff Field worked extensively on CHIRPED, both in the theoretical framework and in data collection. Much of this work was also enabled by Philip Schlup, who spent countless hours aiding me on my many projects, and was instrumental in shaping how I work in the lab. Greg Futia laid much of the groundwork for the SPIFI experiments described here in his work on the theory and demonstration of absorptive SPIFI imaging, as well as his role in SPIFI fluorescence. Dan Higley contributed a great deal to the line-camera 2D SPIFI setup and measurements of scattering immunity. I am also grateful to Dr. Brian Kolner who provided invaluable advice on the measurement of RF phase noise.

Finally, none of this work would have been possible without the support of my family. I am especially thankful to my wife, Shannon, without whose support and encouragement this document may never have been written.

DEDICATION

for Shannon

TABLE OF CONTENTS

LIST OF FIGURES

CHAPTER 1

INTRODUCTION

In this document, we present work done in two areas of optical imaging: the measurement of small optical frequency shifts with application to high-sensitivity Raman measurements and rapid one and two dimensional imaging with single element detectors by frequency multiplexing spatial information. While these technologies appear disparate, both techniques endeavor to expand the applicability of optical imaging to a wider range of biological problems.

Raman scattering is an attractive technology for the characterization of chemical samples, as it is an endogenous contrast method which does not require the application of dyes or tags to allow chemically specific imaging. Raman measurements also have excellent specificity, as the Raman spectrum gives information about the vibrational modes of a molecule, the molecule can be identified by its Raman spectrum. A notable disadvantage of Raman measurements, however, is the weak nature of the interaction leading to long acquisition times and low sensitivity. Coherent techniques have made great strides in improving the sensitivity, yet the sensitivity is still too low to probe many interesting biological systems.

In this work, we approach Raman measurements from a new direction. Instead of probing the nuclear vibrations, as is often done, we'll make a measurement of the electronic response of the atom to a driving electric field. This electronic response gives rise to a time-dependent index of refraction, which when sampled by an optical pulse, leads to a small shift in the center optical frequency of the probe pulse. So, the problem of measuring small concentrations of Raman active molecules turns to the measurement of small optical frequency shifts.

The simplest method would be to observe the shift in the center wavelength of the pulse on an optical spectrometer. Optical Spectrum Analyzer (OSA) have a maximum resolution of

about 1 GHz, too coarse for the Raman measurements we wish to make in this work. Therefore, we need to convert this optical frequency shift into a more easily measurable quantity.

We can easily convert shifts in center frequency of the optical pulse into changes in intensity through a narrow optical filter. This filtering converts the optical frequency change into a small change in optical power, which can be measured accurately using a balanced photo detector. We'll examine the measurement of such signals, including the implication of noise to the sensitivity limit.

To obtain better performance in the face of shot noise, we look to convert the shift in center wavelength of a pulse train to a delay in time (by propagation in a dispersive medium, that is, one in which different colors travel at different speeds), rather than a change in power. The measurement of timing jitter in laser oscillators is a mature and growing field of research, which already possesses the capability to measure extremely small timing jitter values. We'll consider again the application of this technique in the presence of experimental noise, and demonstrate the viability of this technique subject to our current, experimentally imposed, sensitivity limits. Projections will also be made, showing a road map for sensitivity improvement using this technique by improving the experimental setup.

This Raman measurement technique will be implemented as a laser-scanning microscope, in which a single focal spot is raster scanned across the sample, acquiring an image point by point. This is a slow process, but works well in the presence of optical scattering, as we often find in biological specimens. We also look for an approach to increase imaging speed while still using a single-pixel detector to retain the ability to image in the presence of scattering.

Our single-pixel imaging method employs a spinning disk, on which is printed a modulation pattern with a modulation frequency that depends on radial position. Thus, when the entire

beam is collected on a single detector in space, the electronic spectrum of the photodiode signal contains a spread of frequencies, the positions of which map to spatial position and the amplitude of which give object contrast information. We'll show the basic technique of line imaging using a point detector, using both absorptive and fluorescent contrast, as well as application of our linear measurement technique to an optical spectrometer. With different wavelengths modulated at different frequencies, we can not only measure the pulse spectrum on a single element detector, but also perform hyperspectral imaging by rapidly collecting the spectrum of a single image point in a laser scanning technique.

With the one dimensional case demonstrated, we move to application of the technique to two dimensions. The introduction of a second modulator allows two dimensional x–y images to be collected using a single element, using a method analogous to the 1D case. Theory and experiment will be presented on this system, as well as a discussion of experimental considerations and alternate processing methods that can be employed to improve implementation of such a system. Operation of a 2D modulation imaging system is also demonstrated using an alternate modulator, a micro-mirror array.

The final application of this technology is also to two dimensional imaging, however, we now collect x–z images using again a single modulator. This allows the collection of not only transverse information from a line focus, but simultaneous collection of axial information along the beam propagation direction, while still using a simple optical setup. This technique is applicable not only to absorptive contrast, but also to linear and nonlinear fluorescence. As optical frequencies are too high to be directly detected, the phase of optical fields is typically detected using holography, which measures the interference between the field of interest and a reference field, and from this interference the phase difference can be

determined [1, 2]. However, this interference requires coherence between the two fields, which limits its application to the incoherent fields produced by fluorescence. Our modulation imaging technique encodes the propagation phase of the coherent illumination beam in the fluorescence intensity. The propagation phase of the coherent illumination beam can then be recovered and processed using standard holography techniques.

CHAPTER 2

Raman Scattering

Raman scattering is a light matter interaction where a photon is inelastically scattered from a molecule, such that the scattered photon has a different optical frequency than the incident photon. While the vast majority of scattering events do not cause this change in frequency, occasionally a scattered photon will leave the molecule in a higher ro-vibrational state than before the scattering, causing the scattered photon to have an energy lower than the incident photon by the energy of the ro-vibrational state. This is called Stokes Raman scattering. The photon may also be scattered by a molecule already in an excited ro-vibrational state and leave that molecule in a lower energy state, causing the scattered photon energy to be the sum of the incident energy and the energy of the ro-vibrational state energy, a process known as anti-Stokes Raman scattering. The probability of anti-Stokes scattering is comparatively less than that of Stokes Raman scattering since higher ro-vibrational states are less populated, according to Boltzmann statistics.

By illuminating a molecule with light of a single frequency, and measuring the spectrum of the light scattered from the material, the energy of the ro-vibrational states can be determined by the energy difference between the incident light and the light scattered to various Stokes and anti-Stokes lines. As the incident photon energy need not correspond to any energy level of the molecule, this measurement can be made with any illumination frequency. At frequencies far from electronic resonance, these spontaneous Raman lines are very weak and measurement requires high illumination intensities and long integration times, ultimately limited by the experimental background from sources such as scattered light and fluorescence.

If the laser frequency is close to an electronic energy level of the system being studied, the Raman scattering can be enhanced [3].

2.1. Stimulated Raman Scattering

To improve the signal strength, Raman scattering events can be stimulated instead of relying upon spontaneous scattering. In this method, the molecule is illuminated with light at two frequencies, separated by the ro-vibrational frequency of interest. The intensity of the coherently scattered Stokes light is proportional to the product of the intensity of the pump and Stokes beams [4]. To measure the Raman spectrum, one laser is typically fixed while the other is swept through a range of optical frequencies. When the difference between the two frequencies corresponds to a ro-vibrational mode of the molecule, the measurement will show an increase in power in the Stokes beam, Stimulated Raman Gain (SRG), and a corresponding decrease in the power in the pump beam, Stimulated Raman Loss (SRL). When the frequency difference does not correspond to a vibrational mode, both beams are unperturbed. These effects are collectively known as Stimulated Raman Scattering (SRS). As the gain and loss signals are small changes in power against the background of intense pump or stokes beams, the signals can get lost in the laser and measurement noise.

A similar method can be used which still illuminates the sample with a pump and Stokes beam, but produces the signal of interest at a third frequency. In this case, the sample is illuminated with light of two frequencies, ω_1 and ω_2, where $\omega_1 > \omega_2$. If the sample has a ro-vibrational frequency of ω_{M}, Stokes and anti-Stokes frequencies can be generated when $\omega_1 - \omega_2 = \omega_{\mathrm{M}}$, in a 4-wave mixing process [5]. A strong Stokes signal at $\omega_2 - \omega_{\mathrm{M}}$ is generated when $2\omega_2 - \omega_1$, a process known as Coherent Stokes Raman Scattering (CSRS). A strong anti-Stokes signal at $\omega_1 + \omega_{\mathrm{M}}$ is generated when $2\omega_1 - \omega_2$ in a process called Coherent

Anti-Stokes Raman Scattering (CARS). In both of these cases energy is conserved between the incident and generated photons, causing no net change in the energy of the sample.

While a CARS measurement of the transition encodes the vibrational energy of the molecule in the output beam at a new frequency, $\omega_1 + \omega_M$, there is still a significant background contribution that does not contain the desired information. This contribution is generated from interaction between the fields and electronic and nonresonant vibrational modes [6]. The challenge in achieving high sensitivity in CARS microscopy is thus differentiation between the resonant CARS signal and the non resonant background. Numerous methods exist to suppress the non-resonant background, including through polarization [7], destructive interference [8], and frequency modulation [9]. With the background suppression available through Frequency-Modulated CARS (FM-CARS), CARS microscopy has been able to detect as few as 500000 molecules in a 100 attoliter focal volume with a 1.6 Hz update rate [9]. While this method represents an orders of magnitude improvement in CARS sensitivity, SRS has recently been shown to have the highest sensitivity [10], where as few as 300,000 methanol (5 mM) or 3,000 retinol (50 μM) molecules were measured in a ~100 attoliter volume [11].

2.2. Impulsive Stimulated Raman Scattering

To achieve higher sensitivity, we turn to a different coherent Raman approach, where a short pulse is used to provide a large number of optical frequencies at the same time, exciting all Raman transitions with vibrational periods longer than the pulse duration. In this way, Raman scattering can occur driven by different colors within the same pulse. This technique, called Impulsive Stimulated Raman Scattering (ISRS), creates a vibration coherence in the molecule which leads to small, time dependant changes in the index of refraction [12]. Selectivity of the coherent excitation can be improved by shaping femtosecond pulses, either

to create multiple pulse bursts at the desired frequency to drive strong interactions [13] or using an appropriately shaped single pulse [14] to excite a specific mode.

This transient index of refraction can be measured by filtering the probe spectrum and observing the change in power through the filter as a function of pump probe delay, or by introducing a reference beam and measuring the phase change directly, again as a function of pump probe delay, using an interferometer [15]. This phase can also be recovered through spectral interferometry [16] in a pump-probe configuration, or without scanning by employing chirped probe pulses [17] to probe low-frequency Raman modes.

Traditional Raman scattering looks at light scattered by the molecular nuclear vibration. In this work, we look at the phase shift of a laser pulse interacting with the moving electronic cloud of the molecules of interest. The moving charge density changes the index of refraction as a function of time, leading to both phase and frequency shifts that are imposed on a laser pulse propagating through the sample. The frequency shift depends not only on the vibrational oscillation frequency but also on the velocity of vibrational motion. Among other effects, the atomic displacement leads to a change of the molecule's polarizability, which characterizes the displacement of electrons in a molecule in response to an applied electric field. The magnitude of the frequency shift is proportional to the molecular concentration and the intensity of the pump pulse.

2.3. Susceptibility perturbation

Considering excitation by a short pulse, in which a superposition of modes will be excited, for which the pulse is shorter than the vibrational period. The autocorrelation of the pulse spectrum determines the mode excitation [14], with pairs of different colors from within the bandwidth driving a coherence at their difference frequency. This gives a perturbation to

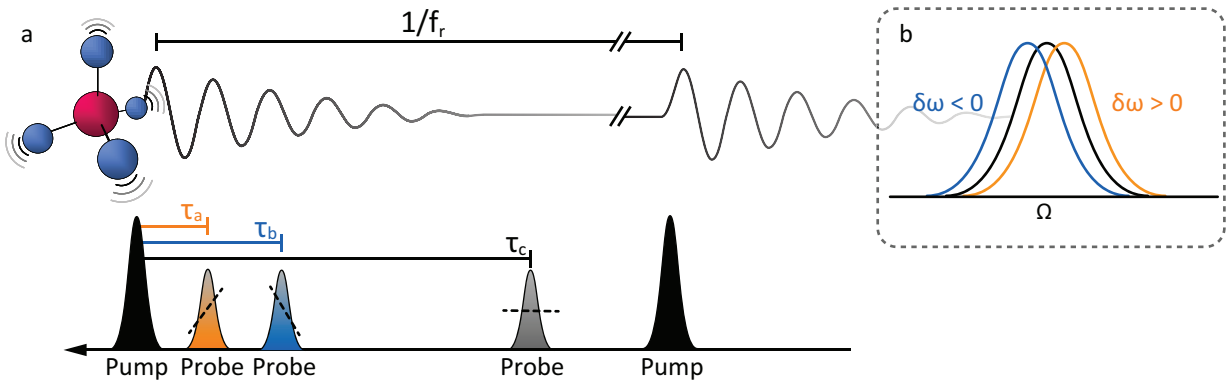

FIGURE 2.1. Schematic depiction of the molecular coherence giving rise to a transient index of refraction. (a) The transient index is then sampled by a probe pulse that arrives after the pump at a variable time τ. (b) The transient index gives rise to temporal phase across the pulse duration, which can be seen as a shift in the center frequency of the pulse.

the effective optical susceptibility in response to each pulse (quasi-Gaussian approximation) given by [18]

$$\delta\chi^{(1)}(\zeta,t;\tau) \approx \frac{N}{\varepsilon_0}(\alpha')^2\frac{1}{\Omega_v}\left|D\left(\Omega_v\right)\right|\sin\left(\Omega_v(t+\tau)+\phi_0\right)\Phi(\zeta) \tag{2.1}$$

with

$$D\left(\Omega_v\right) = \int_{-\infty}^{\infty}\left|E_{\mathrm{pu}}(t)\right|^2 e^{-\iota\Omega_v t}\mathrm{d}t \equiv \left|D\left(\Omega_v\right)\right| e^{\iota\phi_0} \tag{2.2}$$

in units of $\mathrm{V}^2\,\mathrm{m}^{-2}\,\mathrm{s}$, where $\Phi(\zeta) = \left|A(\zeta)\right|^{-2}$, $A(\zeta) = 1 - \iota\left(\frac{\zeta - z_w}{z_R}\right)$, N is the number density of harmonic oscillators, ε_0 is the permittivity of free space, α' is the Raman differential polarizability, Ω_v is the vibrational frequency, and τ is the pump probe delay. E_{pu} is the temporal amplitude profile of the pump pulse.

For a medium of length ℓ with a linear refractive index n in the presence of this susceptibility perturbation, the phase shift picked up in the focus (neglecting ζ dependence) by a probe of center angular frequency ω at a delay τ relative to the pump pulse, as depicted in

Fig. 2.1, can be written as

$$\delta\phi(t;\tau) = \delta\phi_0 \sin\left(\Omega_v(t-\tau) + \phi_0\right). \tag{2.3}$$

where we've defined

$$\delta\phi_0 = \frac{\omega\ell}{2nc}\frac{N}{\varepsilon_0}(\alpha')^2\frac{1}{\Omega_v}\left|D\left(\Omega_v\right)\right|. \tag{2.4}$$

This index perturbation will lead to a change in the center frequency of the probe pulse given by the temporal derivative

$$\begin{aligned}\delta\omega(\tau) &= \frac{\mathrm{d}\phi(t;\tau)}{\mathrm{d}t} \\ &\approx \delta\phi_0\Omega_v \cos\left(\Omega_v(t-\tau) + \phi_0\right).\end{aligned} \tag{2.5}$$

The magnitude of this frequency shift can be seen to be proportional not only to the vibrational frequency Ω_v, but also to the number density N of the species, as well as the Raman differential polarizability. This continuous frequency shift is distinct from the typical Raman scattering in which the center wavelength of the scattered light is shifted by the vibrational frequency, producing Stokes and anti-Stokes spectral sidebands. Measuring a pump-probe delay scan to map out this cosine dependence allows for determination of the vibrational frequency, with the magnitude of the frequency shift providing information about number density. From the frequency shift, we can compute the peak change in index of refraction, allowing the determination of molecular concentration.

As this frequency shift is born of time-dependent phase that arises from the index perturbation created by this vibrational coherence, and that the vibrational coherence is relatively short lived (dephasing typically within a few ps), such that each probe pulse sees a freshly

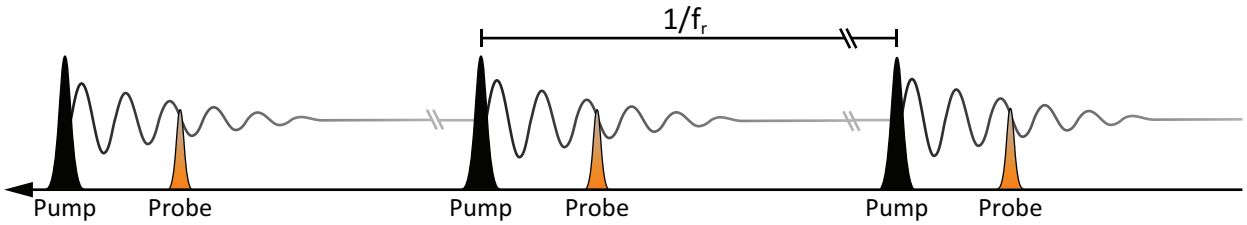

FIGURE 2.2. Pump pulses at repetition rate f_r set up coherent oscillations which decay rapidly compared to the temporal separation of the pulses. The probe pulses arrive delayed slightly from the pump pulses, each sampling a freshly constructed coherence.

prepared coherence (as the pulse separation is on the order of nanoseconds), as depicted schematically in Fig. 2.2. Thus, there is no coherence between pulses in the pulse train; each pulse pair performs an independent experiment. Each pulse sees an identically prepared perturbation that does not evolve pulse to pulse. This presents a challenge for measurement.

The simplest approach to measuring this constant change in the center frequency of the pulse is to observe the spectral change using an optical spectrometer. The resolution of optical spectrometers, however, is typically on the order of GHz, severely limiting the concentrations that can be observed. Another common method of accurate frequency determination is interferometry. While this is commonly employed with Constant Wave (CW) light, this technique cannot be applied in our case as it would require a change in offset frequency or repetition rate to get a heterodyne beat. As shown in Fig. 2.3, in our experiment the pulse envelope shifts relative to the comb, so the energy in each comb line changes but the comb lines are fixed by the laser. This is distinct from the type of shift that would be applied by an Acousto-Optic Modulator (AOM), for example, as the AOM adds an offset frequency, shifting both the envelope and the underlying comb structure.

While the change in optical path from the a modulated index of refraction and from a moving particle look the same when sampled by a CW field, when sampled using short pulses the effects are seen to be quite different. In Doppler Optical Coherence Tomography (OCT)

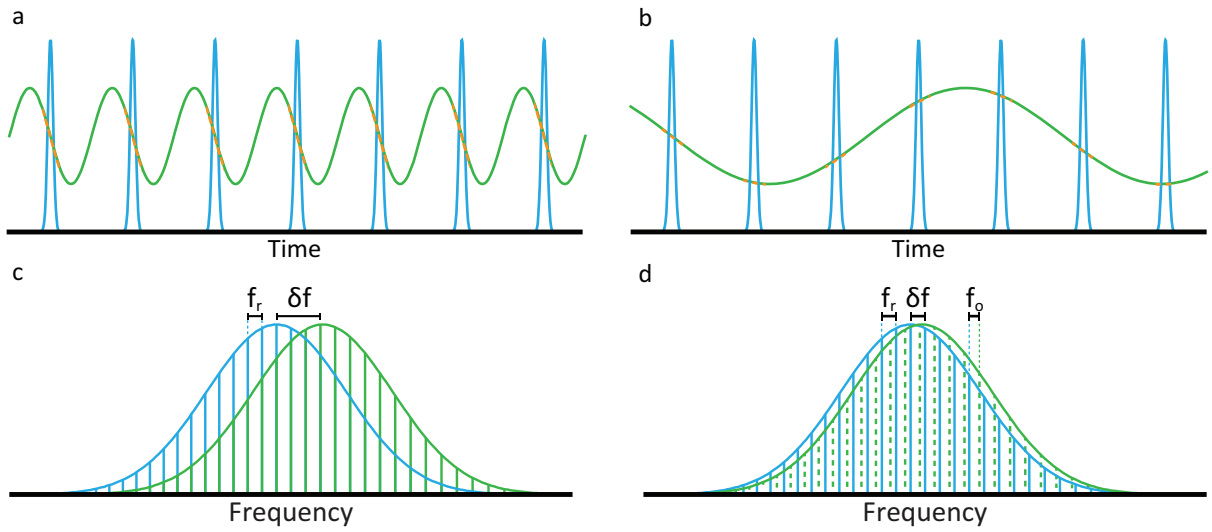

FIGURE 2.3. Two temporal pulse trains shown with phase modulations that (a) are the same for each pulse and (b) vary from pulse to pulse. This phase shifts the pulse spectrum relative to comb lines for (c) the modulation that is the same for each pulse and (d) a slow phase change that leads to shift in offset frequency f_o (e.g., from an AOM).

[19], small frequency shifts born of moving particles are measured using an interferometer. However, when attempting to measure a shift brought about by a changing index of refraction that applies the same modulation to each pulse in the train, such interferometric measurements prove ineffective.

Optical Path Length and the Generalized Doppler Shift. The effect of time varying inhomogeneous media on frequency has been considered for the case of Radio Frequency (RF) pulses in which the path length fluctuates slowly compare to pulse duration in the theory of the so-called Generalized Doppler effect [20]. Work has been done on the Doppler shift of laser pulses scattered by an inhomogeneous material [21]. Here, we'll look at Doppler shifts for both the case of time varying media and moving particles under both CW and pulsed laser illumination.

Starting with the optical path length, defined by OPL $= nL$, we calculate the time-derivative as

$$\frac{\mathrm{dOPL}}{\mathrm{d}t} = n\frac{\partial L}{\partial t} + \frac{\partial n}{\partial t}L, \tag{2.6}$$

where the change in optical path is the sum of two terms. The first term looks like a moving object, with length changing as a function of time, and the second term is a time-varying index of refraction, as we'll see from the Raman-induced index perturbation. These two effects require different detection techniques, when measuring the changing path length or the changing index of refraction. The method also depends on whether the field being used to measure the effect are CW or pulses.

For the CW case, measurement of the two quantities is equivalent. Consider the light backscattered from particles moving at a uniform velocity, where we can write the path length as a function of time as $L(t) = L_0 + v_z t$, and movement through a medium with a uniform index change (e.g., linear index change: $n(t) = n_0 + n't$). We write the change in optical path as

$$\frac{\mathrm{dOPL}}{\mathrm{d}t} = n_0 v_z t + n' L_0 t = (n_0 v_z + n' L_0)\, t. \tag{2.7}$$

This linear change in OPL gives rise to a frequency shift that can be written as

$$\delta\omega = -\frac{\omega}{c}\,(n_0 v_z + n' L_0)\,. \tag{2.8}$$

The contribution from moving particles takes the same form as the changing index of refraction. This frequency shifted field can then be mixed with an unshifted beam, allowing the determination of the frequency shift from the heterodyne beat signal, using for example

a Michelson interferometer. However, with short pulses, the measurement becomes more complicated.

Interferometry with Frequency-Shifted Pulses. To examine the impact of short pulses on the measurement, we look at the cross-correlation of a reference pulse and a frequency-shifted pulse. We will look at both the case of a changing physical propagation distance as well as scattering from a moving particle. Doppler OCT, for example, is just an effective time-varying distance to the scattering point, an thus, we need only compute the cross-correlation signal.

We will have a reference pulse that will be scanned with a delay τ relative to the frequency-shifted pulse. The representation of the pulses in the reference pulse train is given by

$$E_{\text{ref}}(t) = \sum_{n=-\infty}^{\infty} E_r\left(t - \frac{n}{f_{\text{rep}}}\right) \exp\left(\iota\omega_0 t\right) + \text{c.c.} \tag{2.9}$$

where E_p is the pulse envelope, ω_0 is the center frequency, and c.c. is the complex conjugate. The modulated pulse train is given by

$$E_{\text{mod}}(t) = \sum_{n=-\infty}^{\infty} E_s\left(t - \frac{n}{f_{\text{rep}}}\right) \exp\left(\iota\omega_0 t\right) + \text{c.c.}. \tag{2.10}$$

We'll measure the output signal of a Michelson interferometer to observe the modulation. For femtosecond pulses, the current pulses from the detector are the detector impulse response scaled by the pulse energy. A slow detector (i.e., with a bandwidth $< f_{\text{rep}}$) will provide a signal that corresponds to the average intensity of the pulse train $\bar{I}_j$

$$\langle I_{\text{inst}} \rangle = \bar{I}_s + \bar{I}_R + f_r 2\text{Re}\left[\Gamma\left(T_d\right)\right] \tag{2.11}$$

where the correlation function is given by

$$\Gamma(\tau) = \int_{-\infty}^{\infty} \hat{E}_p(\omega - \omega_0)\, \hat{E}_r^*(\omega - \omega_0 - \delta\omega(\tau)) \exp(\iota\omega\tau)\, \mathrm{d}\omega. \tag{2.12}$$

This intensity will show a difference with changes to the pulse parameters involved in the cross correlation measurement. For the case of slowly varying changes, those that vary from pulse-to-pulse, we can write the modulated pulse train as

$$E_{\mathrm{mod}}(t) = m(t) \sum_{n=-\infty}^{\infty} E_p\left(t - \frac{n}{f_r}\right) \exp(\iota\omega_0 t) \tag{2.13}$$

where $m(t) = a(t)e^{i\theta(t)}$, with $a(t)$ and $\theta(t)$ are the amplitude and phase modulation of the pulse train, respectively. This leads to an average intensity of

$$\langle I_{\mathrm{inst}} \rangle = \bar{I}_s + \bar{I}_R + 2f_r a(t) \mathrm{Re}\left[\Gamma(\tau)\, e^{i\theta(t)}\right], \tag{2.14}$$

assuming the modulation, $m(t)$ and $\theta(t)$, vary slowly relative to bandwidth of the optical detector. In this case, we can see that the modulation is faithfully transferred from the optical pulse train to the intensity signal. For the case of a moving scatterer with a uniform velocity along z of v_z, the modulated field takes the form of

$$E_{\mathrm{mod}}(t) = \exp\left(\iota\frac{\omega}{c} 2v_z t\right) \sum_{n=-\infty}^{\infty} E_p\left(t - \frac{n}{f_r} - \frac{2v_z}{c} t\right) \exp(\iota\omega_0 t)\,. \tag{2.15}$$

The intensity can be written in terms of the effective delay, $\tau \to \tau + \frac{2v_z}{c} t$, as

$$\langle I_{\mathrm{inst}} \rangle = \bar{I}_s + \bar{I}_R + 2f_r \mathrm{Re}\left[\Gamma\left(\tau + \frac{2v_z}{c} t\right) \exp\left(\iota\frac{\omega}{c} 2v_z t\right)\right] \tag{2.16}$$

So in the case of the moving particle, we see again a modulation in the intensity signal encoded directly in the intensity signal.

Lastly, we'll look at the modulation that is pertinent to this work, in which the amplitude and phase modulation is the same for each pulse in the pulse train. Again writing the modulated pulse train,

$$E_{\mathrm{mod}}(t) = \sum_{n=-\infty}^{\infty} E_p\left(t - \frac{n}{f_r}\right) \exp\left[-\imath\delta\omega(\tau)\left(t - \frac{n}{f_r}\right)\right] \exp\left[-\imath\delta\phi(\tau)\right] \exp\left(\imath\omega_0 t\right) \tag{2.17}$$

which allows us to write the correlation function of

$$\Gamma\left(\tau\right) = e^{-\imath\delta\phi(\tau)} \int_{-\infty}^{\infty} \hat{E}_p\left(\omega - \omega_0\right) \hat{E}_p^*\left(\omega - \omega_0 - \delta\omega(\tau)\right) \exp\left(\imath\omega\tau\right) \mathrm{d}\omega. \tag{2.18}$$

Substituting $\Omega = \omega - \omega_0 - \frac{\delta\omega}{2}$ and defining

$$\eta\left(\tau\right) = \int_{-\infty}^{\infty} \hat{E}_p\left(\Omega + \frac{\delta\omega}{2}\right) \hat{E}_p^*\left(\Omega - \frac{\delta\omega}{2}\right) \exp\left(\imath\Omega\tau\right) \mathrm{d}\Omega \tag{2.19}$$

gives a correlation function

$$\Gamma\left(\tau\right) = \eta\left(\tau\right) \exp\left[\imath\left(\omega_0 + \frac{\delta\omega}{2}\right)\tau - \imath\delta\phi\right]. \tag{2.20}$$

The intensity is then given by

$$\langle I_{\mathrm{inst}}\rangle = \bar{I}_s + \bar{I}_R + f_r 2\left|\eta\left(\tau\right)\right| \cos\left[\left(\omega_0 + \frac{\delta\omega}{2}\right)\tau - \delta\phi + \angle\eta\left(\tau\right)\right] \tag{2.21}$$

Here the intensity has information about the vibrational coherence encoded in the phase $\delta\phi(\tau)$ of the interferogram or a change in the carrier frequency, but this effect will be very

small. Note that any dispersion, $\varphi(\Omega)$ will be the same for each pulse in our experiment, $\exp(\imath\varphi(\Omega))$, so in the cross correlation, the phase drops out, $\exp(\imath\varphi(\Omega))\exp(-\imath\varphi(\Omega)) = 1$, so that the cross-correlation depends only on the power spectrum and is independent of the dispersion placed after any frequency shifting. Due to the identical modulation on each pulse, we need an alternate method to detect the frequency shift that can overcome the limitations of linear interferometry.

To measure these frequency shifts, we can measure power changes through a narrow spectral filter proportional to the frequency shift. Though the magnitude of this change in power will be small, differential detection allows for cancellation of common mode noise allowing operation very near the shot noise limit. Alternately, we can convert the frequency shift into a delay of the pulse train by applying dispersion. This delay can be measured directly, leveraging work done on the measurement of timing jitter of laser cavities. This delay will also manifest as a phase offset in the repetition rate of the laser (relative to the pulse train without the influence of the sample). Many techniques exist for the accurate measurement of RF phase, including a great deal of work done on measuring the timing jitter of laser oscillators and optically referenced RF frequency standards for optical metrology.

CHAPTER 3

Frequency Shift to Amplitude Conversion

The first measurement method for small frequency shifts is also the most direct. If we observe the power through a spectral filter that is narrow relative to the overall spectrum, then as the center frequency changes the power through the filter will change as well [22, 23]. We'll analyze the limit in sensitivity here in the fundamental, shot noise limit. This limit can be reached with reasonable ease using autobalancing photoreceivers to compensate for laser amplitude noise [24].

3.1. Theory

A schematic depiction of the center frequency shift converting into amplitude is shown in Fig. 3.1. Considering a pulse with a Gaussian power spectrum, used to sample a vibrational coherence at a pump–probe delay τ which gives rise to a center frequency shift as given in Eq. 2.5, we first write

$$S(\Omega) = S_0 \exp\left(-\frac{\Omega^2}{2a_0}\right) \tag{3.1}$$

and integrating the power transmitted by a narrow Gaussian filter defined by $F(\Omega) = \exp(-(\Omega - \sqrt{a_0})^2/(2\Delta))$. We're further assuming here the filter is centered at the point of maximum slope of the Gaussian, the best-case scenario. The filter width is given by Δ.

$$\frac{\Delta P}{P} = \frac{\int_{-\infty}^{\infty} S(\Omega - \delta\omega)F(\Omega)\,\mathrm{d}\Omega - \int_{-\infty}^{\infty} S(\Omega)F(\Omega)\,\mathrm{d}\Omega}{\int_{-\infty}^{\infty} S(\Omega)F(\Omega)\,\mathrm{d}\Omega} \tag{3.2}$$

Defining the filter as a fraction of the bandwidth $\Delta \to \sqrt{a_0}/N$

$$\frac{\Delta P}{P} = \exp\left(\frac{N\left(2\sqrt{a_0} - \delta\omega\right)\delta\omega}{2a_0(1+N)}\right) - 1 \tag{3.3}$$

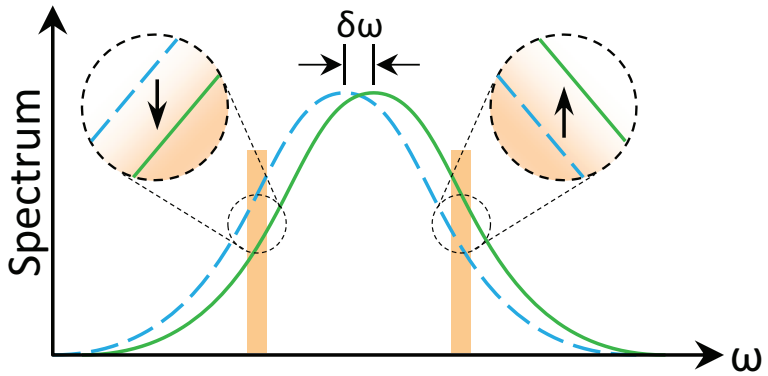

FIGURE 3.1. Schematic of the frequency shift approach, showing energy transfer through a pair of filters.

For the moment, we'll let the width of the Gaussian filter become infinitely thin, approximating a delta function at the peak of maximum slope

$$\frac{\Delta P}{P} = \exp\left(\frac{\delta\omega}{\sqrt{a_0}} - \frac{\delta\omega^2}{2a_0}\right) - 1 \tag{3.4}$$

As $\delta\omega$ is much smaller than a_0, we let the $\delta\omega^2$ go to zero and we arrive simply at

$$\frac{\Delta P}{P} = \exp\left(\frac{\delta\omega}{\sqrt{a_0}}\right) - 1 \tag{3.5}$$

We see good agreement for reasonably narrow filters, with the approximate value reaching 90% of the exact value for $N = 10$ and 99% for $N = 99$. For our experiment, we have about 10 THz of bandwidth in the pulse, and the Fiber Bragg Grating (FBG) we are using has a 30 GHz passband width, which gives an N of about 333.

We'll estimate the minimum detectable frequency shift that can be made using this method by observing the limiting case, in which the shift is small enough that the change in power through the filter is below the fundamental noise of the detection process. The single sideband power spectral density of the shot noise as a function of power is $S(f) = 2h\nu P$, with a corresponding shot noise power spectral density due to an average photocurrent I of $S(f) =$

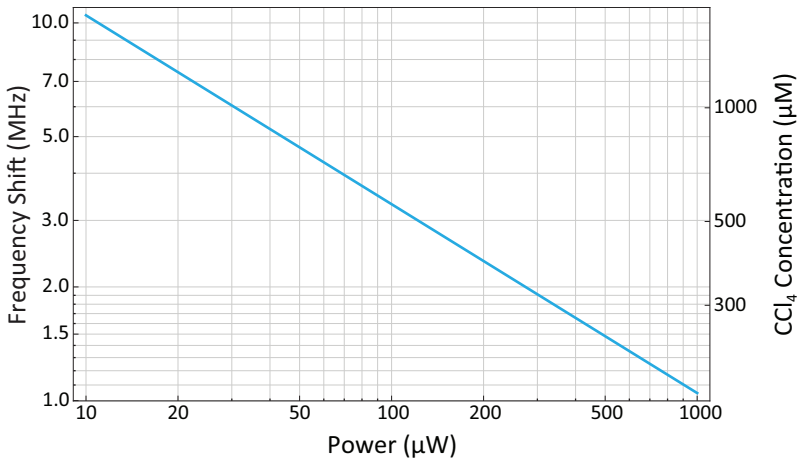

FIGURE 3.2. Shot noise limited frequency shift and CCl_4 concentration as a function of power. CCl_4 concentration was determined using the parameters specified in Appendix A.

$2qI$, where q is the electron charge. The shot noise current is $i_{\text{sh}} = \sqrt{2qi_d f_B}$, where the diode current is given by $i_d = R_p P_d$ where $R_p = \eta \frac{q}{hf}$ is the photodiode responsivity (with η being the quantum efficiency, h is Planck's constant, and f is the frequency), f_B is the bandwidth, and P_d is the power incident on the photodiode.

The smallest power level that can be measured is assumed to be the change in diode current equal to the shot noise current $\Delta P = \sqrt{f_B q P_d / R_p}$. So the shot noise limited power change is

$$\frac{\Delta \mathrm{P}}{P_d} = \sqrt{\frac{f_B q}{R_p P_d}}. \tag{3.6}$$

Equating the approximate power change through the filter to the shot noise limited power change, we can solve for the smallest $\delta\omega$ achievable as

$$\delta\omega_{\text{min}} = \sqrt{a_0} \log\left(1 + \sqrt{\frac{f_B q}{R_p P_d}}\right) \tag{3.7}$$

Let's consider the parameters for our experiment. For an 80 fs pulse with an average power of 10 µW and a detector with a responsivity of 0.9 A/W using a measurement bandwidth

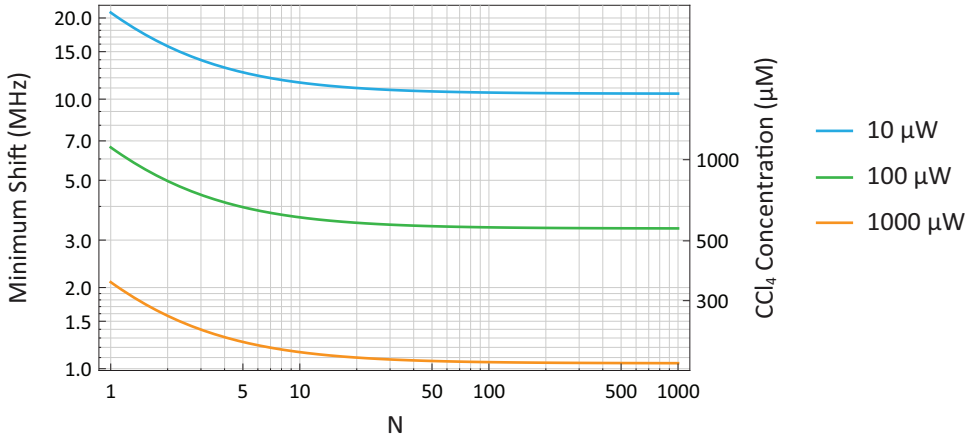

FIGURE 3.3. Minimum, shot-noise limited frequency shift as a function of filter width.

of 1 Hz gives a minimum detectable shift of 1.9 MHz. Using these same parameters, we can estimate the minimum resolvable shift as a function of power as shown in Fig. 3.2. Returning to the full form of the filtered signal as given in Eq. 3.3 to allow us to consider a wider filter. The shot-noise limited minimum shift is then given by

$$\delta\omega_{\min} = \sqrt{a_0} - \frac{1}{N}\sqrt{a_0 N\left(N - 2(1+N)\log\left(1 + \sqrt{\frac{f_B q}{R_p P_d}}\right)\right)}. \tag{3.8}$$

The minimum shift, using the parameters given above, is calculated for a variety of power levels as a function of filter width is shown in Fig. 3.3.

These estimates are based on a Gaussian spectrum. To calculate the frequency shift for an arbitrary spectral shape, we'll have to first write the photodiode signal, s(Ω) as a function of the spectrum S(Ω), through the responsivity of the photodiode R_p as $s(\Omega) = R_p S(\Omega)$. The fractional shift in signal is given by $\Delta s/s = (S(\Omega + \delta\omega) - S(\Omega))/S(\Omega)$. To evaluate this without a specific spectral shape, and arrive at an approximate expression for the change in signal level which we can relate to the frequency shift, we' ll rewrite the spectrum as a Taylor

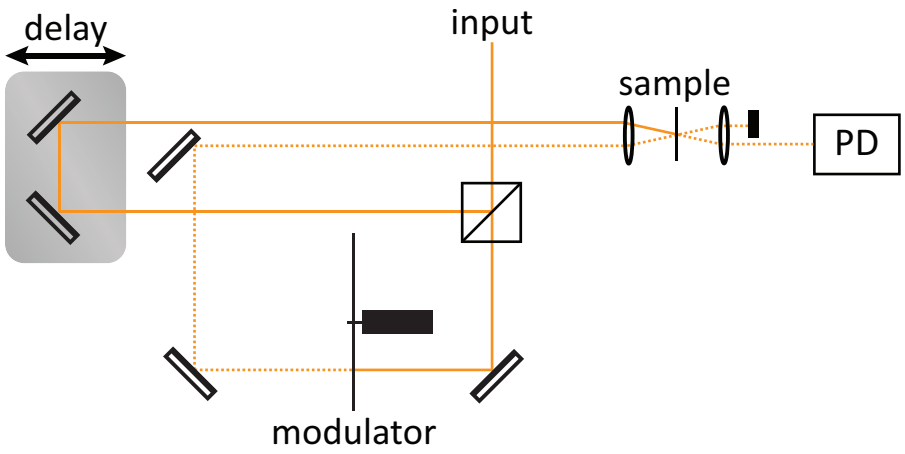

FIGURE 3.4. Optical setup of the Raman test microscope.

series (truncated here to first order)

$$S(\Omega) = RS\left(\Omega_f\right) + RS'\left(\Omega_f\right)\left(\Omega - \Omega_f\right). \tag{3.9}$$

Using this expression, and evaluating at the filter frequency for both the shifted and unshifted spectra, we can write

$$\frac{\Delta s}{s} = \delta\omega \frac{1}{S\left(\Omega_f\right)} \left.\frac{\partial S}{\partial \Omega_f}\right|_{\Omega \to \Omega_f} \tag{3.10}$$

Then the measurement of the frequency shift via the change in transmission through a spectral filter, you have only to measure the spectrum and the photodiode signal. Because the shift is determined by the ratio of signal levels and the ratio of spectra and spectral slope, the exact photodiode responsivity and spectral intensity calibration are not required.

3.2. Results

To test this setup, we built a simple Raman microscope. The microscope is a pump probe configuration built using a modified Mach Zender, as shown in Fig. 3.4. A controllable relative pump and probe delay is introduced using a motorized stage, and the probe pulse train is modulated with an optical chopper. The pump and probe beams are then made parallel and

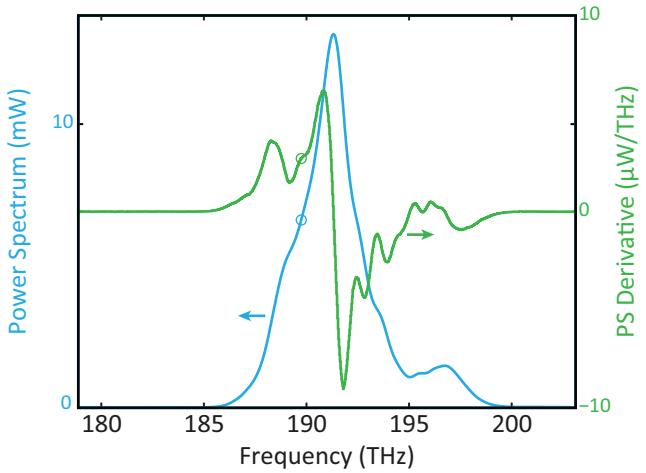

FIGURE 3.5. Power spectrum and spectral slope used in the calculation of the frequency shift. The circles indicate the location of the spectral filter.

an close enough together to fill the back aperture of the focusing objective. The beams are brought to a focus and overlapped using a Zeiss APLAN 40x 0.65NA into a 150 μm thick sample of BGO. The probe is then collected using a matching objective and coupled into an optical fiber (SMF-28E). This fiber is sent through an 90%/10% power splitter, with the 10% port connected to an OSA to measure the spectrum for each run. The 90% port is connected to the input of the fiber filter. The filter has two output fibers, the passband and reject band. The passband is connected to the signal port of an auto-balanced detector while the reject port is connected to the reference port of the auto-balanced detector through a variable attenuator. The variable attenuator is adjusted to control the power ratio between the two ports, which in turn effects the Common-Mode Rejection Ratio (CMRR) of the auto-balancing detector. Measuring the power spectrum using a Data Acquisition (DAQ) and custom written down-sampling periodogram estimation software (described in Appendix D), we can quickly minimize the output noise, thus ensuring a high CMRR.

The pump power can be controlled with a waveplate and polarizer, allowing the magnitude of the Raman signal to be varied. For each pump power, we first measure the spectrum using

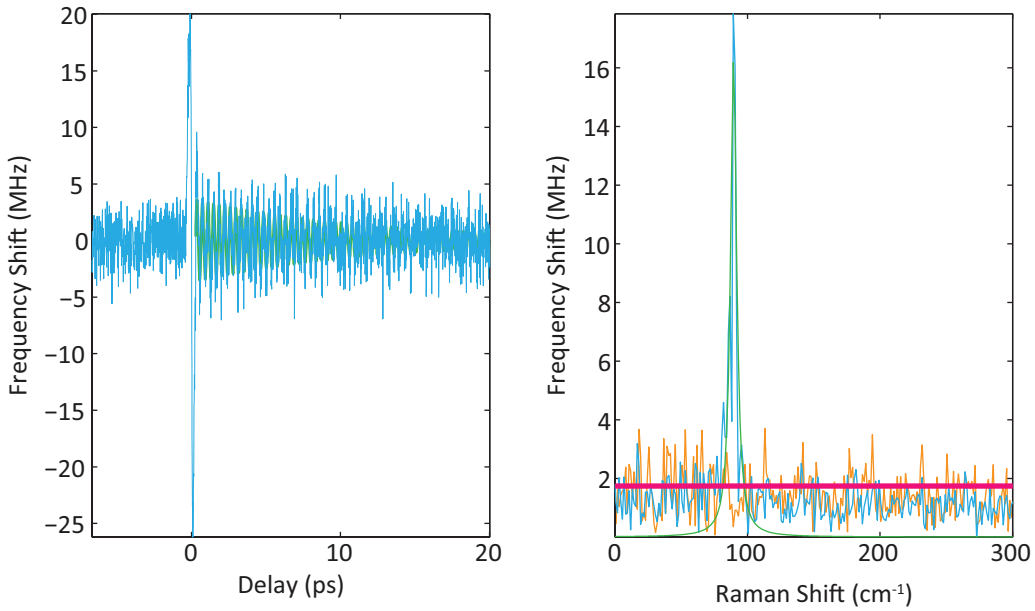

FIGURE 3.6. (a) Filter-based Raman induced frequency shift from BGO with a pump power of 3 mW. The shift is plotted with respect to the pump–probe time delay τ, a measure of how much time elapses between the arrival of the pump pulse and the arrival of the probe pulse. Negative delays show no signal as the probe pulse arrives ahead of the pump pulse. At time zero, we can see a strong signal due to cross-phase modulation. The temporal data is then processed using the Linear Prediction Singular Value Decomposition (LPSVD) algorithm, and the predicted trace plotted (green). (b) The Fourier transform of the temporal data (blue) is plotted on to of the Lorentzian Raman line from the parameters predicted by the LPSVD (green). The residual noise left by subtracting the predicted trace from the data and Fourier transforming is plotted (orange) along with the theoretical noise floor calculated using Eq. 3.8 (red).

the OSA. From this spectrum, the power and slope at the filter location can be determined and the fractional spectral slope calculated, as shown in Fig. 3.5. The filter used has a 30 GHz passband width and is centered at 1580 nm. The fractional spectral slope at this point is 4.1/Hz, just off the peak of the spectral slope. If a custom filter were to be commissioned at the point of peak spectral slope, the fractional slope could be increased by about 20%.

The autobalanced signal power output is connected to the input of a lock-in amplifier. The reference signal for the lock-in is generated using CW beam focused on the same optical chopper and collected with a photodiode. The lock-in values are then recorded as a function of

pump-probe delay, giving a trace as shown in Fig. 3.6(a). The average signal value is sampled at each point using a DAQ, from which we can calculate the fractional signal, and that combined with the fractional slope gets us a measure of the optical frequency shift using Eq. 3.10.

The Raman spectrum can be found from this pump-probe trace via a Fourier transform. The Raman spectrum given by transforming the entire trace is displayed on a log scale showing BGO's strong 89 cm^{-1} mode in Fig. 3.6(b). The time trace is also processed using an LPSVD algorithm, which presumes the data is a linear combination of exponentially-decaying sinusoids and determines the amplitude, phase, frequency, and damping coefficient of each component. The data shown contains only a single Raman frequency, and the predicted trace is plotted beneath the measured trace. The spectrum can be determined from these predicted parameters, as the Fourier transform of an exponentially decaying sinusoid is a Lorentzian. The predicted Lorentzian is plotted in terms of the parameters determined by the LPSVD beneath the Fourier transform of the measured data. The noise floor alone is plotted by subtracting the predicted noise-free LPSVD trace from the measured data and Fourier transforming the resulting data, which is assumed to contain only noise. This is plotted on top of the data, with the expected shot-noise limited noise floor, as predicted by Eq. 3.6 for the power level used in this measurement, shown as a solid line.

The time trace is also processed using a Gabor transform, in which a Gaussian window is used to select a region of the time trace at a time delay τ and Fourier transforming the trace, producing a spectrogram shown in Fig. 3.7. Using a 1 ps Gaussian window, we see the Raman signal fall into the noise near 2 MHz, in good agreement with the calculated value. This transform shows the dependence of the frequency shift on the pump probe delay in a quantitative way. The Fourier resolution of the spectrogram is inversely proportional to the

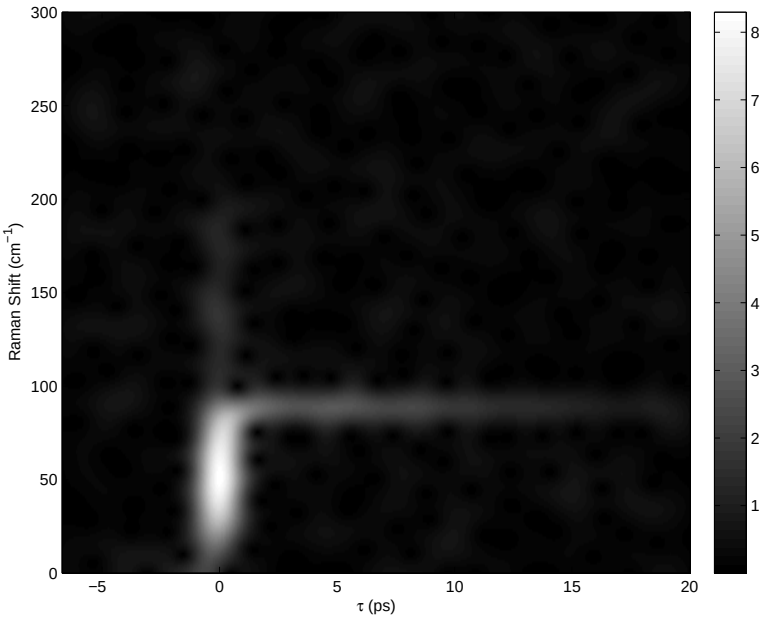

FIGURE 3.7. Spectrogram produced by Gabor transform of the temporal Raman signal, as shown in Fig. 3.6(a). The width of the Gaussian window used in the Gabor transform is 1 ps. Near time-zero, we see the broad spectrum caused by the cross-phase modulation signal. At larger delays, we see only the contribution of 89 cm^{-1} as it decays, before falling to the noise floor.

width of the Gaussian time window with the amplitude of the line as the average frequency across the time bin.

We've demonstrated here good performance of the system that converts a small optical frequency shift to an intensity, consistent with the noise performance expected from our experimental parameters. The system, while attractive given the simplicity of the experimental setup, is limited by fundamental detector noise. To improve the sensitivity of the measurement of the Raman induced frequency shift, we'll take a different approach, one which converts the frequency shift into a time delay, and is subject to different fundamental noise constraints.

CHAPTER 4

Frequency Shift to Delay Conversion

The final method for measurement of the Raman-induced frequency shift is based on measurement of time delay. We've seen that direct measurement with a grating spectrometer is limited by spectrometer resolution to about a gigahertz, and the filter-based conversion of frequency shift to power change is limited to shifts on the order of a few megahertz (for a 1 Hz measurement bandwidth in the shot noise limit).

The shift in optical frequency of an ultrafast pulse can be turned into a time delay through the application of dispersion. As ultrafast pulses are made up of many different colors of light, when the pulses travel in a dispersive material, these different colors travel at different speeds. When the pulse exits the material, it will have picked up a time delay proportional to the center frequency, as shown in Fig. 4.1. Mathematically, we can write the pulse propagation through a material in terms of acquisition of a spectral phase, which we can write as a Taylor expansion $\Phi(\Omega) = \varphi_0 + \varphi_1\Omega + \frac{1}{2}\varphi_2\Omega^2 + ...$ The transit time of a pulse through the system is given by the group delay, $\tau_g = \partial\Phi(\Omega)/\partial\omega$. The group delay can then be written in terms of the dispersion as $\tau_g = \varphi_1 + \varphi_2\Omega$, where we've truncated terms beyond second order, as we expect φ_2 to dominate the change in group delay. Thus, the transit time will change with a change in center frequency as

$$\Delta\tau_g = \varphi_2\delta\omega \tag{4.1}$$

Thus we are left with a time delay which is proportional to the frequency shift, which is in turn proportional to the Raman response. The problem of measurement of the optical frequency shift has turned to the measurement of small time delays, which we'll look at measuring in two ways. The first will be based on optical cross correlation, which will turn

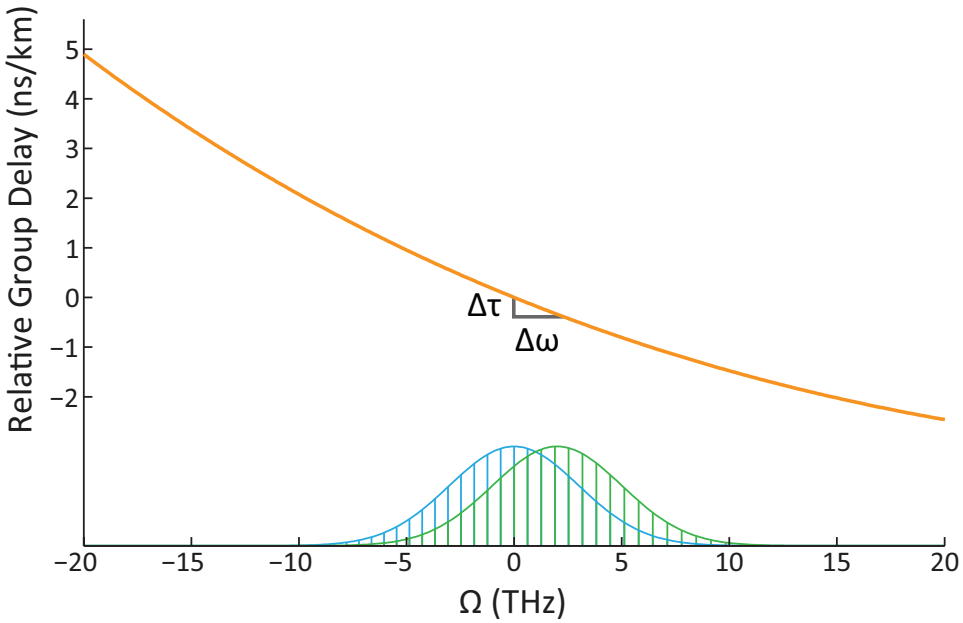

FIGURE 4.1. Schematic depiction of the time delay, $\Delta\tau$, induced by a shift in center frequency, $\Delta\omega$, of a pulse in a dispersive material. The dispersion curve shown is for fused silica glass centered at 1550 nm.

a small timing change into an amplitude change of the autocorrelation signal. The second will also turn the delay signal into a power signal, but through the use of an electro-optic intensity modulator, which will enable an RF oscillator to be phase locked to the pulse train. The measurement of this timing change is then made as an RF phase measurement, finally translating task of measuring $\delta\omega$ into $\delta\phi_{\mathrm{RF}}$. Such phase measurements can be made very accurately, giving this technique a detection limit much lower than systems which measure power directly.

4.1. Balanced Cross-Correlator

The first approach we examined for the measurement of a small timing signal is using a balanced cross correlator [25]. The delayed pulse is mixed with itself in a nonlinear crystal, which maps the timing delay into a change in the amplitude of the correlation signal. This

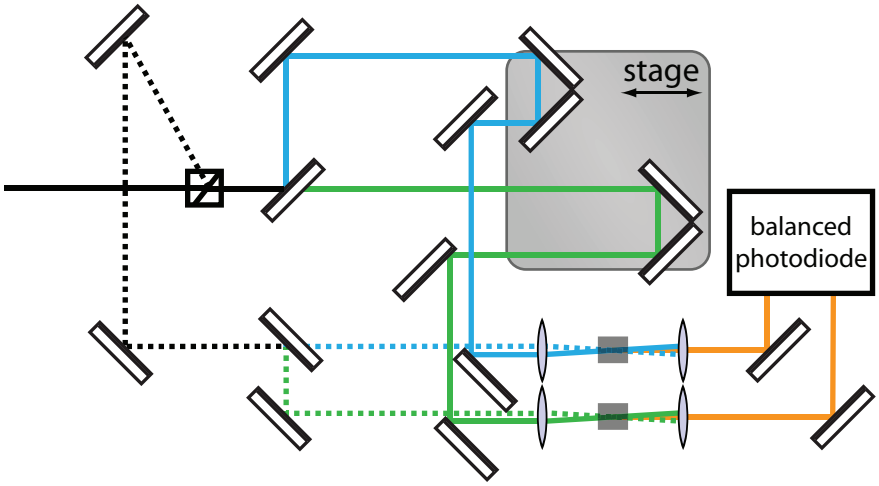

FIGURE 4.2. Schematic of the balanced cross correlator for measurement of laser timing jitter.

technique is common in short-pulse laser systems, which can generate steep nonlinear correlation signals. The amplitude of the sum frequency signal sets the slope of the amplitude versus time delay measurement, so for high sensitivity it is advantageous to have a large slope, requiring short pulses. However, as the time delay we are attempting to measure is born of the application of GDD to frequency-shifted pulses, our pulses are necessarily chirped. Moreover, as seen in Eq. 4.1, the magnitude of the delay is linearly proportional to the applied GDD, thus we have two countervailing effects on signal level: the sensitivity decreases for large chirp as the square of the GDD but increases linearly with the GDD. To calculate this interplay, we'll start with a transform limited gaussian pulse in time $E(t) = \exp(-a_0 t^2)\exp(\imath\omega_0 t)$, where $a_0 = 2\log(2)/\tau_p^2$, with a corresponding spectrum $E(\Omega) = \sqrt{\pi/a_0}\exp\left(-(\omega-\omega_0)^2/(4a_0)\right)$. The dispersive element adds spectral phase, which (to second order) takes the form

$$\varphi(\Omega) = \varphi_0 + \varphi_{(1,\delta\omega)}\Omega + \frac{1}{2}\varphi_{(2,\delta\omega)}\Omega^2 \tag{4.2}$$

where $\Omega = \omega - \omega_0$ and $\varphi_{(n,\delta\omega)} = \partial^n\varphi/\partial\omega|_{\omega=\omega_0+\delta\omega}$. ω' is the pulse center frequency, ω_0 for the unshifted pulse and $\omega_0 + \delta\omega$ for the shifted pulse. This phase stretches and delays the

temporal pulse, with the temporal pulse now given by

$$E(t) = \frac{2\pi}{\sqrt{1 + 2\imath a_0 \varphi_{(2,\delta\omega)}}} \exp\left[(a - \imath b)(t - \varphi_{(1,\delta\omega)})^2\right] \exp(-\imath\varphi_0) \exp(\imath\omega_0 t) \tag{4.3}$$

with $a = a_0/\left(1 + (2a_0\varphi_{(2,0)})^2\right)$ and $b = 2a_0^2\varphi_{(2,0)}/\left(1 + (2a_0\varphi_{(2,0)})^2\right)$ for the unshifted pulse, and similarly $a = a_0/\left(1 + (2a_0\varphi_{(2,\delta\omega)})^2\right)$ and $b = 2a_0^2\varphi_{(2,\delta\omega)}/\left(1 + (2a_0\varphi_{(2,\delta\omega)})^2\right)$ for the frequency shifted pulse. Assuming a small $\delta\omega$, these expansions simplify

$$\begin{aligned}
\varphi_{(1,s)} &= \frac{L}{c}(n_0 + n_0'\delta\omega + (\omega_0 + \delta\omega)(n_0' + n_0''\delta\omega)) \\
&\approx \varphi_{(1,0)} + \varphi_{(2,0)}\delta\omega + \frac{L}{c}(n_0''\delta\omega)\delta\omega \\
\varphi_{(2,s)} &= \frac{L}{c}(2n_0' + 3n_0''\delta\omega + \omega_0 n_0'') \qquad (4.4) \\
&\approx \varphi_{(2,0)} + 3\frac{L}{c}n_0''\delta\omega \\
&\approx \varphi_{(2,0)} \qquad (4.5)
\end{aligned}$$

The temporal field of the shifted pulse, letting $\varphi_2 \equiv \varphi_{(2,0)} = \varphi_{(2,s)}$ and $\varphi_1 \equiv \varphi_{(1,0)}$, can then be approximated as

$$E(t) \approx \frac{2\pi}{\sqrt{1 + 2\imath a_0 \varphi_2}} \exp\left[-(a - \imath b)\,(t - \varphi_1 + \varphi_2^2)\right] \exp(-\imath\varphi_0) \exp(i(\omega_0 + \delta\omega)t) \tag{4.6}$$

we can write the intensity autocorrelation as

$$A(\tau) = \frac{8\pi^{9/2}}{\sqrt{a_0 + 4a_0^3\varphi_2^2}} \exp\left[-\frac{a_0\tau^2}{1 + 4a_0^2\varphi_2^2}\right]. \tag{4.7}$$

The slope of the autocorrelation is given by is maximized at $\tau = \sqrt{(1 + 4a_0^2\varphi_2^2)/(2a_0)}$. The slope at this point $\partial A/\partial\tau = -\sqrt{2}e^{-1/2}8\pi^{9/2}/(1 + 4a_0^2\varphi_2^2)$. As the delay is linear in φ_2, from

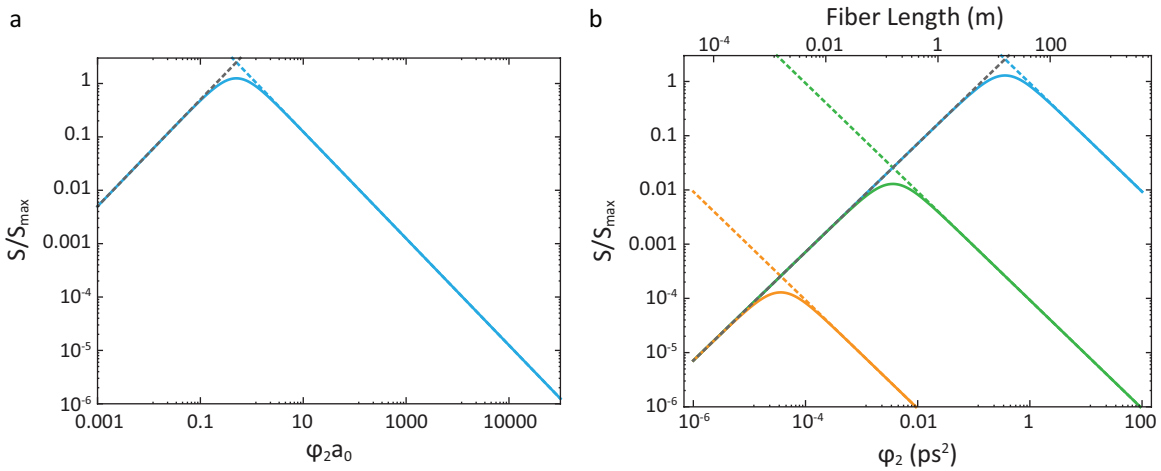

FIGURE 4.3. Calculated normalized balanced photodiode signal as a function (a) of the $\varphi_2 a_0$, to which the frequency shift signal is proportional as can be seen in Eq. 4.8, and (b) of φ_2 and length of SMF-28e fiber for transform-limited pulse durations of 10 fs (orange), 100 fs (green), and 1 ps (blue). In both figures, the dashed gray line represents the contribution of φ_2 in the small-chirp limit, $\varphi_2/a_0 \ll 1$, and the dashed colored lines indicate the contribution in the large-chip limit, $\varphi_2/a_0 \gg 1$, for the corresponding pulse duration.

Eq. 4.1, the change in autocorrelation signal as a function of $\delta\omega$ is given by $\partial A/\partial\omega = \varphi_2 \partial A/\partial\tau$. As shown in Fig. 4.3, the signal is maximized for $\varphi_2 = 2/a_0$, at which point the signal level has been maximized owing to its linear dependance on the GDD to give rise to the delay, but before the slope has begun to fall significantly due to the GDD^{-2} dependence of the pulse duration.

To compensate for amplitude noise, and keep it from getting erroneously interpreted as timing changes, the delays will be set such that the slope is sampled on either side of the autocorrelation and the difference signal monitored. The error signal is thus twice the maximum slope times the time delay, $\delta\tau$. We can then calculate the minimum detectable frequency, again in the shot noise limit, where as above the power spectral density of the shot noise is given by $S(f) = 2qI$. The fractional power change is given again per Eq. 3.6 and equated to the fractional autocorrelation signal, $\delta A/A = \delta\omega\varphi_2\sqrt{(2a_0)/(1+4a_0^2\varphi_2^2)}$. This

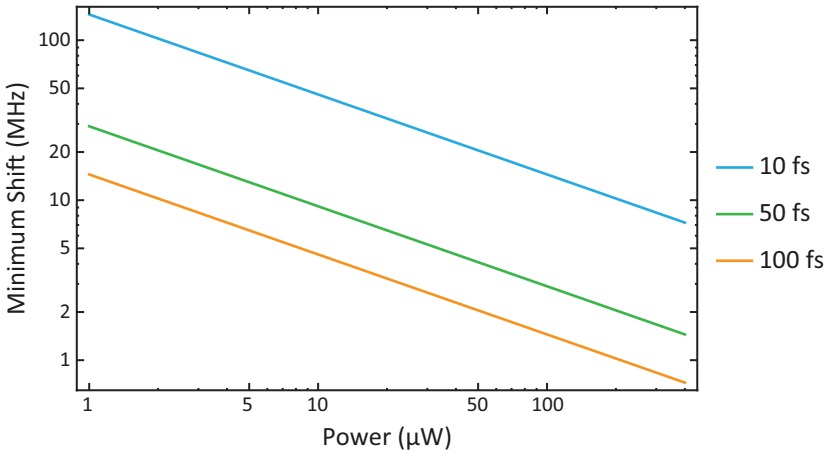

FIGURE 4.4. Shot-noise limited minimum shift, calculated from Eq. 4.9, for several pulse durations assuming operation at the peak autocorrelation slope and at the optimum GDD, assuming a 1 Hz measurement bandwidth.

yields a shot-noise limited minimum frequency shift of

$$\delta\omega = \sqrt{\frac{2f_{\mathrm{B}}q}{P_d R_p \varphi_2}\frac{1+4a_0^2\varphi_2^2}{a_0\varphi_2}}, \tag{4.8}$$

where f_B is again the measurement bandwidth, q is the electron charge, P_d is the average power, and R_p is the photodiode responsivity. At the ideal chirp, $\varphi_2 = 2/a_0$, this simplifies to

$$\delta\omega = \sqrt{\frac{17 f_B q a_0}{2P_d R_p}}. \tag{4.9}$$

From this equation, we calculate the shot-noise limited minimum frequency shift for a variety of average powers and several transform-limited pulse durations, as shown in Fig. 4.4.

While the sensitivity predicted here is higher than the direct spectrometer measurement, and slightly higher than the filter-based approach discussed in Chapter 3, this approach is difficult for two reasons. First, achieving high power levels is difficult given the low nonlinear

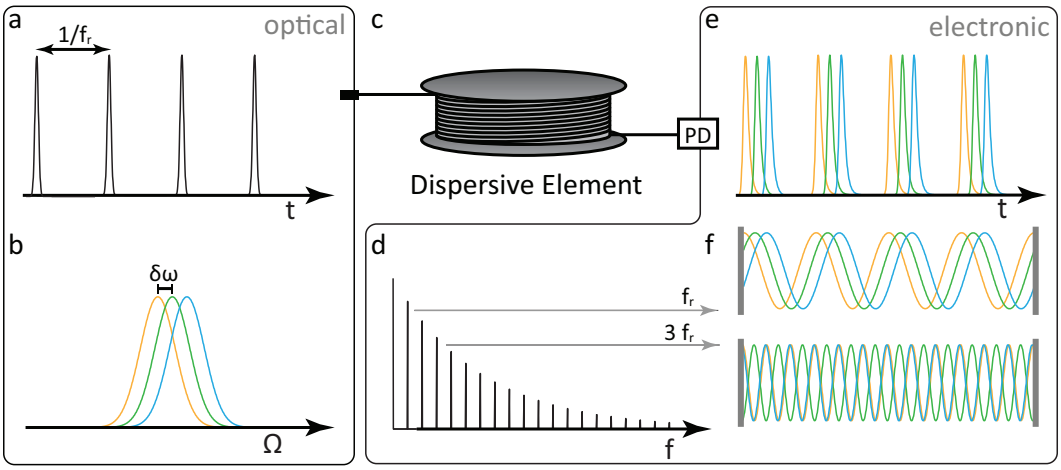

FIGURE 4.5. Schematic of frequency shift to time delay conversion. The optical pulse train (a) acquires a shift in center frequency, shown for 2 different shifts in (b). Propagation through a dispersive element, such as an optical fiber (c), introduces a time delay on the pulse train when it is collected on a photodiode (PD) (e). The electronic pulse train spectrum (d) consists of a series of harmonics of the repetition rate, which can be separated through electronic filtering, as in the first and third harmonic shown in (f).

conversion efficiency. Second, the GDD is limited to small values owing to the strong dependence of the autocorrelator signal level on pulse duration. To reach higher sensitivity, we'll adopt an approach that does not require nonlinear conversion of short pulses.

4.2. Direct Pulse Train Measurement

As the previous method required the use of short pulses to get appreciable timing sensitivity, we'll turn to an alternate measurement technique based around locking of microwave oscillators to optical pulse trains. In the simplest setup, the optical pulse train is converted to an electronic pulse train using a photodetector. The electronic signal looks like a series of electronic impulses, with a shape given by the impulse response of the photodetector. This impulse train can be filtered to generate a sine wave at the repetition rate or a harmonic of the repetition rate (with the number of harmonics present limited by the bandwidth of the photodetector). The timing change in the pulse train maps to a phase shift in this sinusoidal

signal, which is measured using the phase measurement setup described in Appendix C. This phase change is the signal of interest, as it gives a measurement of the frequency shift as

$$\Delta\phi_{\mathrm{RF}} = 2\pi m f_r \Delta\tau = 2\pi m f_r \varphi_2 \delta\omega \tag{4.10}$$

where m is the chosen harmonic of the repetition rate frequency, f_r.

The performance of this measurement system is degraded by noise introduced by the photodetector, as well as noise present in the phase locking setup. Amplitude noise measured on the photodiode will manifest as white phase noise written on to the locked oscillator [26]. The shot noise limited phase noise, converted from [26] in Appendix B, is

$$S_\phi(f) = \frac{P_{\mathrm{shot}}}{P_{\mathrm{signal}} f_B}, \tag{4.11}$$

which can be expressed in dBr/Hz (rad.^{2}/Hz). In this equation, P_{signal} is the power of the microwave signal from the photodiode at the desired harmonic m of the repetition rate frequency mf_r and $P_{\mathrm{shot}} = 2qf_B R_p P_d R$ is the shot-noise power of the light incident on the photodiode, where q is the electron charge, f_B is the measurement bandwidth, R_p is the photodiode responsivity, P_d is the average power incident on the photodiode, and R is the load impedance.

This expression is based on the shot noise as a result of average power incident on the photodiode. In more recent work [27], correlations in the measured shot noise of short pulse trains was used to operate at shot-noise limited levels several orders of magnitude below that predicted using the average power. These experiments made use of a new class of fast photodiodes with very high power handling, distinct from those used in our work.

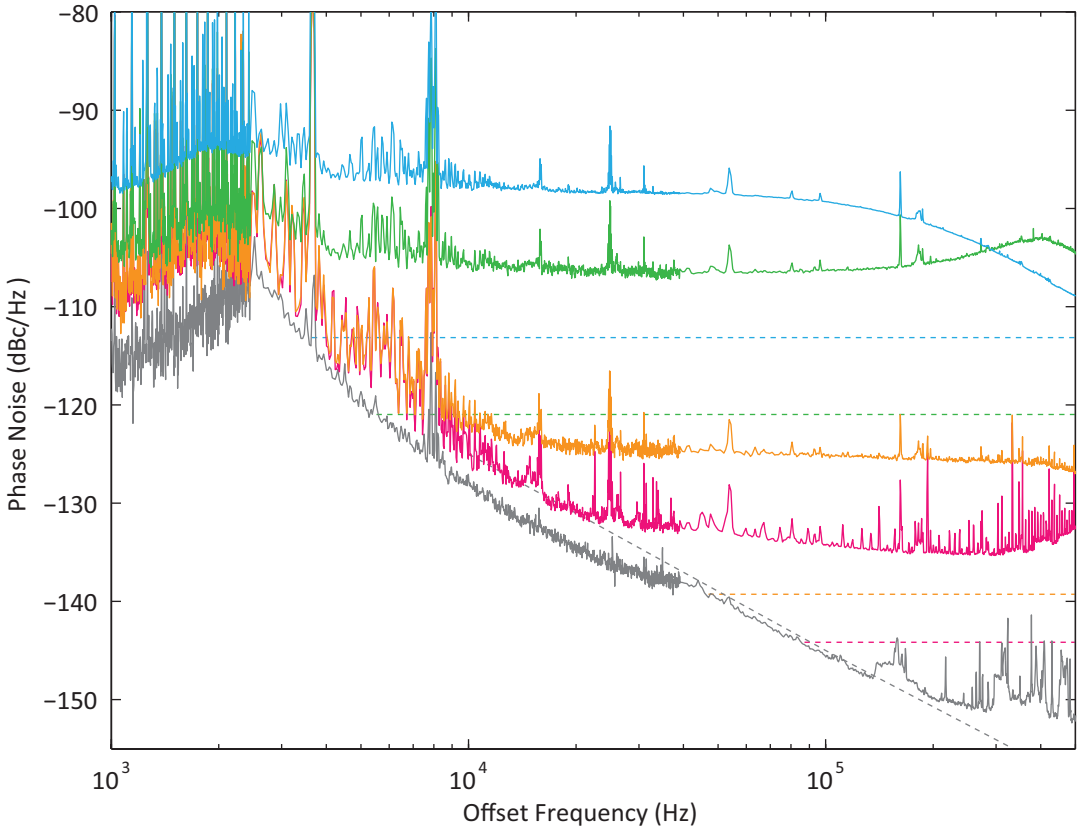

FIGURE 4.6. Measured phase noise floor of a the pulse train incident on a single diode for different power levels. The dashed lines show the shot-noise limited noise floor, calculated from Eq. 4.11, for each power level. The gray curve shows the measured phase noise floor of the reference oscillator, with the dashed line giving the expected noise floor.

Methods. To quantify the noise floor in our single-detector measurement, we couple the frequency shifted pulses into a ≈20 km length of optical fiber and then detect the pulse train with a photodiode (Thorlabs DET10C). Figure 4.6 shows the single-sideband phase noise of the repetition rate measured using the phase noise measurement system described in Appendix C. This measurement is made for several power levels, and plotted along side the shot-noise limited noise floor calculated for each power level using Eq. 4.11.

As the photodiode signal was not sufficient to drive the mixer in the phase measurement setup, an RF amplifier (Minicircuits ZHL-3010) was used which provided 30 dB gain with a 6 dB noise figure. This accounts for some of the degradation of the expected performance (as

the plotted theoretical floor does not account for the noise figure of this amplifier), though the difference between the measurement and the expected value is close to 14 dB. The extra 8 dB is likely due to excess noise coming from amplitude to phase noise conversion in the photodiode and in the mixer, as well as noise picked up in propagation through the experiment and through the long fiber.

4.3. Optical Phase-Locked Loop

In order to reduce the impact of this amplitude noise, and lower the noise floor of the measurement, we'll follow the path of [28] and move to a system which is less dependant on the impact of the photodetector. This approach balances two opposing signals to cancel out any common amplitude noise, akin to the approach in Section 4. Unlike that case, however, the cancelation does not require a nonlinear process, and thus, our chirped pulses will have less of an impact on the overall stability of the measurement.

This approach, which is dubbed the "Optical PLL" is based on the use of optical amplitude modulators driven by an electronic reference oscillator to generate an error signal by attenuating the pulse train at the repetition rate. The input pulse train is split in half, and each half amplitude modulated with sinusoidal modulations out of phase with each other by π, as shown in Fig. 4.7. The modulated pulse trains are then measured on photodetectors and the difference signal taken. In this way, small changes in the arrival time of the pulses will result in a small decrease in one signal and a small increase in the other. The difference signal will then show a change proportional to twice the time change, while any amplitude noise common to both channels will be removed. The difference signal serves as an error signal which is fed back to a servo controlling the frequency of the microwave oscillators.

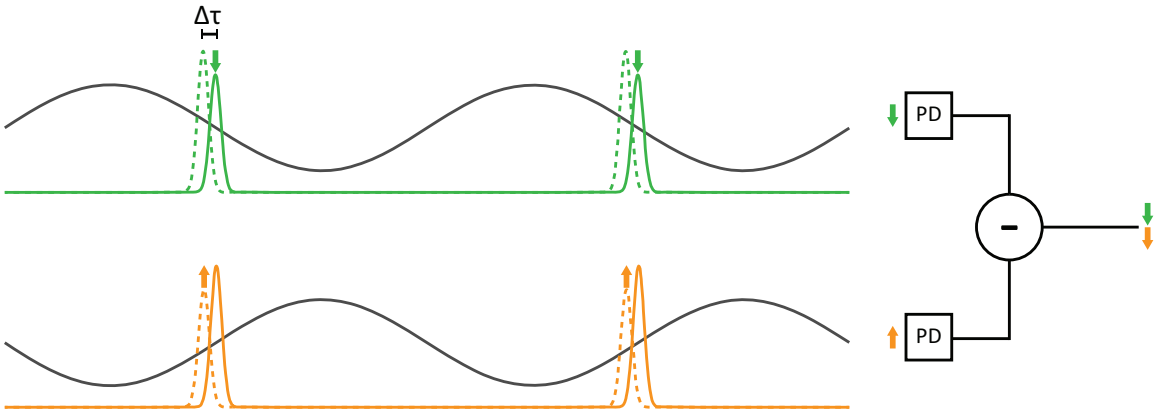

FIGURE 4.7. Schematic depiction of the drive signals in the Optical PLL. Amplitude modulation is applied to two copies of the pulse train, π out of phase. This differential modulation generates an error signal that doubles dependence on $\Delta\tau$ while cancelling any common mode noise on the pulse train.

In this architecture, amplitude noise being written to the error signal is avoided, as the two error signals vary with opposite signs with respect to timing jitter, but will react in the same way to amplitude noise. Taking the difference between these signals as our error signal gives rejection of common amplitude noise while doubling the dependance on timing jitter. Using this method, Kim et al. measured an Root Mean Squared (RMS) timing jitter of 2.4 fs (integrated from 1 mHz to 1 MHz) [29]. More recently, Jung and Kim measured an RMS timing jitter of 0.847 fs (integrated from 1 Hz to 1 MHz) [30].

Theory. We'll consider formally the sensitivity of the Optical PLL method. We'll begin by considering the difference signal taken between two photodiodes, measuring pulse trains with intensity modulation driven by sine waves at the repetition rate, but 180° out of phase with one another. Following the similar derivation in [29], the unmodulated pulse train has the form

$$P_{\text{in}}(t) = \frac{P_{\text{avg.}}}{f_r} \sum_{-\infty}^{\infty} \delta\left(t - \frac{n}{f_r}\right)$$

where $P_{\text{avg.}}$ is the average power. The fiber amplitude modulator considered here is a Mach-Zehnder set up in a push-pull configuration [31]. The applied voltage to the modulator changes the phase relationship between the light in the two arms of the internal interferometer, leading to a transmission given by

$$T_{\text{M}} = \frac{1}{2}\left[1 + \cos\left(\pi\frac{V}{V_\pi} - \phi_{\text{b}}\right)\right]$$

where V_π is the voltage required to shift the modulator phase by π, e.g., the voltage difference between minimum and maximum attenuation, and is determined by the design of the modulator [32]. The bias phase ϕ_{b}, is typically set to $\pi/2$ so that the modulator operates in a quasi-linear regime. Driving the modulator with a sinusoidal voltage, V at the chosen harmonic of the repetition rate, mf_r, leads to a power transmission that can be written

$$P_{\text{out}}(t) = P_{\text{in}}(1-\alpha_{\text{M}})\left[\frac{1}{2} + \frac{1}{2}\sin\left(\pi\frac{V_0}{V_\pi}\sin\left(2\pi m f_r t + \Delta\phi + \phi_e\right)\right)\right],$$

where P_{in} is the input power, α_{M} is the insertion loss of the modulator, ϕ_e is the phase change to be measured, and $\Delta\phi$ is the phase difference between the modulation signals. We'll define the phase depth as a function of the sine wave voltage amplitude V_0 and V_π as $\Phi_0 = \pi V_0/V_\pi$. We can then write the power in each channel, where we have set $\Delta\phi = \pi$ such that the pulse train is sampling the positive and negative slopes of the driving sine wave. The power in each channel can be written

$$P_{\pm}(t) = \frac{P'_{\text{avg.}}}{f_r}\sum_{-\infty}^{\infty}\alpha_{\text{M}}\left[\frac{1}{2} \pm \frac{1}{2}\sin\left(\Phi_0\sin\left(2\pi m f_r t + \phi_e\right)\right)\right]\delta\left(t - \frac{n}{f_r}\right),$$

where $P'_{\text{avg.}} = (1-\alpha_{\text{M}})P_{\text{avg.}}$ is the power coupled into the modulator. We'll sample this modulation at the zero crossing, so we can substitute $t = n/f_r$ and write the average current

from the photodiode for each channel is then given in terms of the photodiode responsivity, R_p, as

$$\langle I_+ \rangle = R_P P'_{\text{avg.}} \left[\frac{1}{2} + \frac{1}{2} \sin\left(\Phi_0 \sin\left(\phi_e\right)\right) \right]$$

$$\langle I_- \rangle = R_P P'_{\text{avg.}} \left[\frac{1}{2} - \frac{1}{2} \sin\left(\Phi_0 \sin\left(\phi_e\right)\right) \right]$$

The difference signal is then

$$\langle I_d \rangle = \langle I_+ \rangle - \langle I_- \rangle$$

$$= R_p P'_{\text{avg.}} \sin\left(\Phi_0 \sin\left(\phi_e\right)\right).$$

As the phase error ϕ_e is assumed to be small, we can presume that we are operating in the small-angle limit, and thus approximate

$$\langle I_d \rangle = R_P P'_{\text{avg.}} \Phi_0 \phi_e.$$

The phase detection sensitivity, K_d, can be written from Eq. 4.3 as, $K_d = \langle I_d \rangle / \phi_e = R_p P'_{\text{avg.}} \Phi_0$. This method will again be fundamentally limited by shot noise, now shot noise of the detected sinusoidally modulated power. The shot noise current density, in A^2/Hz, is given by $S = 2qI = qR_p P'_{\text{avg.}}$. This current density can be converted to a phase noise spectral density, rad^2/Hz, by dividing by the square of the phase detection sensitivity, K_d, giving

$$S_{\varphi, I_{\text{shot}}} = \frac{S}{K_d^2} = \frac{q}{R_p P'_{\text{avg.}} \Phi_0^2} \tag{4.12}$$

where q is the charge of an electron. This power spectrum is a white noise process limited by the photocurrent, but with the added dependence on Φ_0^2. Like the single diode case, this noise floor can be reduced by increasing the average power or the photodiode responsivity. Where this is advantageous over the single diode case is the dependence on Φ_0. We can increase Φ_0 to decrease the shot-noise limited floor below the single-diode case by increasing the RF power. This method is also not as influenced by amplitude to phase noise conversion, as common amplitude noise is canceled by the differential detection.

This analysis presumed the noise is dominated by the shot noise on the error signal. While this is the fundamental limit, the measured noise floor will always be the sum of all relevant noise sources. If the noise of some component exceed the shot-noise, for example from one of the oscillators, then the noise of that oscillator will dominate and appear as the noise floor. We will now estimate the magnitude of the shift that will be visible for some given noise floor, be it limited by oscillator phase noise, noise introduced by the error signal, or by timing jitter from the laser itself.

Methods. To find the sensitivity of the detection system in the presence of the above described noise, we'll return to change in delay as a function of change in center frequency, $\delta\tau = \varphi_2\delta\omega$. This delay change corresponds to a phase change of $\phi(\tau) = 2\pi f_r\varphi_2\delta\omega$, as depicted in Fig. 4.7. Equating this phase change to the phase noise for various levels, we can solve for the minimum frequency shift as

$$\delta\omega = \frac{\sqrt{2 \times 10^{\mathcal{L}(f)/10}\Delta f}}{2\pi m f_r \varphi_2} \tag{4.13}$$

where we have assumed a bandwidth narrow enough that the power spectrum does not change appreciably over the bandwidth. The minimum detectable frequency is calculated

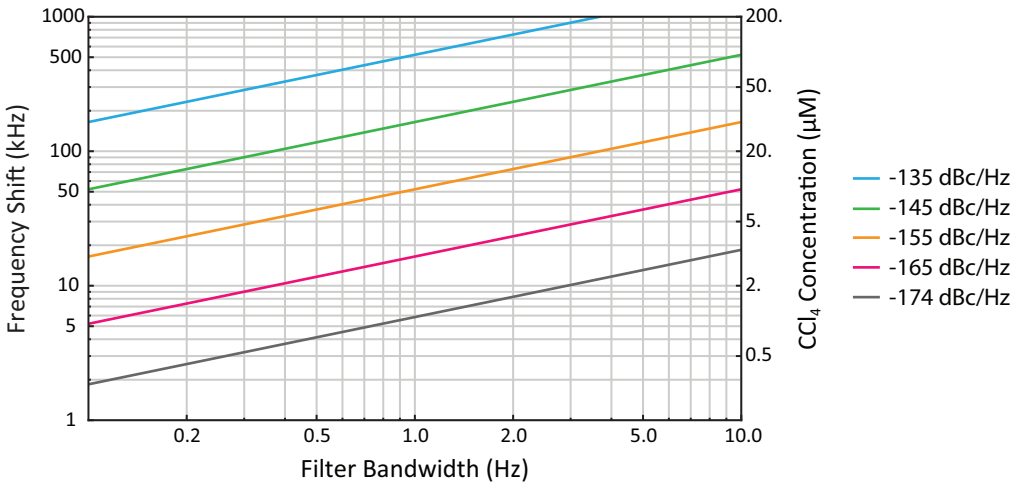

FIGURE 4.8. Minimum frequency shift as a function of the measurement bandwidth for a variety of oscillator phase noise levels, down to the thermal noise floor (-174 dBc/Hz, for signal power of 0dBm). The trend shown in this plot can be continued to lower thermal noise floors, available with higher powers.

for 20.5 km of fiber and our 36.7 MHz fundamental (m=1) repetition rate as a function of measurement bandwidth and oscillator phase noise in Fig. 4.8. The dispersion of SMF-28e is D=18 ps/nm/km (β_2 = -23 ps^2/km), so φ_2 for 20.5 km of fiber is ≈471 ps^2. The oscillator runs at 24th the harmonic of the repetition rate, 880 MHz, with an output power of 6 dBm. The phase noise is from the oscillator is -145 dBc/Hz for a 100 kHz offset. Dividing this down to the repetition rate introduces a small amount of additive phase noise, S_D.

The optical setup is a simple variation of the previously describe test setup. The electronic components and additional optical components used for the Optical PLL are shown in the block diagram in Fig. 4.9. The Raman-shifted probe pulse (following the setup described in the previous section) is coupled into the optical fiber (Corning SMF-28e) in place of the spectral filter. The light is then split into the two channels using a -3 dB fiber splitter, and each output channel of the fiber splitter is spliced to the input of a lithium-niobate amplitude modulator (JDSU). The amplitude modulators only operate on one polarization, so the input fiber is laid in a polarization controller (General Photonics) which is used to project as much

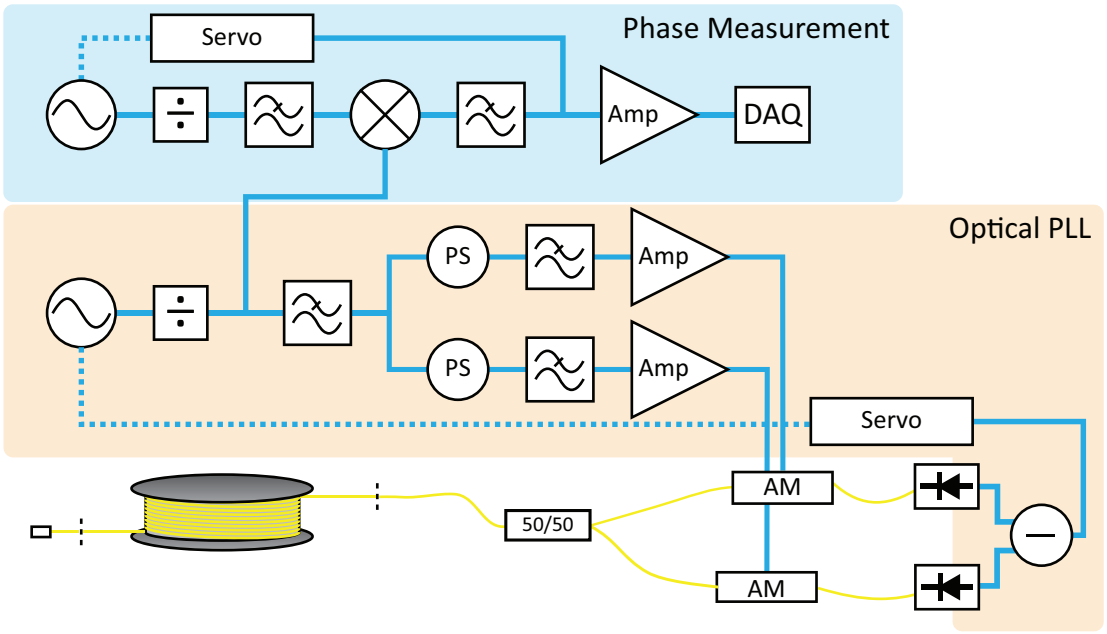

FIGURE 4.9. Optical PLL block diagram, described in detail in the text. PS is phase shifter and AM is amplitude modulator. RF signals are shown with solid blue lines, control signals are dashed blue lines, and optical fibers are shown in yellow. The pulse to be measured enters the fiber in the bottom left, propagates through the optional long fiber, then is split 50/50 to be modulated before being detected on matched photodetectors. The phase measurement setup is described in detail in Appendix C.

light as possible on the active polarization axis of the modulator. The light is collected with a pair of InGaAs photodiodes (Thorlabs DET10C), and the difference signal generated with a summing amplifier (SRS SIM980). This difference signal is the error signal, coupled in to the input of the servo (Vescent Photonics). The output of this servo is the reference voltage for a Voltage Controlled Oscillator (VCO) (Minicircuits ZX95-890C) that drives the amplitude modulators. The servo parameters and optimization are discussed further in Appendix C.

The modulators are driven with a sine wave at the repetition rate, with the phase of the electronic signals adjusted such that the pulses are sampling the peak slope of the modulators attenuation on both the rising and falling signals. This signal is generated from a VCO that is divided (Valon 3008) before being split into two channels (Minicircuits ZFRSC-42), each of which goes into a voltage variable phase delay (Minicircuits JSPHS-51) before being amplified

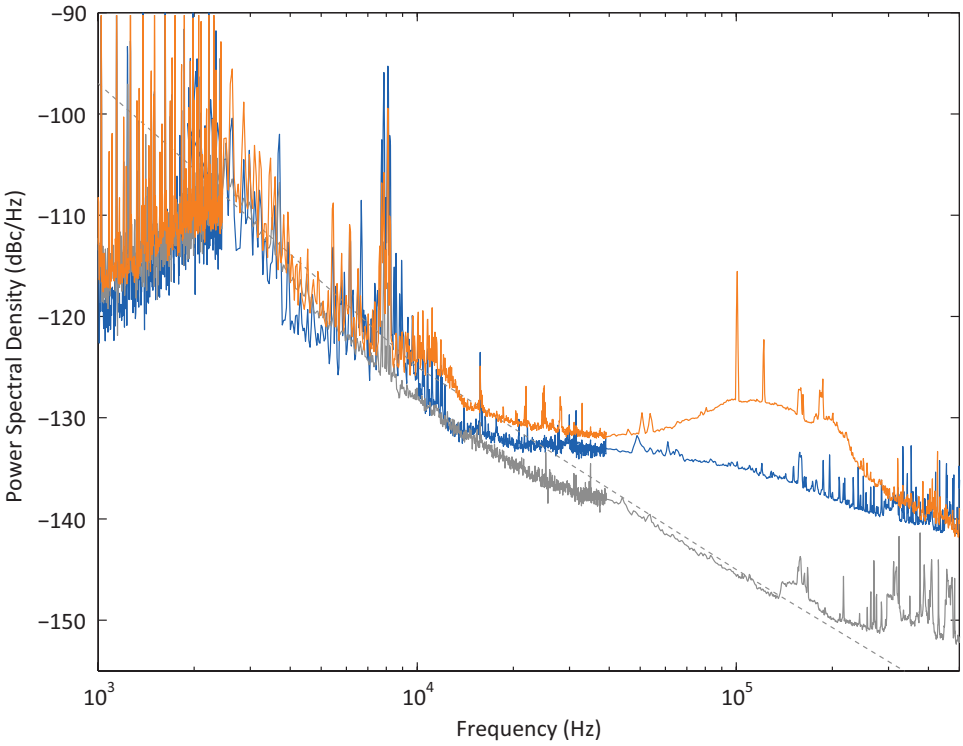

FIGURE 4.10. Laser noise measured with Optical PLL with (orange) and without (blue) the dispersive delay line. The measured VCO phase noise floor is shown (gray) in good agreement with the expected value (gray dashed).

with a low noise power amplifier (Minicircuits ZX60-100VH+). The amplified VCO signals are then connected to the RF input of the amplitude modulators, and the feedback loop is complete. To initiate the locking, the VCO is first locked to the pulse train using a photodiode collecting the residual pump light. This puts the VCO at the nominal repetition rate, allowing adjustment of the variable phase delays. The delays are use to ensure that the drive signals relative to the optical pulse train maintain a 180° offset. Once the proper phase delays are achieved, the error signal from the Optical PLL is restored, and the frequency lock is initiated. The phase noise of the VCO is then measured by mixing with a tracking oscillator as described in Appendix C.

To test the performance of the Optical PLL system, we first couple the pulse train into a short length of fiber, bypassing the dispersive delay line. This will allow us to characterize the

performance of the measurement system by observing the timing jitter of the laser oscillator alone, which will provide a limit on the performance of the system. The other limit will be imposed by the electronics used in the measurement system. The phase noise Power Spectral Density (PSD) is shown in Fig. 4.10 with and without the dispersive delay line. The phase noise floor reached about -130 dBc/Hz, limited in this case by optical power incident on the detector. The influence of the dispersive delay line can be seen in the difference between the two noise floors, as there is a slight decrease in noise when the long fiber is removed, likely due to the increase in optical power (as the loss in the fiber is ~0.2 dB/km). The other difference of note is the prominent gain peak that can be seen at about 100 kHz, due to the increased gain necessary to compensate for the fiber loss. The noise floor could be reduced by increasing the power at the detector, which could be accomplished at several points in the experiment. The amplitude modulators themselves introduce about 5 dB of loss, though modulators with only 3 dB of loss are commercially available. The transmission of the objectives used to focus onto the sample is quite low at our wavelength, as they objectives were designed for visible light, so the focusing and collection efficiency could be vastly improved by better matching the optics to the laser.

To examine further the impact of power on the Optical PLL, we'll temporarily bypass the Raman setup, and couple the laser beam directly into the long optical fiber. We'll then vary the power into the fiber using a variable attenuator and measure the phase noise floor. The experimental setup and powers used in this data set are the same as those used in the single diode case, shown in Fig. 4.6. The power dependance is important in this setup as not only does it impact the noise floor, but as power is shifted continuously from the pump to the probe arm to investigate the effect of lower pump powers, the predicted shot-noise limited

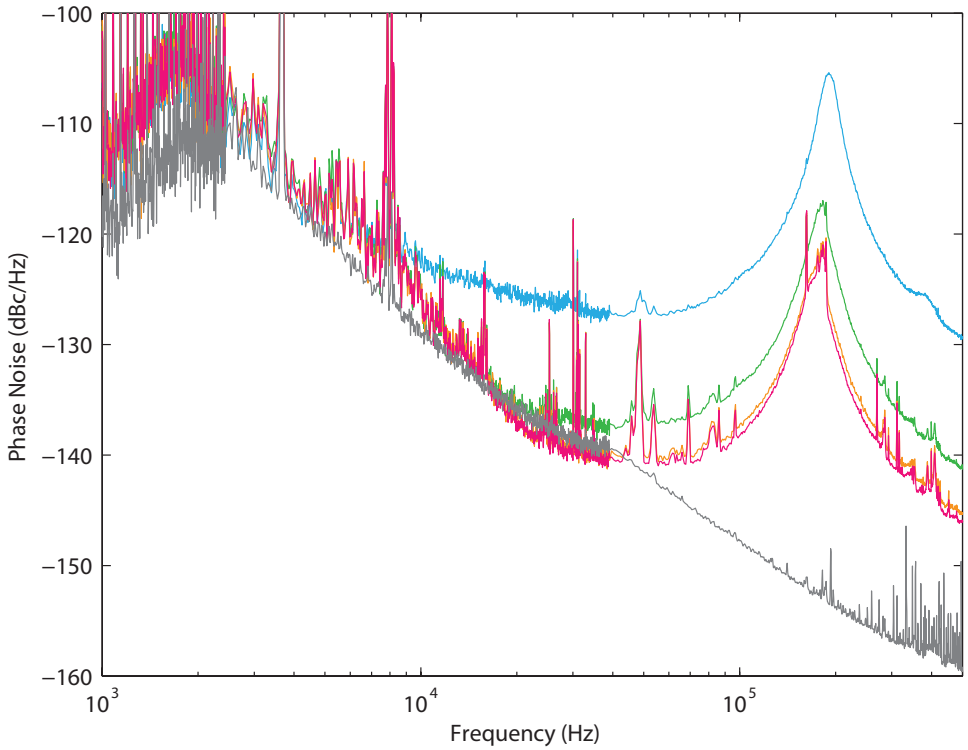

FIGURE 4.11. Phase noise floor for the Optical PLL system, showing a decrease in noise as power increases for the first few power levels. After this, the noise floor does not fall off with power, as expected from Eq. 4.12, but rather is limited by excess noise introduced by the detection. The power levels used here are the same as used in Fig. 4.6 to allow direct comparison. The distinct peak at high offset frequency is due to the servos limited bandwidth at this high gain level.

phase noise will be a function of pump (probe) power. The results of this test are shown in Fig. 4.11, and for the first two measurements show a decrease in noise floor with increasing power, as expected. However, further increases in power don't result in changes to the noise floor, as the noise floor is now being limited by some other component that has dominated the shot noise contribution. The limiting factor in this case is likely excess noise from the servo controllers output stage, as voltage noise on the output stage will manifest as phase noise on the VCO signal.

While the performance of the Optical PLL has not reached the theoretical shot-noise limited levels, the technique could still be quite sensitivity in spite of the higher noise floor shown

in Fig. 4.11. As can be seen, there is a prominent gain peak shown near the high frequency edge of the measured data. With higher optical powers, and thus higher RF powers, lower gain levels could be used in the feedback loop, providing for a larger, flatter gain spectrum lessening the gain peak in the measured phase noise. We may also be able to reduce the phase noise by replacing the optical detectors with those able to operate at higher power, as in [27], or by varying the optical power and measuring the amplitude to phase noise conversion to ensure it is minimized, as in [33]. Both these would ensure there is less noise to be canceled by the Optical PLL.

The Optical PLL components could also be improved. Using modulators with lower insertion loss would allow large modulated power incident on the photodiode. The phase depth of the modulation could also be improved by scaling to higher RF powers driving the modulators, replacing the modulators with models featuring lower values of V_π, or both. We could also implement the Sagnac experimental architecture, following [34], which uses a single modulator, as that would ensure that the optical properties of the two modulation paths are identical and ensures noise cancellation.

We'll next verify that the Raman measurements setup works as expected, and that the measurements are subject to the measured noise constraints, after which components can be upgraded and excess noise sources eliminated to allow the system to reach the numbers predicted in the previous section.

We now measure the phase signal using a lock-in amplifier while scanning the pump-probe delay , as in Chapter 3. The measured voltage $V_{\text{meas.}}$ is proportional to the phase difference between the Optical PLL signal and the reference oscillator though the conversion slope of the double balanced mixer, $K_{\text{d,mix.}}$, as $V_{\text{meas.}} = K_{\text{d,mix.}}\Delta\phi$. Rearranging, we can write the frequency

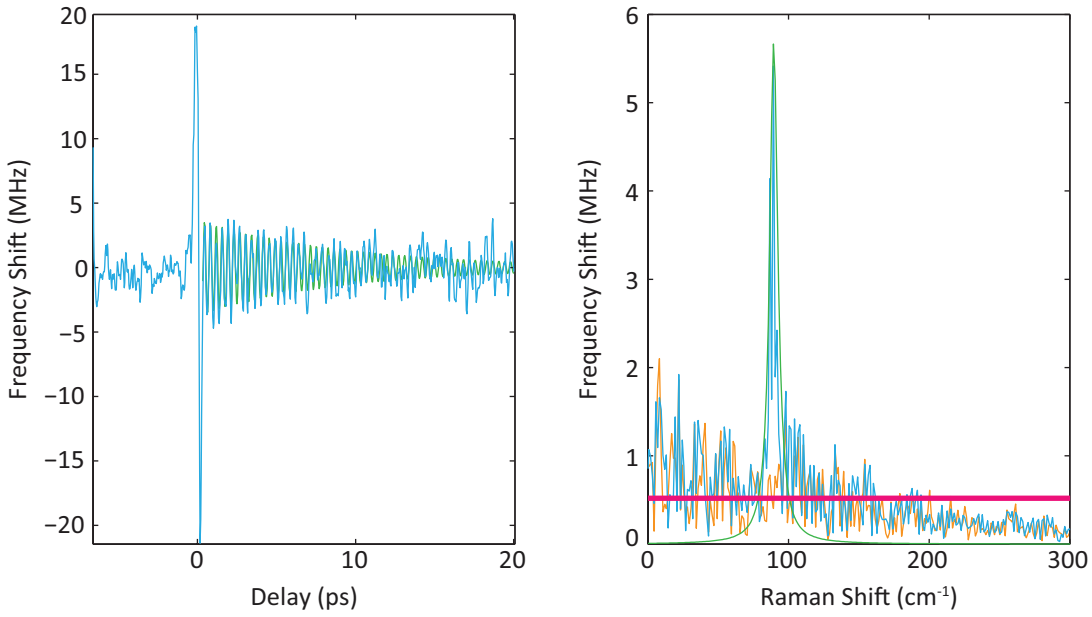

FIGURE 4.12. (a) Raman signal measured as a function of pump–probe delay using the Optical PLL (blue). The temporal data is then processed using the LPSVD algorithm, and the predicted trace plotted (green). (b) The Lorentzian Raman line from the predicted parameters is plotted (green) along with the Fourier transform of the temporal data (blue) and the residual noise left by subtracting the predicted trace from the data and Fourier transforming (orange). The theoretical Optical PLL noise floor is calculated using the measured RF noise floor, shown in Fig. 4.10, and shown as a solid line (red).

shift as

$$\delta\omega = \frac{V_{\text{meas.}}}{2\pi m f_r \varphi_2 K_{\text{d,mix.}}} \tag{4.14}$$

where $\Delta\phi$ is the phase difference as given by Eq. 4.10. The phase signal can then be related to the frequency shift through the repetition rate (f_r) and the GDD (φ_2). However, an exact value for the GDD is unknown in the experimental setup, as the length and exact dispersion of this fiber are both unknown. While the GDD of a short length of fiber and the length of the fiber could be measured, these measurements are quite cumbersome to make and their accuracy could still be suspect. To avoid this, we calibrate the instrument by simply relating the signal measured using the Optical PLL to a measurement made using the filter-based approach. This approach gives a reliable cross calibration between the two techniques, and as the shift in the

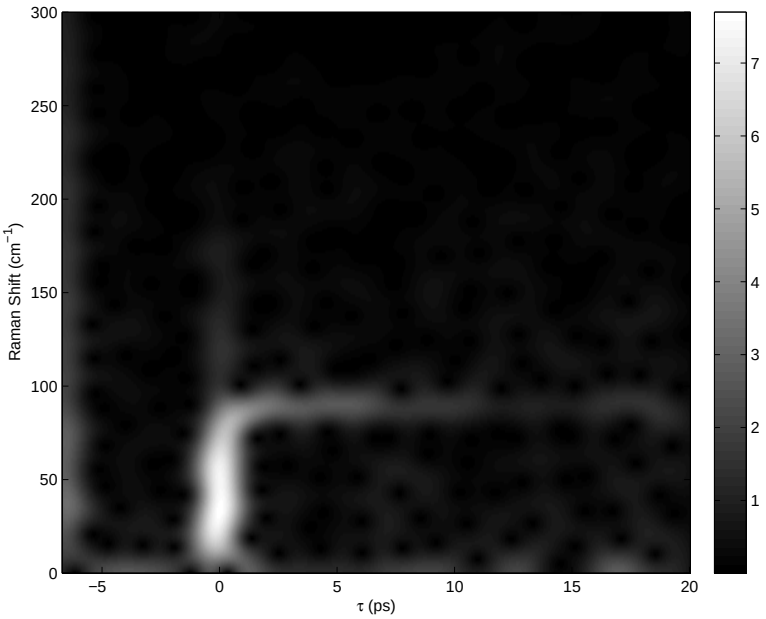

FIGURE 4.13. Gabor transform of pump-probe trace for BGO sample, using the same pump power as in Chapter 3

filter based approach is subject only to the spectrometer calibration, the absolute calibration of both techniques should be quite good. A pump-probe delay scan of the BGO crystal is taken at a pump power of 3 mW, yielding the data shown in Fig. 4.12. The measured data shows good agreement with the predicted noise floor for this data, though the noise floor isn't quite flat, indicating a deviation from the white noise expected in the shot noise limit.

To observe the point at which the Raman signal becomes equal to the noise (a signal to noise ratio of 1, as we used in the predictions), we'll process the data using a Gabor transform, in which small sections of the data are selected using a Gaussian window and Fourier transformed, giving the power spectrum at different delay values. The full Gabor transform can be seen in Fig. 4.13, and line outs from the transform shown in Fig. 4.14 for a delay very near time zero and a delay chosen to be the point at which the Raman line's peak is equal to the noise peaks surrounding it. The peak height at this point can be seen to be approximately 450 kHz, in reasonable agreement with the expected minimum shift value

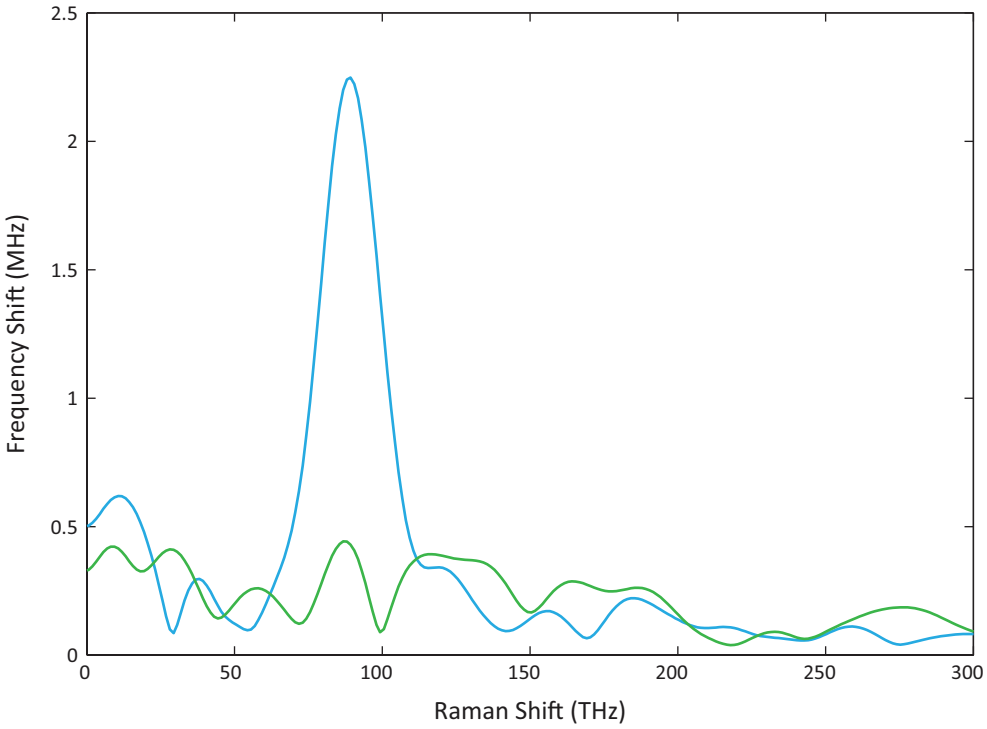

FIGURE 4.14. Line outs from the Gabor transform (Fig. 4.13) showing two traces, one at a delay very near time zero (blue) and the other at a delay chosen to be the point at which the Raman line's peak is equal to the noise peaks surrounding it (green).

for a power noise floor of -130 dBc/Hz. The decrease in spectral resolution in this data as compared to the Raman spectrum shown in Fig. 4.12 is due to the width of the Gabor window used. As we want a window narrow enough to give reasonable sampling in terms of delay, we necessarily reduce the resolution in the Fourier domain. However, the peaks in the Raman spectrum are still easily identifiable.

This sensitivity represents only a few fold increase over the sensitivity of the filter based approach. However, while the filter based approach has reached its fundamental noise-limited sensitivity, the current operation of the Optical PLL is sub-optimal. The phase noise floor is almost 20 dB above the shot-noise limited floor, with the noise floor currently being limited by other components in the PLL. One likely limiting factor is the gain of the servo loop itself. We can see a clear gain peak near 100 kHz in Fig. 4.10. If we can increase this servo bandwidth,

pushing the gain peak out of the region of interest, we can not only decrease the noise floor but this would also allow us to operate at higher offset frequencies. At higher offsets, the phase noise performance of the VCO is better. This can be seen in Fig. 4.10, where the noise floor is limited to the phase noise of the reference oscillator the noise floor falls at 20 dB per decade, so we should see big improvements by moving to higher offset frequencies. Using the same VCO as in our current setup, but pushing the modulation frequency from 50 kHz to near 1 MHz would decrease the phase noise floor from the VCO to -165 dBc/Hz. This would be below the shot noise limited noise floor for the current setup. To achieve the full -165 dBc/Hz, the optical power would need to be increased to at least 1 mW, or the optical power could be increased by a smaller amount and the RF power increased as well. Increasing the optical power could be as easy as replacing the objectives or modulators with lower loss models, improving the fiber coupling efficiency through better matching the beam to the collimator, or decreasing the fiber length.

CHAPTER 5

Spatial Frequency Modulation for Imaging (SPIFI)

Optical imaging is used across a broad range of scientific disciplines. Many systems can be imaged using Silicon Charge-Coupled Device (CCD) or Complementary Metal–Oxide–Semiconductor (CMOS) devices, which leverage years of development to offer excellent performance and relatively low cost. However, many interesting systems exist outside of the absorption band of Silicon, which require detection with exotic materials. These detectors are often limited, either by technology or by cost, to relatively few elements. It is thus advantageous to image using only a single element detector. While this is easily accomplished by raster-scanning a point focus throughout a sample, this leads to slow update rates and limits the observation of dynamics that occur faster than the scan time.

To reduce the acquisition time, we multiplex spatial information into the electronic spectrum of the detector, as single element detectors often have fast response times, and thus wide available electronic bandwidth. The modulation technique we use was first demonstrated for application to imaging in the 1990s [35], which grew out of the use of such modulators for target tracking in the sidewinder missile program [36, 37]. Other masks types were also considered, including a discrete frequency mask [36], as we employ later for two dimensional modulation, and a mask consisting of a rapidly scanning aperture [38] used to temporally multiplex line images for increase 2D acquisition speed.

More recently, we demonstrated the application of the imaging technique not only to transmissive linear imaging, but also to linear fluorescence[39] and nonlinear fluorescence[40]. The ability to use this rapid line scan technique in these microscopy configurations opens up new possibilities in imaging in turbid media, as the speed increase allows much more

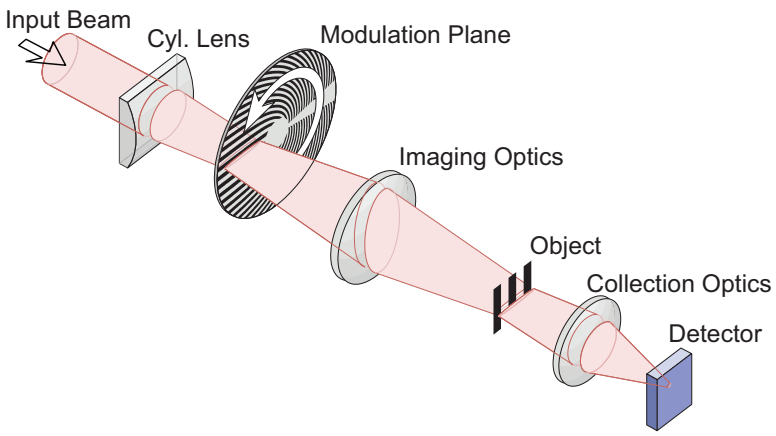

FIGURE 5.1. Schematic of one dimensional SPIFI setup

rapid dynamics to be captured. This increase in imaging speed is advantageous even where array detectors are available, and opens new possibilities to imaging in regimes where array detectors are unavailable or prohibitively expensive.

Imaging with array detectors in scattering media is limited by the crosstalk between signals from different areas of the sample being scattered to the same pixel in the array detector, rapidly degrading the imaging fidelity of the system. As the SPIFI signal encodes its position in the temporal signal, through modulation, it is largely insensitive to scattering once the object transmission function has been imprinted on the beam, all that is necessary is to collect a representative sample of the scattered light [41].

5.1. One Dimensional SPIFI

The foundation of the SPIFI method is the encoding of object spatial information on to a line focus by modulation of the line focus at different frequencies across different lateral positions. Following the derivation presented in [39], we consider a beam that has been focused to a thin line, written

$$E_{\text{ex}}(x,t) = E_0 u(x) e^{\iota\omega_0 t}$$

where $u(x)$ is the normalized spatial profile of the coherent illumination field along the line focus and ω_0 is the optical angular frequency. This field is passed through (or reflected off) a modulator described by a function $m(x,t)$. The object transmission function is given (in one dimension) as $g(x)$, which describes either the distribution of absorbers (or emitters) along the beam dimension. It is this function that the SPIFI technique will recover in order to describe the object. This leads to a beam given by

$$E_{\text{obj}}(x,t) = E_0 u(x) m(x,t) g(x) e^{\imath\omega_0 t}$$

This x dependent field is then collected by a single element detector, leaving only a temporally dependant signal after integration over the spatial coordinate that takes the form of $s_{\text{obj}}(t) = \gamma \int I_{\text{obj}}(x,t)\mathrm{d}x$ where the prefactor γ has been introduced to account for collection factors, including detector efficiency. The intensity of the object beam can be written as

$$I_{\text{obj}}(x,t) = I_0 |u(x) m(x,t) g(x)|^2 \tag{5.1}$$

where $I_0 = \frac{1}{2} nc\varepsilon_0 |E_0|^2$, and we have required that the detector exhibits a flat frequency response across the bandwidth of the SPIFI signal, and further that the detector is large enough to capture the full extent of the beam.

The modulation pattern we choose for this work is a radially dependent cosine, the frequency of which varies linearly along the radial axis of the modulator. The transmission function of the modulator is given as

$$m(x,t) = \frac{w(t)}{2}\left[1 + \cos\left(2\pi\kappa x t\right)\right]. \tag{5.2}$$

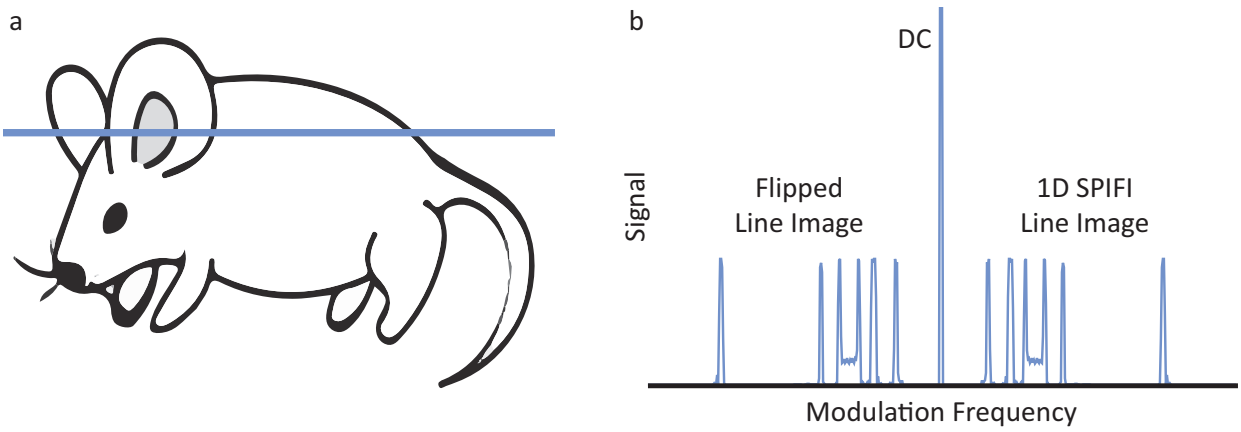

FIGURE 5.2. Cartoon showing SPIFI operation in 1D. The (a) blue line indicates a slice of the larger image being mapped into (b) the frequency domain of a photodiode signal.

The application of this time-window, $w(t)$, leads to an object beam of

$$E_{\text{obj}}(x,t) = \frac{E_o}{2} u(x)g(x)w(t)\left[1 + \cos(2\pi\kappa x t)\right] e^{\imath\omega_0 t}. \tag{5.3}$$

The collected intensity is given by squaring this field, leading finally to

$$I_{\text{obj}}(x,t) = I_0 \frac{1}{4} |w(t)u(x)g(x)|^2 \left[\frac{3}{2} + 2\cos(2\pi\kappa x t) + \frac{1}{2}\cos(4\pi\kappa x t)\right] \tag{5.4}$$

The SPIFI signal $s_{\text{obj}}(t) = \frac{1}{2} I_0 \gamma \left[s_0(t) + s_1(t) + s_2(t)\right]$ is made up of three terms, the 'DC' term, $s_0(t) = |w(t)|^2 \int \frac{3}{4}|u(x)g(x)|^2 \mathrm{d}x$ is the overlap integration of the excitation beam and object. The time-dependent signals s_1 and s_2 are the first and second harmonic bands of the modulation frequency, with

$$s_1(t) = |w(t)|^2 \int |u(x)g(x)|^2 e^{\imath 2\pi\kappa t x} \mathrm{d}x + \text{c.c.} \tag{5.5}$$

$$s_2(t) = \frac{1}{4}|w(t)|^2 \int |u(x)g(x)|^2 e^{\imath 4\pi\kappa t x} \mathrm{d}x + \text{c.c.} \tag{5.6}$$

The first and second harmonic sidebands contain the same information about the signal. We'll ignore for this analysis the presence of the second harmonic sideband, as well as any other harmonic content that may arise from the use of non-cosine masks (such as the binary masks used experimentally, which will be discussed later). These harmonics can be trivially removed through electronic filtering of the photodiode signal, or removed from the Fourier transform of the signal in post-processing. Shifting the coordinate system to centroid of the beam by the substitution $x' = x - x_c$ lets us write the sideband signal in the form of a spatial Fourier transform, where the spatial frequencies are given as $f_x \to \kappa t$. This takes the form of

$$s_1(t) = |w(t)|^2 e^{\imath 2\pi\kappa x_c t} \int |u(x')g(x')|^2 e^{\imath 2\pi\kappa t x'} \mathrm{d}x' + \text{c.c.} \tag{5.7}$$

Writing the Fourier transform operator $\mathfrak{F}\{\}$,

$$\mathcal{G}'(f_x) = \int \left|u(x)g(x)\right|^2 e^{\imath 2\pi f_x x} \mathrm{d}x \equiv \mathfrak{F}\{|u(x)g(x)|^2\}, \tag{5.8}$$

we return to the temporal frequency of the first sideband,

$$s_1(t) = 2|w(t)|^2 |\mathcal{G}'(\kappa t)| \cos\left(2\pi f_c t + \angle\mathcal{G}'(\kappa t)\right) \tag{5.9}$$

where $\angle\mathcal{G}'$ is the phase of the spatial frequency distribution, $\mathcal{G}'$, and the center frequency is $f_c = \kappa x_c$.

The Fourier transform of the temporal signal, $\hat{S}_1(f) = \mathfrak{F}\{s_1(t)\}$, gives an electronic spectrum showing the positive and negative sidebands of the fundamental SPIFI signal.

$$\hat{S}_1(f) = \kappa^{-1}\hat{S}_{1+}(f) + \kappa^{-1}\hat{S}_{1-}(f)$$

The sidebands are the spatial extent of the illuminated intensity limited in resolution by convolution with the temporal window. The upper side band can be written as the convolution

$$\hat{S}_{1+}(x' = f\kappa^{-1}) \quad = \quad \mathcal{W}(\kappa x') \circledast \left|u(x')g(x')\right|^2 \tag{5.10}$$

where f is the frequency of the electronic signal, and $\circledast$ is the convolution operator. The Fourier transform of the temporal window defines the equivalent "point spread function" of the system given by $\mathcal{W}(x') = \mathfrak{F}\{|w(t)|^2\}_{f=x'\kappa^{-1}}$.

This form of the point spread function gives the response of the imaging system to the finite time window of the modulator. To examine exactly how this finite time window impacts the resolution of the SPIFI imaging system, we consider the resolution as given by the numerical aperture of the system. The numerical aperture is defined as $NA = n\sin\theta_{\max}$, where n is the index of refraction and $\theta_{\max}$ is the largest angle collected by the imaging system. The spatial frequencies of an object are given (by definition [42]) as $f_x\lambda = \sin\theta$. Substituting this spatial frequency in to the expression for numerical aperture, we arrive at an expression for numerical aperture given by

$$NA = n\lambda f_{x_{\max}}$$

where $f_{x_{\max}}$ is the maximum spatial frequency collected. As above, the spatial frequencies in the SPIFI imaging systems are linearly related to time by the chirp rate κ by $f_x = \kappa t$. Thus, the maximum spatial frequency is simply κ times T_m, the duration of the modulator time-window, $w(t)$. Finally, the numerical aperture is

$$NA = \frac{1}{2}\lambda\kappa T_m$$

The Rayleigh spatial resolution is (in 1D) $\delta x = \lambda(2\mathrm{NA})^{-1}$, which for SPIFI gives a resolution

$$\delta x = (\kappa T_m)^{-1}, \tag{5.11}$$

the highest spatial frequency sampled on the mask.

The number of spatially resolved points, N, is given by the beam width, W divided by the spatial resolution, δx. Making the substitutions for SPIFI, the number of spatial points is $N = W/\delta x = \kappa W T_m$, which is the same as the space-spatial frequency bandwidth product, $N = 2W f_{x_{\max}}$. For the temporal signal, the number of points is the modulated bandwidth, Δf_m, divided by the resolution bandwidth, δf. The resolution bandwidth δf is the inverse of the acquisition duration, T_m, leading to the time-bandwidth product, $N = \Delta f_m T_m$. For SPIFI the signal bandwidth is

$$\Delta f_m = \kappa W, \tag{5.12}$$

and the resolution bandwidth of the trace is T_m^{-1}, giving a temporal number of points $\kappa W T_m$, identical to the spatial-spatial frequency bandwidth product. The limit on both the number of points and the resolution is seen to be based only on the modulator design and is independent of the wavelength of the illumination.

As the resolution of the system is tightly linked to the design of the modulation mask, we'll briefly recast some of the parameters more directly in terms of the modulator. For these experiments, we use one of a family of patterns defined first by [43], shown in Fig. 5.3 and written as

$$m(R,\theta) = \frac{1}{2} + \frac{1}{2}\cos\left[(k_0 + \Delta k R)\theta\right] \tag{5.13}$$

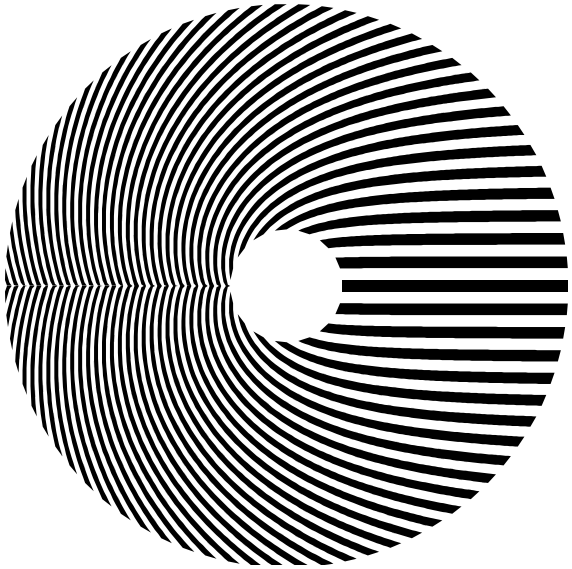

FIGURE 5.3. Example mask pattern of Eq. 5.13 with chirp rate $\Delta k = 3\ \mathrm{mm}^{-1}$.

where R is the radial coordinate relative to the center of the disk and θ is the angular coordinate. The beam to be modulated samples the modulation pattern across a radial line such that $R = x$. Spinning the mask at a constant angular velocity $\mathrm{d}\theta/\mathrm{d}t = 2\pi f_r$ so that we can make a substitution $\theta \to 2\pi f_r t$ in Eq. 5.2. provides the requisite linear chirp in modulation frequency expressed in Eq. 5.2, where we can make the identification $\kappa = f_r \Delta k$, with an additional offset of the modulator frequency given by $\kappa_0 = f_r k_0$. In the masks used, the pattern spatial frequency offset was $k_0 = 0$. Adjusting this parameter allows the center frequency of the modulation band to be increased without requiring an increase in the motor spin rate (which would also increase the modulation bandwidth). This flexibility can allow the modulation band to be moved away from low-frequency noise while being kept below the sampling limit of the digitization board.

The limiting factor in moving to higher frequencies using this offset is this requires the printing of higher spatial frequencies on the physical mask. As the resolution of the system is limited to the highest spatial frequency on the mask (or the Numerical Aperture (NA)

of the imaging system, whichever is lower), imposing a limitation on the print resolution equivalently caps the potential range of spatial frequencies. Thus, the maximum chirp rate able to be printed is just the inverse of the print resolution. Since print resolution ultimately limits SPIFI resolution, we often choose mask that operate at the highest chirp rate available for a given printing system, and are thus unable to use the k_0 to adjust the center of the frequency band. The spin rate of the modulator can still be adjusted to operate in a relatively low noise region of the electronic spectrum.

The time-window of the modulator is given by $T_m = \Delta\theta/(2\pi f_r)$, where $\Delta\theta$ defines the angular width of the linearly-chirped modulator pattern. This gives a spatial resolution of $\delta x = 2\pi/(\Delta\theta\Delta k)$, a modulation bandwidth of $\Delta f_m = f_r W \Delta k$, the number of resolved points $N = \Delta\theta W \Delta k/(2\pi)$, and a center modulation frequency of $f_c = f_r(k_0 + \Delta k x_c)$, where x_c is the beam center position on the modulator disk.

5.2. Fluorescent SPIFI

The previous analysis assumed the contrast function was just intensity transmission. However the analysis is still valid for linear and nonlinear fluorescence, as long as the modulation of the fluorescence signal follows the modulation of the illumination light. As the fluorescent light is emitted spontaneously from the excited state, fluorophores are characterized by their lifetime—the average time a fluorophore spends in the excited state before decaying to the ground state. If the timescale of the driving modulation is short compared to fluorescence lifetime, the emitted light will exhibit a phase shift and a decrease in modulation depth.

To examine this condition, we'll look at the response of fluorophores to modulated signals. The rate equations for fluorphores driven by sinusoids have been solved [44] for application to fluorescence lifetime imaging, in which the phase and amplitude response of a fluorphore

is measured relative to a sinusoidally modulated illumination signal in order to identify the fluorophore. The depth of modulation and phase of the emitted fluorescence intensity can be written as $m_{\mathrm{F}} = \left[1 + (2\pi\kappa x\tau_{\mathrm{F}})^2\right]^{-1/2}$ and $\phi_{\mathrm{F}} = 2\pi\kappa x\tau_{\mathrm{F}}$, respectively, such that the collected intensity from the fluorescent object is written as

$$I_{\mathrm{obj}}(x,t) = I_0\frac{1}{4}|w(t)u(x)g(x)|^2\left[\frac{2+m_{\mathrm{F}}^2}{2} + 2m_{\mathrm{F}}\cos(2\pi\kappa xt + \phi_{\mathrm{F}}) + \frac{m_{\mathrm{F}}^2}{2}\cos(4\pi\kappa xt + 2\phi_{\mathrm{F}})\right],$$

in comparison to the equation for a transmissive object, given in Eq. 5.4. If the fluorophore of interest exhibits a single exponential decay, then τ_{F} is just the fluorescence lifetime. If it is non-exponential or multi-exponential, then τ_{F} is the apparent lifetime, given by a weighted sum of the decay components [45].

If we select as our frequency limit the point where the modulation depth drops to 10%, we can then write the maximum SPIFI frequency usable for a fluorophore with lifetime τ_{F} as $f_{\mathrm{max.}} = 3\sqrt{11}/(2\pi\tau_{\mathrm{F}})$. As fluorescence lifetimes are typically near 10 nanoseconds [45], this puts the maximum SPIFI frequency over 100 MHz. For the spinning disk implementation described in this work, with a typical bandwidth on the order of 100 kHz, we can expect no appreciable loss of modulation depth and negligible phase accumulation for a reasonable lifetime. If the SPIFI technique were applied using high speed modulators, the lifetime could impose an upper limit—though the available bandwidth would still be quite generous.

Methods. The samples used in the measurement of the SPIFI fluorescence images, an example of which is shown in Fig. 5.4, were made by patterning fluorescent ink onto glass slides using a rubber stamp. To improve adhesion of the ink, the slides were first sprayed with a coat of aerosol hair spray. Inhomogeneity in the ink distribution can be seen in both the absorptive and fluorescent images. The samples were illuminated using a 532 nm

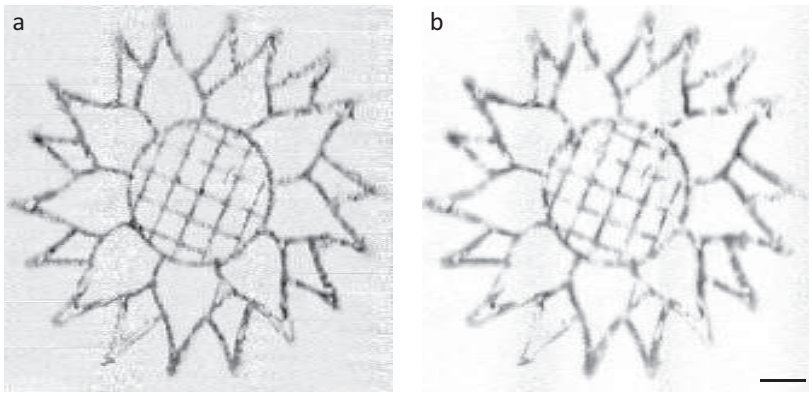

FIGURE 5.4. SPIFI images of fluorescent ink stamped on a glass slide, in both the (a) fluorescence absorptions and (b) fluorescence emission modes. Scale bar is 2 mm.

continuous-wave solid-state laser (Coherent DPSS 532) with 23 mW average power. The beam spatially filtered and collimated to an ≈ 20 mm diameter before being focuses to the modulator with a 50 mm focal length cylindrical lens. The modulator used in this work had a chirp rate of Δk=7/mm and was spun at 30 Hz. The modulation plane was imaged to the object plane using a 3:2 reducing telescope. After passing through the object, the fundamental beam and the fluorescence were collected in the forward direction using a 50 mm lens. The fluorescent and fundamental light were separated using a 600/mm grating and the light collected simultaneously using a pair of Silicon photodiodes (Thorlabs DET10A). The detector used for the fluorescent light had a 600 nm long pass filter placed in front of it to suppress spurious signal from scattered fundamental light.

As these fluorescent images were taken as SPIFI line images, the sample was translated using a motorized translation stage perpendicular to the SPIFI line dimension, allowing the measurement of two dimensional images. We used large objected for this first demonstration, and so to capture an image of the entire stamp, we measured three such line scans, with the sample translated laterally between each, which were combined in post processing to yield the image seen in Fig. 5.4. Artifacts of this stitching process are evident on the left side of the

image, as the overlap was not great enough to suppress the edge effects caused by the fall off in beam intensity near the edges.

5.3. SPIFI Spectrometer

SPIFI replaces a line camera with a single-element detector by applying a position dependent temporal intensity modulation to a line focus, then Fourier transforming the electronic signal from the single-element detector to recover the spatial information. We'll expand this to a spectrometer using the setup shown in Fig. 5.5. While array based spectrometers are widely available in the visible, the options for array spectrometers falls off quickly outside of the visible. The cost of arrays is generally higher for devices in the infrared, so a number of technologies exist to measure spectra using a single element detector. Common options include scanning monochromators [46] and Fourier transform spectrometers [47]. Both systems require mechanical scanning, leading to long acquisition times. Here, we apply the one dimensional SPIFI imaging system to replace grating or stage scanning, leading to improvements in speed.

In the simplest SPIFI spectrometer measurement, the optical spectrum of the input light is spatially dispersed using a grating and then a position–dependent temporal modulation is applied and the beam is simply collected on a photodetector. The optical spectrum can then be recovered from the electronic spectrum of the photodetector signal. With this same modulator configuration, we can also perform hyperspectral imaging by illuminating a sample with this spectrally modulated beam. The spectrum of the collected light would then have been modulated by the response of the sample before being collected, encoding that spectral response into the RF spectrum of the signal. We'll consider briefly the design parameters, merging the theory of standard spectrometers with the SPIFI theory of Section 5.1.

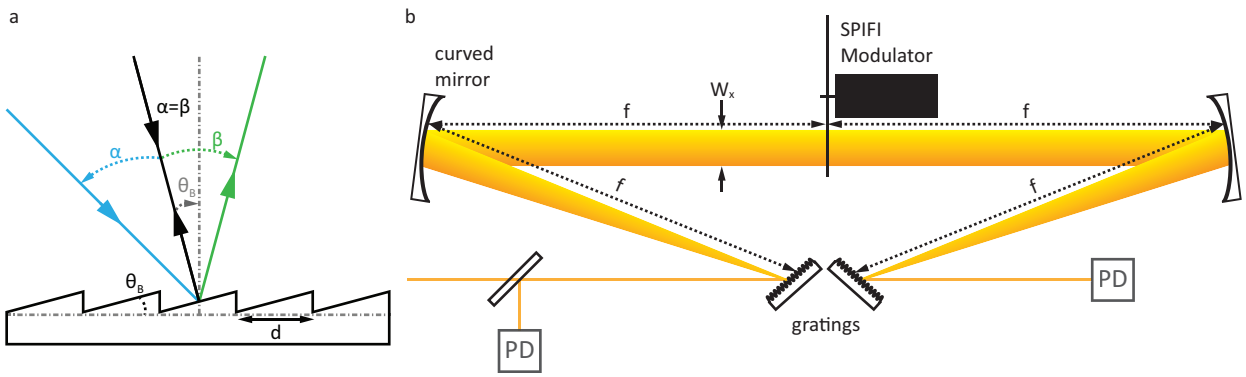

FIGURE 5.5. Diagram of a blazed grating (a) showing relevant parameters for the SPIFI spectrometer and (b) diagram of the spectrometer setup showing both reflective and transmissive beam paths. PD is photodiode and SPIFI modulator is a mask, as given by Eq. 5.13 and shown in Fig. 5.3, mounted on a motor.

Theory. The SPIFI spectrometer is a standard grating spectrometer, with the array detector replaced by the SPIFI modulator and a single element detector. The equation which governs the diffraction from a grating is

$$\sin(\beta) + \sin(\alpha) = Gm\lambda$$

where m is the order of diffraction, G is the grating groove density, λ is the wavelength of incident light, α and β are the angles of incidence and diffraction, respectively, both with respect to the grating normal, as shown in Fig. 5.5(a). Assuming the incidence angle to be constant, the angular dispersion can be calculated from the grating equation [48] as

$$\frac{\partial\beta}{\partial\lambda} = \frac{mG}{\cos(\beta)} \equiv D.$$

Operation in the Littrow configuration (where the angle of incidence is equal to the angle of diffraction) this angular dispersion becomes simply $D = 2/\lambda \tan(\beta)$. Placing a lens a focal length away from the grating, and measuring the spectrum a focal length again away from the lens as shown in Fig. 5.5(b), we can translate this angular dispersion to a linear dispersion. The

linear dispersion is just given as the angular dispersion times the focal length of the collection lens. This dispersion is often written in the inverse, as the reciprocal linear dispersion

$$P = \frac{\lambda}{2f\tan(\beta)}$$

where f is the focal length of the lens. This term, usually expressed in nm/mm, expresses the change in wavelength with translation in the focal plane. Using the x width, W_x, and resolution, δx, for the SPIFI imaging system, as given in Section 5.1, we can convert these to spectral parameters using the reciprocal linear dispersion. Thus, the bandwidth of the SPIFI spectrometer is given by $\Delta\lambda = PW_x$ and the resolution is given by

$$\begin{aligned}\delta\lambda &= \frac{P}{\Delta k} \\ &= \frac{\lambda}{2f\Delta k\tan(\beta)}.\end{aligned} \tag{5.14}$$

This gives the SPIFI-limited performance, based only on the grating, lens, and mask parameters. As with all grating spectrometers, other design considerations may impact spectrometer resolution [49, 50].

In the previous analysis, we've assumed that the photodiode and digitizer have sufficient bandwidth to capture all relevant frequencies and that the laser repetition rate is high enough that the source appears quasi-CW. However, targeting this toward use in the MIR, we must consider the effect of low-repetition rate sources as many MIR systems operate at low frequencies (on the order of kHz). This low-frequency pulsed operation limits the maximum temporal frequency to be used in the SPIFI signal to be half of the repetition rate, and not half of the sample rate as we've examined before. By setting the signal bandwidth, Eq. 5.12, equal

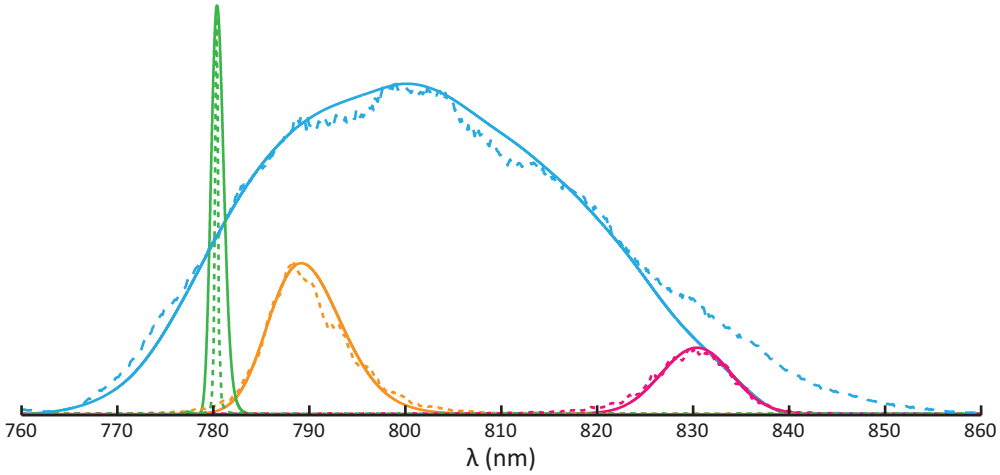

FIGURE 5.6. Spectra of a Ti:Sapphire oscillator taken with the SPIFI spectrometer (solid) and a CCD-based grating spectrometer (dashed). The mode-locked oscillator spectrum (blue) is shown along side the spectra transmitted through two bandpass filters, centered at 790 nm (orange) and 830 nm (pink). The narrow CW oscillator spectrum (green) was used to calibrate the SPIFI spectrometer.

to half the repetition rate, we can formally state this requirement as $\kappa = f_0/(2W)$, where f_0 is the repetition rate of the laser. The update rate, t_{FR}, of the spectrometer can then be written as

$$t_{\mathrm{FR}} = \frac{2W}{f_0}\frac{P}{\delta\lambda}, \tag{5.15}$$

in terms of the modulator width W, chirp rate Δk, reciprocal linear chirp P, and desired resolution $\delta\lambda$.

Methods. To test the performance of the SPIFI spectrometer, we build a test setup to measure the spectrum of a Ti:Sapphire oscillator. The oscillator produces pulses with about 45 nm bandwidth (Full Width at Half Maximum (FWHM)) centered at 800 nm in mode-locked operation. The oscillator can also be made to operate CW, where it produces a narrow spectral peak centered at 780 nm. The beam first illuminates a 600/mm grating, causing the spectrum to spread spatially in the x direction while leaving the y dimension unchanged. A 250 mm focal length mirror placed a focal length away from the grating stops the angular spread of

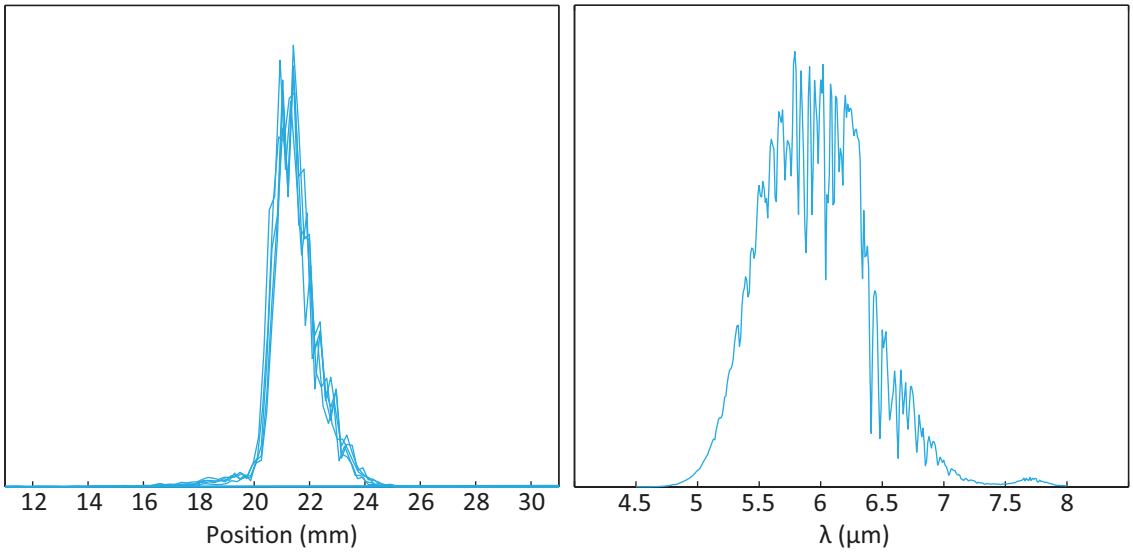

FIGURE 5.7. Sample MIR spectrum taken with (a) the SPIFI spectrometer and (b) an array spectrometer. The SPIFI spectrum is shown in position, as wavelength to position calibration data was not taken.

the spectrum and focuses the beam in y such that a spectrally dispersed line focus appears at the modulator plane. A Δk=5/mm modulator encodes the spatial location of each part of the beam (and thus, the wavelength) through a temporal modulation. The modulator disk is tilted slightly out of plane, such that when the reflected light then travels back along (and slightly below) its input path, it can be picked off by a mirror and directed on to the single element detector.

To allow comparison of the performance of the transmissive and reflective configurations, we simultaneously collect the transmitted and reflected signals using two photodiodes. The ability of the system to work in a reflective mode is important for the application of this technique to a broad wavelength span, as the transmission of the glass substrate is spectrally much narrower than the reflectivity of the aluminum features printed on the mask.

From the chirp rate of $\Delta k = 5$/mm, we expect a spatial resolution of 200 μm (from Eq. 5.11). Measuring the oscillator in CW operation gives us a point-like object in space, and we measure the resolution to be 240 μm. Converting this spatial resolution to spectral resolution, we

expect a spectral resolution of 1.2 nm (from Eq. 5.14) and measure 1.5nm (consistent with measured resolution of 240 μm).

Test spectra are shown in Fig. 5.6, compared to the spectra taken with an array-based spectrometer (Ocean Optics). The data was taken for the CW and mode-locked spectra, as well as through two bandpass filters, centered at 790 nm and 830 nm. With the CW peak used as a calibration point (to set the absolute wavelength to position mapping), the centers wavelengths agree quite well. For the filters, the transmission appears a bit narrower in the SPIFI case when compared to the grating spectrometer. The fall-off on the red side of the mode-locked spectrum is from a slight clipping on the modulator. The spectral response of the photodiode has not been corrected for, nor has the spectral response of the grating spectrometer.

An initial spectral measurement, shown in Fig. 5.7, was taken on an MIR laser system producing pulses centered at 6 μm at a 1 kHz repetition rate. The experimental setup is the same as in Fig. 5.5, though operating only in a reflective configuration due to the low MIR transmissivity of the modulator substrate. The spectral data is shown on a position axis, as the spectrometer was not calibrated in this initial test. It has also not been corrected for the spectral response of the detector or the reflectivity of the modulation mask. This initial data shows that a properly calibrated spectrometer could be used to make high-update rate, high-resolution MIR spectral measurements. It also paves the way for other spectrally dependent measurements in the MIR, such as pulse measurement using Frequency Resolved Optical Gating (FROG) or hyperspectral measurements.

CHAPTER 6

Two Dimensional SPIFI

The SPIFI imaging method allows a line image to be captured by a single element detector through temporal multiplexing. To acquire two dimensional images, we have either to scan the sample in the orthogonal dimension, as was done in Fig. 5.4, or rotate the sample to measure a set of projections from which the image can be recovered using tomographic processing [51]. In this chapter, we look at three other ways to expand the previously described SPIFI line imaging system to two dimensions, one which multiplexes many one dimensional signals and two others which measure 2D images on a single element detector.

The first approach uses a fast line camera in place of a two dimensional array detector, with the camera axis perpendicular to line focus. The camera then measures a set of SPIFI traces at different y positions, allowing a one dimensional array to do two dimensional imaging. While this still requires an array, the reduction in pixel count is advantageous in applications where the per-pixel cost of an array detector is high or multidimensional arrays are unavailable.

The second method we will explore is the application of two orthogonal modulators, spinning at different rates, which encodes (x, y) spatial information into a one-dimensional temporal frequency axis as the sum of the x and y frequencies. As this method requires only a single detector, we maintain the advantage of scattering immunity we saw with the one-dimensional SPIFI. This method also does not require a potentially costly multi-element detector.

The final method trades the spinning disk modulator for an array of mirrors that can be rapidly switched between two angles. Such devices are commonly employed in movie projectors, and invert the typical imaging system by switching the single source and multiplex

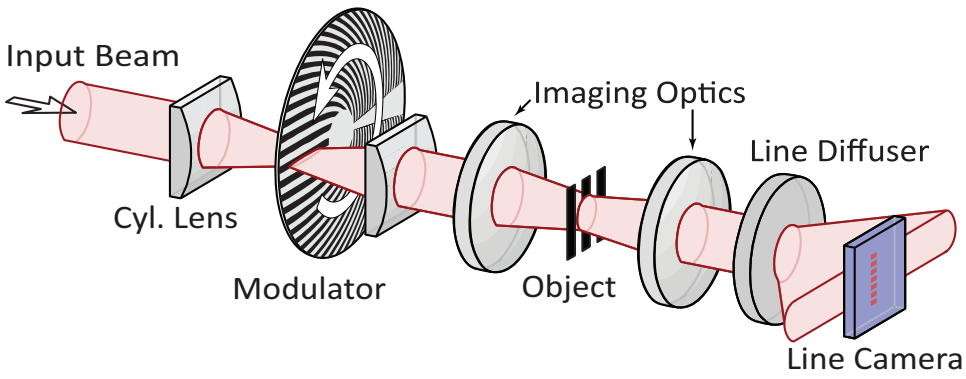

FIGURE 6.1. Schematic of the optical setup for line camera SPIFI.

detector for a multiplexed source and a single detector. This inversion is useful as the usable wavelength range of a metallic mirror exceeds the usable range of many detectors, allowing the same mirror array to be used across a broad wavelength range.

6.1. Line Camera

The simplest approach to two dimensional SPIFI is simply to use the SPIFI modulator to encode the spatial information in one dimension into the temporal trace, then use a linear array detector to collect multiple SPIFI traces simultaneously. The experimental setup for such a system is shown in Fig. 6.1. The setup is modified from the normal SPIFI setup, as shown in Fig. 5.1, by replacing the spherical imaging lens with a second cylindrical lens, collimating the beam after the x modulation instead of re-imaging the modulated line focus to the object plane. The expanded beam has the same modulation across the lateral coordinate, so when the beam in incident on an object, the object contrast function is encoded into a y dependant time signal. Such a modulation is shown in Fig. 6.2, taken from [51] in which the beam is prepared in the same way.

The light from the object is focused to a vertical line and collection with a line camera (Basler ruL 1024-57gm) at 40 kHz with an 8 bit depth. Collection of a reasonable proportion

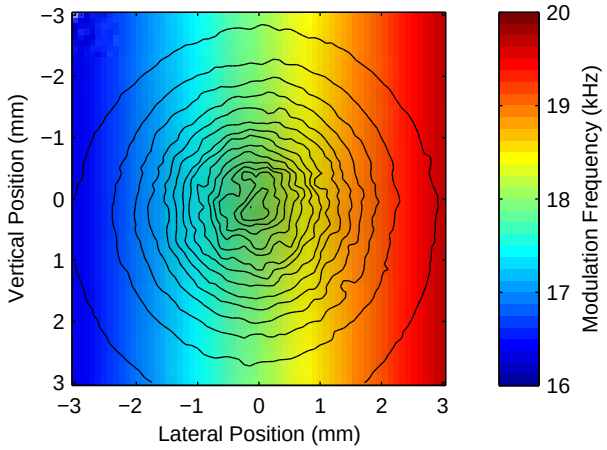

FIGURE 6.2. Modulation frequency as a function of position (gradient) with beam intensity overlayed (contours). From [51].

of the sideband and un-diffracted beam proved difficult in the optical setup used in this work. As SPIFI only requires a representative sample of the light to be collected, we turned to a scattering approach to ensure we get reasonable signal levels. While the position information in x has been encoded in frequency, the vertical position fidelity must be maintained to prevent image degradation in the y direction. To accomplish this, we used an engineered diffuser to scatter the light horizontally, but not vertically, such that we don't get blurring in the vertical dimension of the image. This allows the formation of images but also introduces structure in recovered images, owing to the grid of structures in the engineered diffuser. These structures can be eliminated by averaging several images, with the diffuser moved slightly in between each image, as shown in Fig. 6.3.

While this diffuser could be eliminated by using better collection optics, the introduction of a diffractive element to ensure image formation is another statement of the scattering immunity in the collection system. The line images are not degraded by the introduction of this massive scattering, indeed the only degradation comes in due to the imprinting of vertical

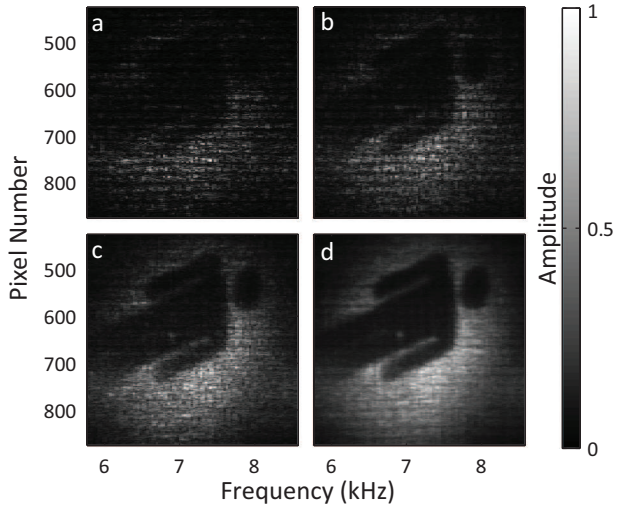

FIGURE 6.3. Retrieved image of an absorptive object (man), through averaging of (a) 1, (b) 2, (c) 5, and (d) 20 individual retrieved images, with the line diffuser moved ~250 μm along x and y between images. From [52].

structure on the images from the diffuser, as in immunity to scattering is only present in the SPIFI dimension.

6.2. Dual Disk

While the array detector allows us to expand the utility of the SPIFI line imaging method rapidly into two dimensions, the advantages of scattering immunity are lost in the y direction. In the implementation shown, we also introduced unwanted speckle structure in the recovered images. The speckle structure introduced by this line camera approach is avoided in the sample scanning approaches, either linear scanning or tomography.

To restore the scattering immunity, avoid the speckle introduced by this line camera approach, and eliminate the need for sample scanning, we expand the SPIFI approach to two dimensions using a pair of SPIFI modulators, as shown schematically in Fig. 6.4. The modulators are orthogonal to one another, the first modulating the x dimension, then the modulated horizontal line is expanded and refocused to a vertical line along y where it is

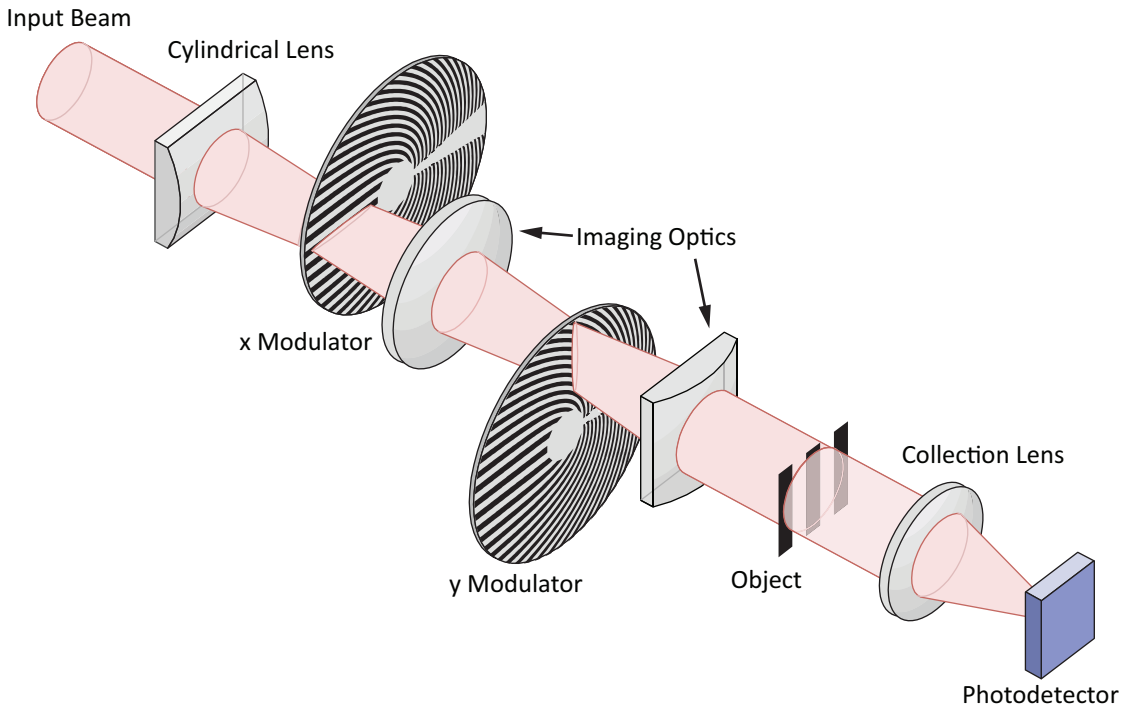

FIGURE 6.4. Optical setup of the dual-disk two-dimensional SPIFI imaging system.

modulated by the second modulator. The modulated beam is then imaged onto an object, and the beam collected on a single element detector.

The two modulators impart a spatially dependent modulation on the horizontal and vertical dimension in turn, such that each point in the object plane has a corresponding temporal modulation frequency given by the product of its x and y modulation frequencies. Here we expand the SPIFI theory to two dimensions and examine the design requirements for the modulators.

Theory. The modulation functions of the two modulators both take the form of Eq. 5.13, where we write the horizontal modulation function as $m_x(x,t) = \frac{w(t)}{2}\left[1 + \cos\left(2\pi\kappa_x xt\right)\right]$ and the vertical modulation function $m_y(y,t) = \frac{w(t)}{2}\left[1 + \cos\left(2\pi\kappa_y yt\right)\right]$. The beam full beam, $u(x,y)$, is then modulated by the product of these two orthogonal modulation functions,

$m_x(x,t)m_y(y,t)$ (the case of a direct two-dimensional modulator, $m(x,y,t)$, will be treated separately in Section 6.3).

We begin by writing the modulation function, as the product of the two orthogonal modulators, as

$$m(x,y,t) = m_x(x,t)m_y(y,t) = \left[\frac{1}{2} + \frac{1}{2}\cos(2\pi\kappa_x xt)\right]\left[\frac{1}{2} + \frac{1}{2}\cos(2\pi\kappa_y yt)\right]. \qquad (6.1)$$

We can then write the electric field as

$$\begin{aligned} E_{\text{obj}}(x,y,t) &= E_0 u(x,y)g(x,y)w(t)\left[\frac{1}{2} + \frac{1}{2}\cos(2\pi\kappa_x xt)\right]\left[\frac{1}{2} + \frac{1}{2}\cos(2\pi\kappa_y yt)\right] \\ &= \frac{E_0}{4}u(x,y)g(x,y)w(t)\left[1 + \cos(2\pi txx\kappa_x) + \cos(2\pi tyx\kappa_y)\right. \\ &\quad \left. + \cos(2\pi txx\kappa_x)\cos(2\pi tyx\kappa_y)\right] \end{aligned}$$

where $u(x,y)$ is the now two dimensional beam profile, $g(x,y)$ is the contrast function (e.g. object transmission or fluorescence distribution), and $w(t)$ is the time window of the measurement. The field can be seen to be the sum of four terms: a Direct Current (DC) term, an x projection term, a y projection term and an x–y cross term. We write the collected intensity as

$$\begin{aligned} I_{\text{obj}}(x,y,t) = \left|g(x,y)u(x,y)w(t)\right|^2 \Bigg\{ &\frac{9}{64} + \frac{3}{16}\cos\left[2\pi\kappa_x tx\right] + \frac{3}{16}\cos\left[2\pi\kappa_y ty\right] \\ &+ \frac{1}{8}\cos\left[2\pi(\kappa_x tx + \kappa_y ty)\right] + \frac{1}{8}\cos\left[2\pi(\kappa_x tx - \kappa_y ty)\right] \\ &+ \frac{1}{32}\cos\left[2\pi(\kappa_x tx + 2\kappa_y ty)\right] + \frac{1}{32}\cos\left[2\pi(\kappa_x tx - 2\kappa_y ty)\right] \\ &+ \frac{1}{32}\cos\left[2\pi(2\kappa_x tx + \kappa_y ty)\right] + \frac{1}{32}\cos\left[2\pi(2\kappa_x tx - \kappa_y ty)\right] \end{aligned}$$

$$+\frac{3}{64}\cos\left[2\pi(2\kappa_x tx)\right]+\frac{3}{64}\cos\left[2\pi(2\kappa_y ty)\right]$$
$$+\frac{1}{128}\cos\left[2\pi(2\kappa_x tx+2\kappa_y ty)\right]+\frac{1}{128}\cos\left[2\pi(2\kappa_x tx-2\kappa_y ty)\right]\Bigg\}$$

We can see here terms similar to those in the one-dimensional case, giving us again two SPIFI sidebands, now in x and y. These come from the first order sidebands in x and y only. We'll again ignore the second harmonic terms (those with dependence on $2\kappa_y$ and $2\kappa_x$), which can be removed in post processing through appropriate filtering of the Fourier transform for a cosine modulator, and don't arise from the binary modulators we commonly use. We can then write the fundamental intensity

$$I_{\text{obj, fund}}(x,y,t)=\left|g(x,y)u(x,y)w(t)\right|^2\left\{\frac{9}{64}+\frac{3}{16}\cos\left[2\pi\kappa_x tx\right]+\frac{3}{16}\cos\left[2\pi\kappa_y ty\right]\right.$$
$$\left.+\frac{1}{8}\cos\left[2\pi(\kappa_x tx+\kappa_y ty)\right]+\frac{1}{8}\cos\left[2\pi(\kappa_x tx-\kappa_y ty)\right]\right\} \tag{6.2}$$

We'll consider these terms independently. We again have a single DC term, as well as our x and y projections. The terms of interest here are the cross terms. Considering this term alone we, we proceed with an analysis similar to the single disk case, and start by writing the intensity due to this term. We'll again switch to centrosymmetric x coordinates by making the substitutions $x'=x-x_c$ and $y'=y-y_c$, writing

$$I_{\text{obj, cross}}(x,y,t)=\frac{1}{8}\left|g(x,y)u(x,y)w(t)\right|^2\left[\cos\left[2\pi(\kappa_x t(x'+x_c)+\kappa_y t(y'+y_c))\right]\right.$$
$$\left.+\cos\left[2\pi(\kappa_x t(x'+x_c)-\kappa_y t(y'+y_c))\right]\right]$$
$$=\frac{1}{16}\left|g(x,y)u(x,y)w(t)\right|^2\left[e^{-2\imath\pi(tx'\kappa_x+ty'\kappa_y)}e^{-2\imath\pi(tx_c\kappa_x+ty_c\kappa_y)}\right.$$
$$\left.+\,e^{-2\imath\pi(-tx'\kappa_x+ty'\kappa_y)}e^{-2\imath\pi(-tx_c\kappa_x+ty_c\kappa_y)}+\text{c.c.}\right] \tag{6.3}$$

Using again a single detector, we'll integrate now over both x and y and again make the assumptions that the detector is large enough to capture the whole field and has sufficient electronic bandwidth to allow us to assume the electronic frequency response is flat across the used bandwidth

$$\begin{aligned} I_{\text{obj, cross}}(t) = \frac{1}{16}w(t)^2 \Big(& e^{-2\imath\pi(tx_c\kappa_x + ty_c\kappa_y)} \iint \left|g(x,y)u(x,y)\right|^2 e^{-2\imath\pi(tx'\kappa_x + ty'\kappa_y)} \mathrm{d}x\,\mathrm{d}y \\ & + e^{-2\imath\pi(-tx_c\kappa_x + ty_c\kappa_y)} \iint \left|g(x,y)u(x,y)\right|^2 e^{-2\imath\pi(-tx'\kappa_x + ty'\kappa_y)} \mathrm{d}x\,\mathrm{d}y + \text{c.c.}\Big) \\ = \frac{1}{16}w(t)^2 \big[& \mathcal{G}\{\kappa_x t, \kappa_y t\} e^{-\imath 2\pi(tx_c\kappa_x + ty_c\kappa_y)} \\ & + \mathcal{G}\{-\kappa_x t, \kappa_y t\} e^{-\imath 2\pi(-tx_c\kappa_x + ty_c\kappa_y)} + \text{c.c.}\big] \end{aligned} \tag{6.4}$$

where c.c. indicated the complex conjugate of the previous terms,

$$\mathcal{G}(f_x, f_y) = \iint \left|u(x,y)g(x,y)\right|^2 e^{\imath 2\pi(f_x x + f_y y)} \mathrm{d}x\,\mathrm{d}y \equiv \mathfrak{F}\{|u(x,y)g(x,y)|^2\}$$

and $\mathfrak{F}$ is the spatial fourier transform. This is the temporal signal of the two dimensional modulator, given by the spatial Fourier transform of the square of the object transmission times the illumination spatial intensity. Fourier transforming this cross term into electronic frequency this temporal signal becomes

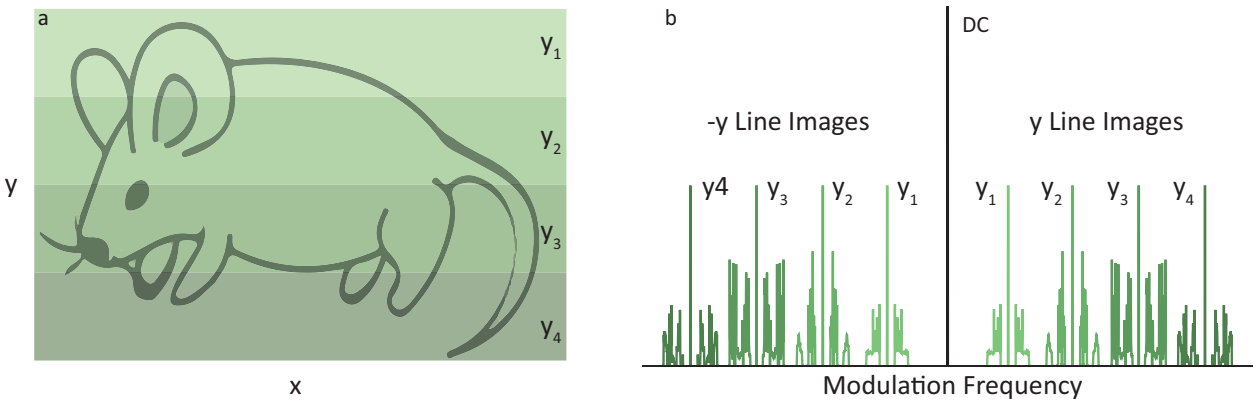

FIGURE 6.5. Cartoon showing SPIFI operation in 2D. The (a) colored regions indicate different slices of larger image being mapped into (b) the frequency domain of a photodiode signal, shown here with four x line images of the object encoded as sidebands of four discrete y frequencies.

$$
\begin{aligned}
I_{\text{obj, cross}}(f) = \frac{1}{16}\mathfrak{F}\{w(t)^2\} \otimes \Bigg[& \left| g\left(\frac{f}{\kappa_x}, \frac{f}{\kappa_y}\right) u\left(\frac{f}{\kappa_x}, \frac{f}{\kappa_y}\right) \right|^2 \\
& + \left| g\left(-\frac{f}{\kappa_x}, \frac{f}{\kappa_y}\right) u\left(-\frac{f}{\kappa_x}, \frac{f}{\kappa_y}\right) \right|^2 \\
& + \left| g\left(\frac{f}{\kappa_x}, -\frac{f}{\kappa_y}\right) u\left(\frac{f}{\kappa_x}, -\frac{f}{\kappa_y}\right) \right|^2 \\
& + \left| g\left(-\frac{f}{\kappa_x}, -\frac{f}{\kappa_y}\right) u\left(-\frac{f}{\kappa_x}, -\frac{f}{\kappa_y}\right) \right|^2 \Bigg]
\end{aligned}
\tag{6.5}
$$

This cross term allows us to recover the contrast function $g(x, y)$ from one of two x sidebands of one of two y carriers. Referring to the schematic depiction of the 2D data shown in Fig. 6.5, we can see the contribution of each of these terms. Each x line out show up four times, on either side of the both the positive and negative y carrier frequency.

Returning for a moment to fill in the remaining DC, x and y dependant terms, we consider first the x dependant term

$$
\begin{aligned}
I_{\text{obj, xSB}}(x, y, t) &= \frac{1}{8} \left| g(x, y) u(x, y) \right|^2 w(t)^2 \cos(2\pi t(x' + x_c)\kappa_x) \\
&= \frac{1}{16} \left| g(x, y) u(x, y) \right|^2 w(t)^2 \left(e^{-2\imath\pi t x' \kappa_x} e^{-2\imath\pi t x_c \kappa_x} + \text{c.c.} \right)
\end{aligned}
$$

again integrating over both spatial dimensions, we again have a spatial fourier transform along x, but what is now being transformed is the contrast function integrated along y,

$$I_{\text{obj, xSB}}(t) = \frac{1}{16} w(t)^2 e^{-2\imath\pi t x_c \kappa_x} \int e^{-2\imath\pi t x' \kappa_x} \int \left| g(x', y) u(x', y) \right|^2 \mathrm{d}y \, \mathrm{d}x' + c.c. \tag{6.6}$$

Giving a temporal signal again as a spatial fourier transform where we'll define lateral projections in x and y as $\mathcal{G}_x(f_x) = \int e^{-2\imath\pi t x \kappa_x} \bar{g}(x) \, \mathrm{d}x$ and $\mathcal{G}_y(f_y) = \int e^{-2\imath\pi t y \kappa_y} \bar{g}(y) \, \mathrm{d}y$ where the integrated x and y profiles are given by $\bar{g}(x) = \int \left| g(x,y) u(x,y) \right|^2 \mathrm{d}y$ and $\bar{g}(y) = \int \left| g(x,y) u(x,y) \right|^2 \mathrm{d}x$. Combining these terms with Eq. 6.5, we determine the total intensity spectrum

$$\begin{aligned} I_{\text{obj}}(f) = \frac{1}{16} \mathfrak{F}\{w(t)^2\} \otimes \Bigg[& \delta(f) + \bar{g}\left(\frac{f}{\kappa_x}\right) + \bar{g}\left(-\frac{f}{\kappa_x}\right) + \bar{g}\left(\frac{f}{\kappa_y}\right) + \bar{g}\left(-\frac{f}{\kappa_y}\right) \\ & + \left| g\left(\frac{f}{\kappa_x}, \frac{f}{\kappa_y}\right) u\left(\frac{f}{\kappa_x}, \frac{f}{\kappa_y}\right) \right|^2 + \left| g\left(-\frac{f}{\kappa_x}, \frac{f}{\kappa_y}\right) u\left(-\frac{f}{\kappa_x}, \frac{f}{\kappa_y}\right) \right|^2 \\ & + \left| g\left(\frac{f}{\kappa_x}, -\frac{f}{\kappa_y}\right) u\left(\frac{f}{\kappa_x}, -\frac{f}{\kappa_y}\right) \right|^2 + \left| g\left(-\frac{f}{\kappa_x}, -\frac{f}{\kappa_y}\right) u\left(-\frac{f}{\kappa_x}, -\frac{f}{\kappa_y}\right) \right|^2 \Bigg] \end{aligned} \tag{6.7}$$

where $\delta(f)$ is the Dirac delta function.

The many terms of this power spectrum are shown in Fig. 6.6, we now have terms that correspond to each region of the power spectrum, filling in the DC terms, as well as the integrated projections. To recover the contrast function, we will need to select a cross terms. In order to recover the signal from one of these cross term generated sidebands, which all contain the same information, we need to not only ensure we can separate those sidebands by filtering, but we must also ensure that these mixing sidebands are not corrupted by the presence of the x or y integral sidebands. This condition is met in the simulated data shown in Fig. 6.6, as all the cross terms are well separated, both from one another and from the

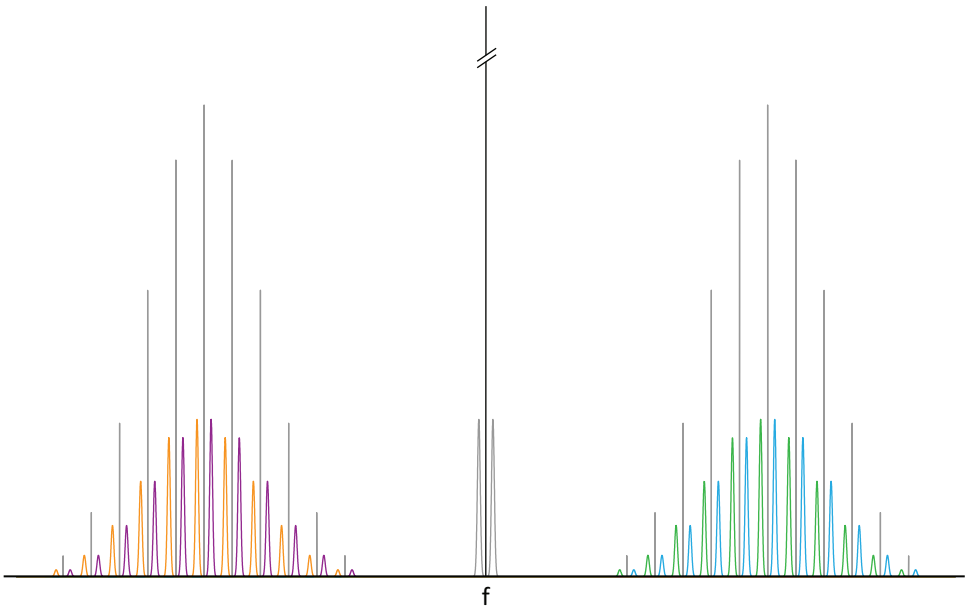

FIGURE 6.6. Plot of power spectrum as described by Eq. 6.7, using a Gaussian beam illumination profile and a uniform transmission function (no object). The "DC" peak is shown in black and the lateral x projection close to "DC" is shown in grey. The y projection profile is shown by discrete narrow frequency "spikes", whose width are given by the time window of the measurement. The four cross terms, which all contain the same information, are shown in different colors: $(-x, -y)$ in green, $(+x, -y)$ in purple, $(-x, +y)$ in orange, and $(+x, +y)$ in blue.

carrier "spikes". If the sidebands overlapped, we would be unable to select a single cross term by filtering, and the resulting image would be corrupted. To ensure this requirement is met in an experiment, we return to the analysis of resolution in SPIFI. This will allow us to ensure that the frequency separation in y is sufficient to ensure that the x sidebands don't overlap.

The resolution of SPIFI is given by the inverse of the highest spatial frequency on the mask, $\delta x = 1/\Delta k$. The frequency separation of the effective pixels is then just the spatial resolution times the chirp rate, $\delta f = \delta x \kappa = f_r$. Now we require that the spacing between the frequencies of the effective pixels of one disk be several times the frequency bandwidth of the other disk, such that we can ensure there is sufficient electronic bandwidth to contain a positive and negative SPIFI sideband for each of the effective pixels. In this analysis, we'll assume that the x modulator is spinning at the slower rate f_{rx}, giving the time window of the experiment T_w,

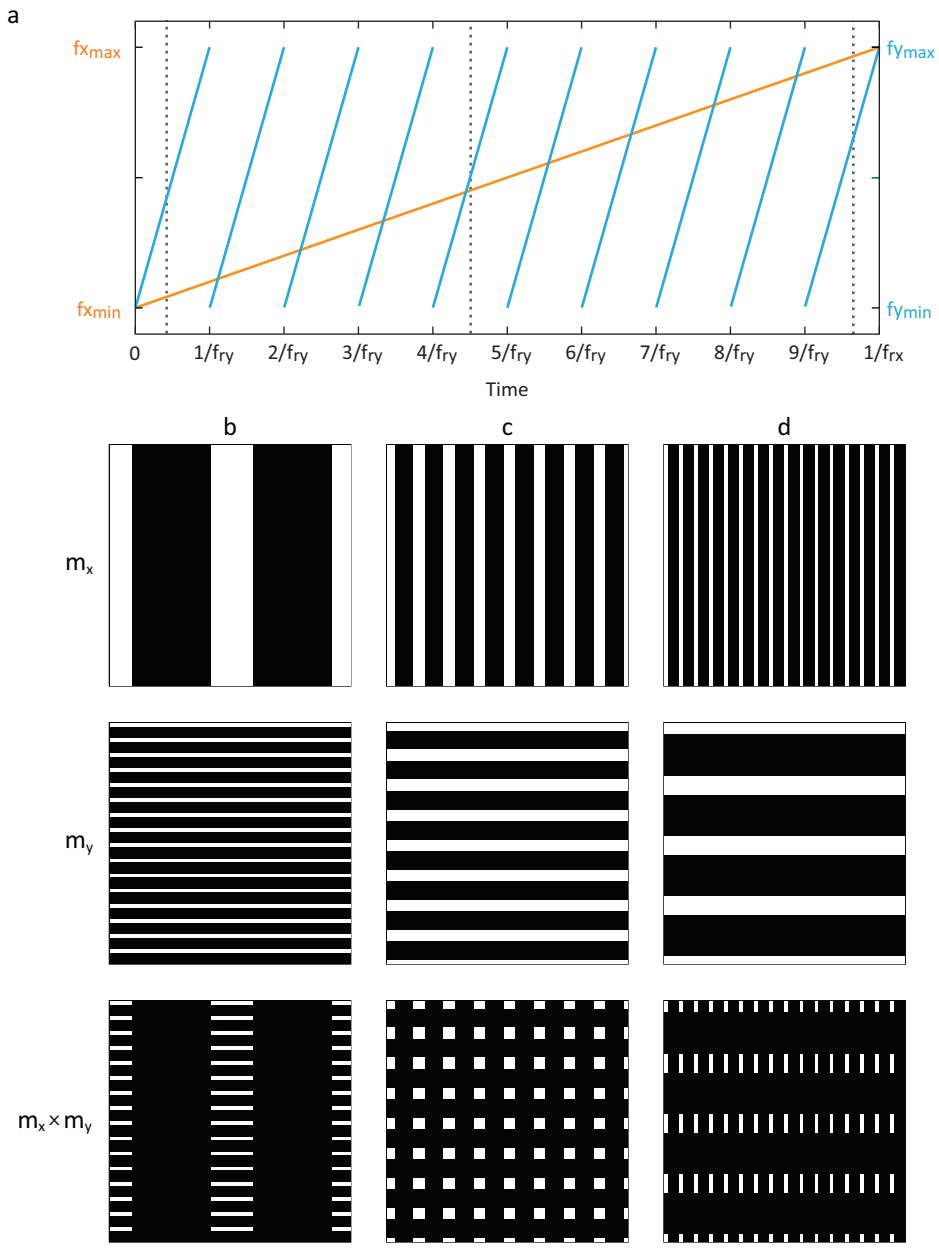

FIGURE 6.7. (a) Example of sweep of f_x and f_y, showing multiple sweeps of f_y over the time window of the x modulator. This figure is for $N_x = 5$. Spatial frequency distributions of the modulators m_x, m_y and $m_x \times m_y$, are shown for three times in (b), (c), and (d) corresponding to the dotted lines in (a).

and the y modulator will spin faster, at a rate of f_{ry} and have an electronic bandwidth of Δf_m as given in Eq. 5.12. At minimum, this requires that the frequency separation of the y pixels, δf_{ry}, be double the x bandwidth, $\Delta f_{mx} = f_{rx}\Delta k_x W_x$, which gives $\delta f_{ry} \geq 2\Delta f_{mx}$. This requires

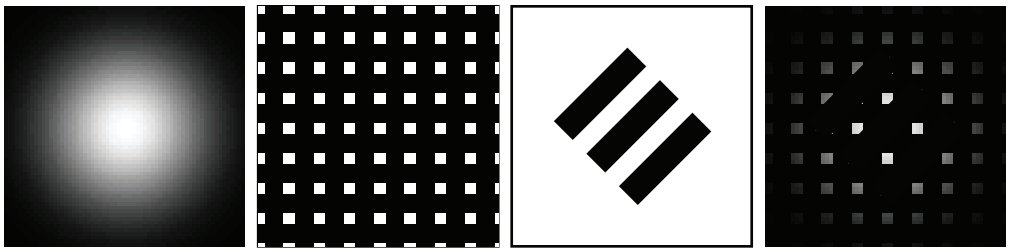

FIGURE 6.8. The Gaussian illumination beam is transmitted by the spatial frequency modulation, as seen in Fig. 6.7, then transmitted by a simple object yielding the distribution that is spatially integrated by the detector.

that the rotation rates of the two masks obey the relationship

$$\frac{f_{ry}}{f_{rx}} \geq 2N_x \tag{6.8}$$

where $N_x = \Delta k_x W_x$ is the number of points in x. This requires the y disk to spin a great deal faster than the x disk. In the time window of the slow disk, the spatial frequencies of the mask will be swept through once, while on that same time scale the spatial frequencies of the y disk will be swept through $2N_x$ times (at minimum), as displayed in Fig. 6.7. The time window of the x modulator also sets the width of the peaks from the y integrated projection, which must be narrower than the minimum frequency in x.

This requirement places some limitations on the dual disk system, namely, that the y disk would need to spin at a rate equal to double the number of x pixels. For an imaging system in which you would want to have hundreds of pixels in x, the y disk would have to be spinning a great deal faster than the x disk. There are two ways to relax this requirement. First, we can artificially limit the number of frequencies on the disk. The number of frequencies for the continuous case is $N_y = W_y \Delta k_y$. We can reduce the number of frequencies on the mask by constructing a modulator with a limited set of discrete frequencies, as detailed in Appendix E. If we create a mask that has a reduced number of frequencies N_y', the spatial resolution is

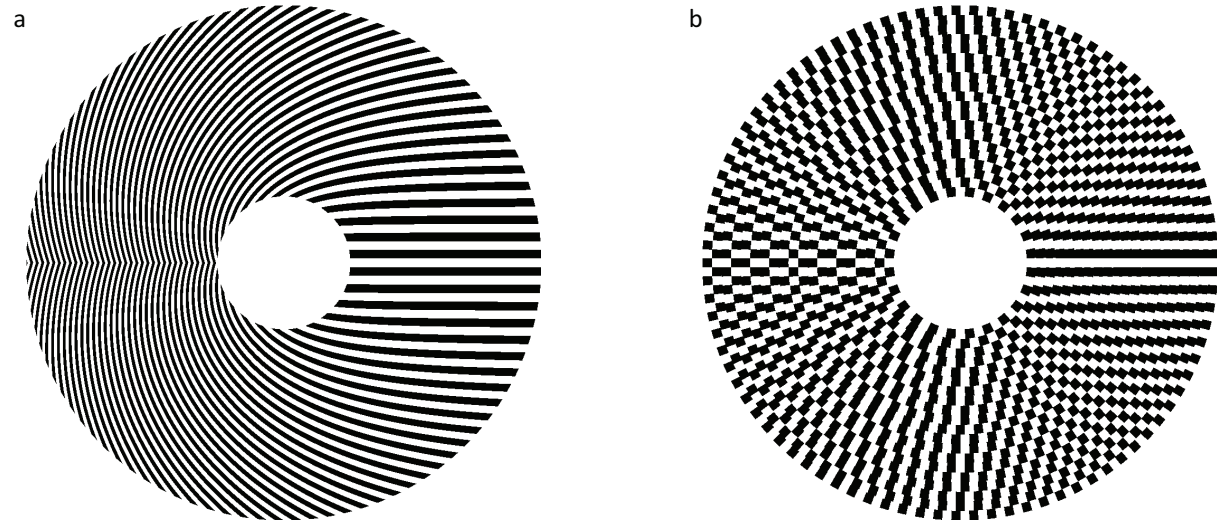

FIGURE 6.9. Comparison of a (a) continuous SPIFI mask with a linear chirp rate (b) a SPIFI mask with reduced number of frequencies. Both masks have a chirp rate of $\Delta k = 3/\text{mm}$ and the discrete mask uses 20 frequencies.

reduced to the width of the discrete frequency bins on the mask, $\delta f'_{ry} = \frac{N_y}{N'_y} f_{ry}$. Equating this to the x bandwidth as in Eq. 6.8, the required ratio is reduced by the factor $\frac{N'_y}{N_y}$ to

$$\frac{f_{ry}}{f_{rx}} \geq 2\frac{N'_y}{N_y} N_x. \tag{6.9}$$

Alternately, modifications can be made to the optical setup to allow the data to be processed from the time trace, rather than in electronic frequency as described above, which allows more flexibility in recovering the image.

Discrete Mask. In this section, we'll analyze the case of a discrete mask for the y modulator, that is, a mask with a limited set of discrete frequencies. To begin, we write the modulation as a continuous modulation function, $m_x(x,t)$, in x and the y modulation, $m_y(y,t)$, as the sum of N_m discrete masks.

$$m_x(x,t) = \frac{1}{2} + \frac{1}{2}\cos\left[2\pi\left(f_{ox} + \kappa x\right)t\right]$$

$$m_y(y,t) = \sum_{n=-\frac{1}{2}N_y}^{\frac{1}{2}N_y} \text{rect}\left(\frac{y-n\Delta}{\Delta}\right)\left\{\frac{1}{2}+\frac{1}{2}\cos\left[2\pi(f_{oy}+n\Delta f)t\right]\right\}$$

where we use the parameters Δ as the y pixel width, Δf is the difference in carrier modulation frequency between adjacent y pixels, f_{ox} is the x offset frequency, f_{oy} is the y offset frequency and $f_{ny} = f_{oy} + n\Delta$f. A depiction of such a mask is shown in Fig. 6.9, where we compare the continuous (limited by print resolution) and discrete masks. We'll expand the modulation function to write and then group into diffracted orders for the Fourier plane

$$m(x,y,t) = \frac{1}{4} + \frac{1}{4}\sum_{n=-\frac{1}{2}N_y}^{\frac{1}{2}N_y} \text{rect}\left(\frac{y-n\Delta}{\Delta}\right)\cos\left(2\pi f_{ny}t\right) + \frac{1}{4}\cos\left[2\pi\left(f_{ox}+\kappa x\right)t\right]$$
$$+ \frac{1}{4}\cos\left[2\pi\left(f_{ox}+\kappa x\right)t\right]\sum_{n=-\frac{1}{2}N_y}^{\frac{1}{2}N_y} \text{rect}\left(\frac{y-n\Delta}{\Delta}\right)\cos\left(2\pi f_{ny}t\right).$$

Expand the x cosine term to simplify the 2D spatial Fourier transform

$$m(x,y,t) = \frac{1}{4} + \frac{1}{4}\sum_{n=-\frac{1}{2}N_y}^{\frac{1}{2}N_y} \text{rect}\left(\frac{y-n\Delta}{\Delta}\right)\cos\left(2\pi f_{ny}t\right) + \frac{1}{8}e^{\imath 2\pi(f_{ox}+\kappa x)t} + \frac{1}{8}e^{-\imath 2\pi(f_{ox}+\kappa x)t}$$
$$+ \frac{1}{8}e^{\imath 2\pi(f_{ox}+\kappa x)t}\sum_{n=-\frac{1}{8}N_y}^{\frac{1}{2}N_y} \text{rect}\left(\frac{y-n\Delta}{\Delta}\right)\cos\left(2\pi f_{ny}t\right)$$
$$+ \frac{1}{8}e^{-\imath 2\pi(f_{ox}+\kappa x)t}\sum_{n=-\frac{1}{2}N_y}^{\frac{1}{2}N_y} \text{rect}\left(\frac{y-n\Delta}{\Delta}\right)\cos\left(2\pi f_{ny}t\right)$$

writing the modulator in terms of spatial frequencies as a sum of the different terms, $M\left(f_x, f_y, t\right) = M_{\text{dc}} + M_{\pm\text{carrier}} + M_{\pm\text{SPIFI}} + M_{\pm\text{SPIFI}\pm y}$, where we've defined

$$M_{\text{dc}} = \delta\left(f_x\right)\delta\left(f_y\right)$$

$$M_{\pm\text{carrier}} = e^{\pm\iota 2\pi f_{oy} t} \frac{\sin\left[\pi\left(\Delta f_y \pm \Delta f t\right)\left(1+N_y\right)\right]}{\sin\left[\pi\left(\Delta f_y \pm \Delta f t\right)\right]} \frac{\sin\left(\pi \Delta f_y\right)}{2\pi \Delta f_y}$$

$$M_{\pm\text{SPIFI}} = \frac{1}{2} e^{\pm\iota 2\pi f_{ox} t} \delta\left(f_y\right) \delta\left(f_x \pm \kappa t\right)$$

$$M_{\pm\text{SPIFI}+y} = \frac{1}{4} e^{\iota 2\pi\left(f_{ox} \pm f_{oy}\right) t} \delta\left(f_x \pm \kappa t\right) \frac{\sin\left[\pi\left(\Delta f_y + \Delta f t\right)\left(1+N_y\right)\right]}{\sin\left[\pi\left(\Delta f_y + \Delta f t\right)\right]} \frac{\sin\left(\pi \Delta f_y\right)}{2\pi \Delta f_y}$$

$$M_{\pm\text{SPIFI}-y} = \frac{1}{4} e^{-\iota 2\pi\left(f_{ox} \mp f_{oy}\right) t} \delta\left(f_x \pm \kappa t\right) \frac{\sin\left[\pi\left(\Delta f_y - \Delta f t\right)\left(1+N_y\right)\right]}{\sin\left[\pi\left(\Delta f_y - \Delta f t\right)\right]} \frac{\sin\left(\pi \Delta f_y\right)}{2\pi \Delta f_y}$$

This modulation is convolved with the product of the spatial beam profile and the contrast function, and the intensity is calculated. The resolution in this case is limited in y by the width of the frequency bins, with the y object information being integrated across the widened modulation bands. This analysis proceeds as in the continuous analysis, leading back to the spin rate ratio we saw in Eq. 6.8. However, we can now create masks with an arbitrary number of points, allowing us to balance our required number of y pixels with our desired frame rate. This does require that a mask be created with the specified number of points, and the ratio of spin rates of the masks will be set by the design of the two masks used in the system.

While this allows more flexibility in the design of the system, we are still in the position of requiring the mask parameters and motor parameters to be chosen at design time. It would be desirable for the system to have more flexibility, to be able to chose the desired motor spin rate at the time of the actual measurement, and simply have whatever y resolution is supported by the chosen configuration.

Image Reconstruction. With the appropriate spin rates chosen for the resolution as per Eq. 6.8, the time window of the experiment is set. The intensity can then be measured as a function of time over a single rotation of the "slow" modulator, giving a signal that takes the form given in Eq. 6.7. As the object spatial information is contained within the power

spectrum of this photodetector signal, we first calculate the power spectrum. This can be trivially done using a Fast Fourier Transform (FFT), or by using a more advanced power spectral density estimator, such as multitaper [53].

The power spectrum looks akin to Fig. 6.6, with a narrow "spike" corresponding to each y position and a positive and negative sideband on either side of that y frequency containing the corresponding x data. As there are two sidebands for each y location as well as two overall sidebands, there are four copies of the image data contained within this power spectrum. We can reconstruct the four degenerate two-dimensional images by reshaping the power spectral data from temporal frequency into space, mapping temporal frequency into space using the factors κ_x and κ_y.

To construct an image, we reshape the power spectrum by starting with the lowest frequency y value, then collecting a set of data points that corresponds to the x sideband and placing it as the first row of a pixel array. The second row is then calculated by shifting the frequency spectrum by the frequency difference between the two adjacent y carriers, given by $\kappa_y \delta_y$, and taking the next x sideband. This process can be repeated until all the x sidebands have been extracted and the image is complete. The process is then repeated for each of the remaining three images.

Direct Fourier Synthesis Reconstruction. In this section, we will consider the signal in terms of time, rather than the frequency domain version as in previous sections. In our analysis of 1D SPIFI, we cast the time trace first as the sum of a set of sinusoids, each weighted by the object contrast function at the position corresponding to that location. Fourier transforming this temporal trace gives the electronic spectrum, which contains the object contrast function.

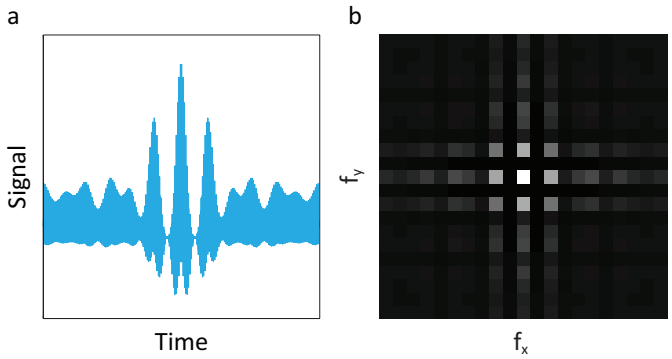

FIGURE 6.10. (a) Simulated temporal SPIFI signal generated for a square aperture and (b) the same trace interpolated onto spatial frequency axes.

We have equivalently considered the mask not as a radially dependant cosine, but rather as a swept grating, whose spatial frequency is swept as a function of time over the scan window $T_{x,y} = 1/f_{r(x,y)}$. Each point in the time trace is then a measure of the projection of a single spatial frequency grating on to the object contrast function. The time trace is thus the spatial frequency spectrum, and Fourier transforming this spatial frequency data gives the object spatial information. Expanding this to the two dimensional case we consider the product of two orthogonal time variant gratings, each of whose spatial frequencies is traced out over time, as depicted in Fig. 6.7. The temporal trace, as shown in Fig. 6.10(a) is reshaped into a 2D array, as shown in Fig. 6.10(b), which can be inverse 2D Fourier transformed to recover the object information.

Cast in this light, it is easy to see why one disk must rotate many times in the rotation time of the other; to measure an accurate spatial frequency spectrum of the object, the overlap integral must be measured between the object and all spatial frequencies in both x and y. To accomplish this, the grating of the slow disk must not change over the rotation time of the faster disk, leading to the spin rate requirement set by Eq. 6.8.

Under this constraint, we process SPIFI trace as a list of x and y spatial frequency projections, which along with the spatial frequencies as a function of time, can be converted to

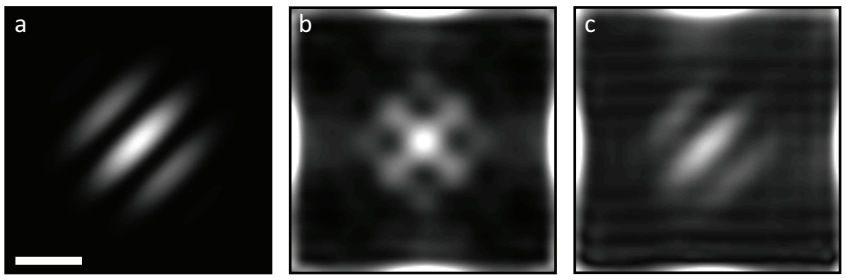

FIGURE 6.11. Simulated image recovery by direct Fourier synthesis. A simple object (a) illuminated by a Gaussian beam and the reconstructions from (b) the full intensity as given by Eq. 6.2 and (c) the single sideband intensity, from Eq. 6.3.

the object contrast function by 2D Fourier transform. To demonstrate this method, SPIFI traces are simulated and reconstructed using this method and the resulting images shown in Fig. 6.11. A simple test object, a series of diagonal lines, is illuminated with a Gaussian beam, giving a contrast function as shown in Figure 6.11(a). The temporal SPIFI intensity trace is calculated from Eq. 6.2 for a set of spatial frequencies f_x and f_y. The temporal SPIFI trace is then reshaped from time vector into a two-dimensional array in terms of the two spatial frequencies, f_x and f_y. This 2D array is then inverse Fourier transformed using an inverse two-dimensional fast Fourier transform (ifft2) algorithm to yield the object transmission function, shown in Fig. 6.11(b). As the intensity trace contains four degenerate copies of the image, two normal images and two conjugate images, the reconstruction based on the full intensity trace yields a corrupted image, namely the sum of all four images. To get a single image, the process must be performed on an intensity trace that contains only a single sideband, as given by Eq. 6.3, which yields a recovered image as shown in Fig. 6.11(c).In this simulation, the spin rates of the disks were made to exceed the requirement given in Eq. 6.8, and thus a single sideband could be selected by Fourier filtering. The image recovered for the single sideband is in good agreement with the test object. The image recovered from the full SPIFI trace is clearly corrupted by the presence of other sidebands.

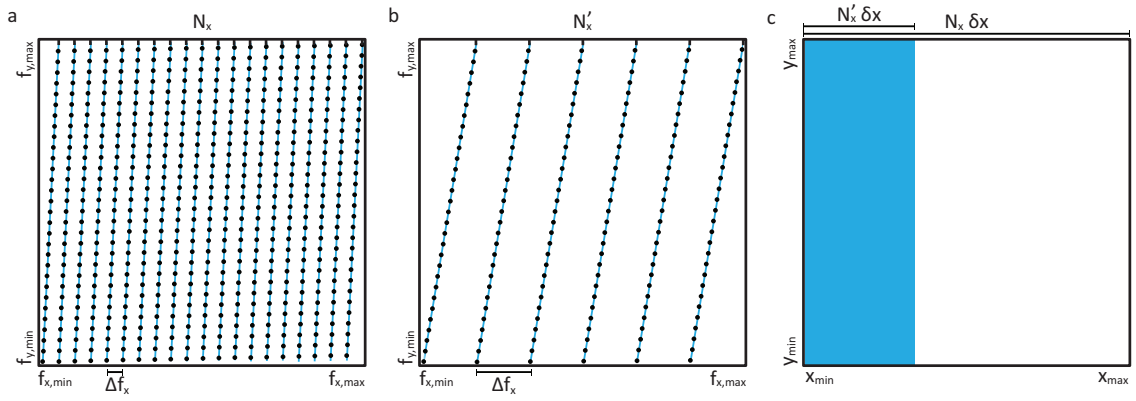

FIGURE 6.12. Spatial frequency sweeps (blue lines) at each time sample (black dots) for (a) a high spin rate and (b) a low spin rate. The effective f_x sampling is marked in the figure as Δf_x.

Spatial Aliasing. In the previous description, we've assume that the rotation rates met the requirement given in Eq. 6.8. In that case, the x modulator grating doesn't change over the timescale of the y modulator. If the ratio of the spin rates is lower, then there is some change in x spatial frequency over the rotation time of the y disk. The y grating sweep then happens over a narrow sweep in x, leading to a greater tilt in spatial frequency and an increase in f_x sample separation, as shown in Fig. 6.12. In the limiting case of Eq. 6.8 we have a number of x points given by $N_x = f_{ry}/f_{rx}$. As the maximum spatial frequency on the mask, $f_{\text{x,max}}$, is fixed by the mask design we can write the spatial frequency sampling, Δf_x as

$$\Delta f_x = \frac{f_{\text{x,max}}}{N_x}. \tag{6.10}$$

As the spatial frequency sampling is related to the spatial resolution, dx through

$$\Delta f_x = \frac{1}{N_x dx} = \frac{1}{W_x}, \tag{6.11}$$

an increase in spatial frequency separation leads to a corresponding decrease in the spatial window, W_x. This reduces the field of view possible at the reduced spin rate. This is consistent

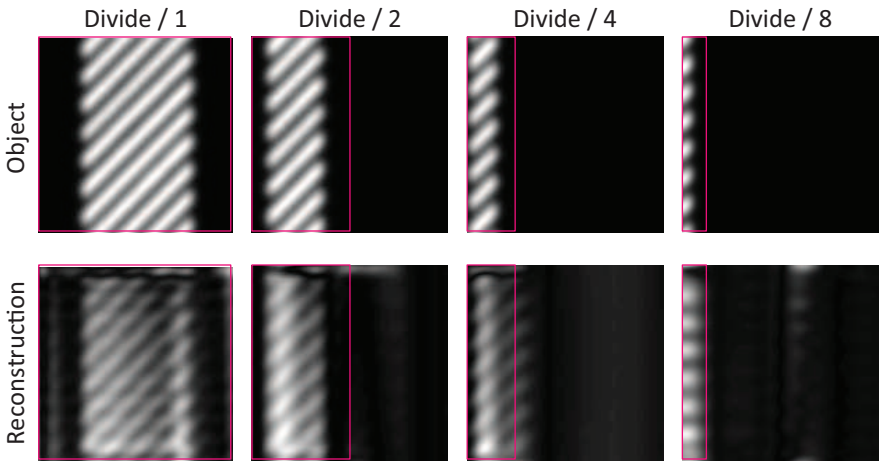

FIGURE 6.13. Reconstructed 2D SPIFI image of a set of diagonal lines as a function of lowering spin rates. The total width of each panel is the same, with the object width being reduced by the reduction in spin ratio and indicated by the red square.

with Eq. 6.8, where instead of determining the required spin rate from the number of points, we instead look at the number of points possible for a desired spin rate ratio,

$$N_x \leq \frac{f_{ry}}{f_{rx}}. \tag{6.12}$$

The factor of two has been eliminated here by using a single SPIFI sideband. In this case the required filtering would need to be accomplished optically, before the trace is measured. To accomplish this, we'll use the same sideband selection technique that plays an important role in Coherent Holographic Imaging by Recovered Phase from Emission Distributions (CHIRPED) (Chapter 7), namely filtering the sideband in the dimension orthogonal to the dimension of modulation.

The reduction in field of view is shown again using a simulation in Fig. 6.13. The simulated experiment is set up with a 4 mm field of view, and a trace simulated and reconstructed using a single sideband and the spin rate as required by Eq. 6.8. The spin rate is then reduced, and the used field of view is also reduced, allowing more flexibility in experimental design.

Results. The setup for this experiment, shown schematically in Fig. 6, begins with a 405 nm laser diode (Q Photonics QLD-405-100S) in a temperature-controlled diode mount (Thorlabs LDM9T). The diode output is collected using a 4 mm focal length lens and spatially filtered using a 20x objective and a 10 μm pinhole. The beam is then expanded to its final size, an approximate diameter of 20 mm. This large beam is then brought to a horizontal line focus using a 50 mm focal length cylindrical lens and then modulated by the spinning cosine modulator (Inlight GOBOs) with a chirp rate of $\Delta k = 5/\text{mm}$. The modulator disk is mounted on a custom designed and machined mounting chuck to the shaft of a brushless DC motor (Faulhaber 2057). The motor is held at a constant angular velocity using a speed controller (Faulhaber MCBL3006) reading hall sensors packaged within the motor. These hall sensors also provide a synchronization signal useful in timing the data acquisition. The beam proceeds from this modulator to a 50 mm spherical lens, which collimates the beam in the vertical dimension and simultaneously focused it to a vertical line at the plane of the second modulator. The second modulator has a chirp rate of 7/mm and is mounted similarly to the first motor. The second modulator, like the first, is printed in aluminum on soda-lime glass and has an outer diameter of 62 mm and an inner diameter of 15 mm, used for mounting. Finally, the second mask plane is imaged in to the object plane, using a 50 mm spherical plano-convex lens and a 50 mm plano-convex cylindrical lens placed back to back, creating an ersatz optic with a sagittal (x–z) focal length of 50 mm and a tangential (y–z) focal length of 25 mm. This creates an image of the x modulator and the y modulator both in the object plane. The beam is then transmitted by an object in this plane, the collected using a 25 mm condenser lens on to a single element photodiode (Thorlabs DET-100A). The photodiode signal is amplified using a current preamplifier (Stanford Research Systems SR570) before

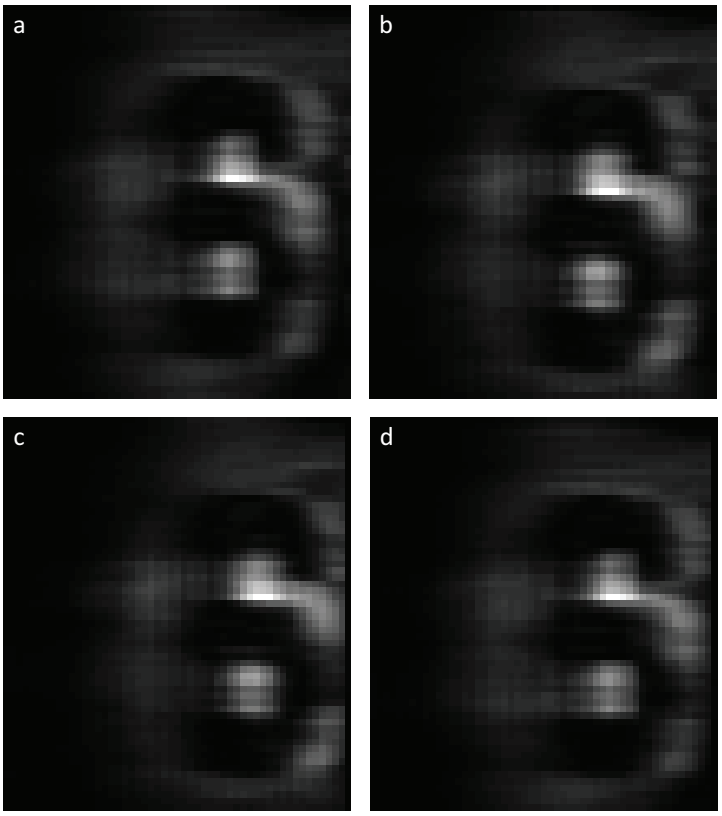

FIGURE 6.14. Two dimensional SPIFI image of the number ”6” printed on a transmissive mask. The object here is absorptive, so we see the illumination beam profile with the absorptive number 6 in the middle. The four images are constructed using the four cross terms, showing each sideband contains the same information.

being digitized (National Instruments PCI-6110). The aforementioned sync signal is used to trigger the start of data acquisition using custom software, which collects the traces and displays their Fourier transform for rapid analysis. The program saves the digitized traces for offline analysis using MATLAB.

The “slow” x modulator was spun at a rate of 0.5 Hz while the “fast” y modulator was spun at a rate of 100 Hz and a SPIFI trace taken over the time duration of several “slow” motor revolutions, to ensure ample data for offline processing. The data is then processed by first selecting a time trace out of the collected data corresponding to a single rotation of the “slow” disk. The Fourier transform of this data produces an electronic spectrum that looks,

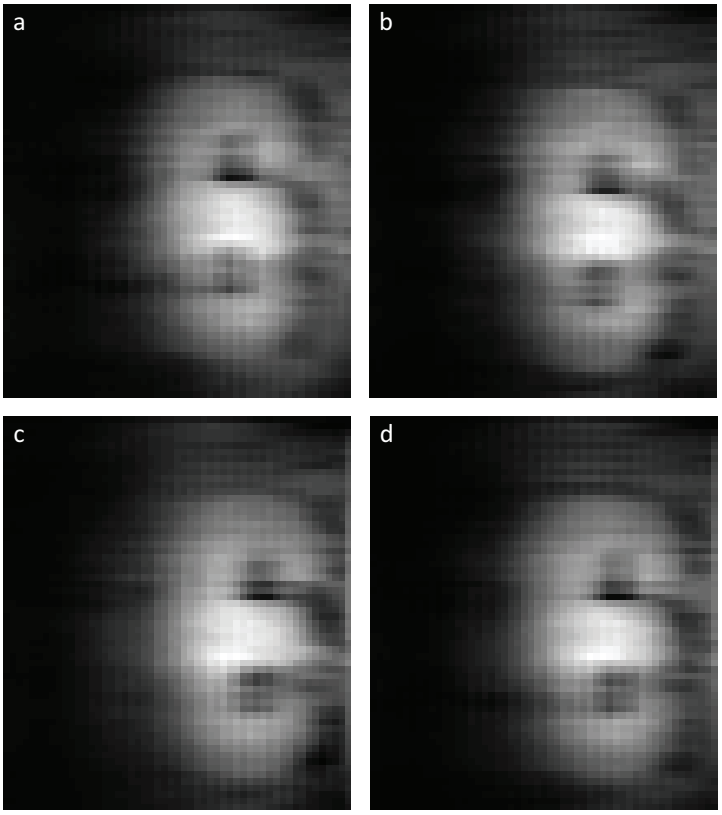

FIGURE 6.15. Two dimensional SPIFI image of the number ”6” printed on a transmissive mask and imaged using the dual disk SPIFI setup. Images were taken with and without the object in place, then subtracted to remove the illumination beam profile. Note that the image has been inverted for clarity. The four images are constructed using the four cross terms, as in Fig. 6.14.

schematically, like that in Fig. 6.6, with the four cross terms, as well as DC terms and the integrated projection terms. The desired cross term (any of the four will do) is isolated by reading out sections of the Fourier transform array into a new matrix, each row of which is one of the x sidebands. When this matrix is complete, the rows will contain the x information at each y location, and the image will be completed. This process can easily be done for each of the four cross terms, yielding four images, like those shown in Fig. 6.14. This image was taken with a simple absorptive object, and shows an image of the beam profile blocked by the number “6” printed on a glass slide. This image is not just the object contrast function, but the product of the object contrast function and the spatial intensity profile of the beam. To

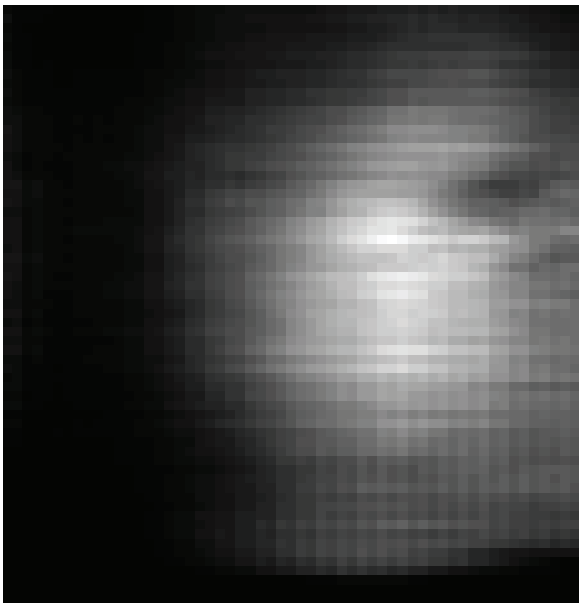

FIGURE 6.16. Two dimensional SPIFI image taken without an object, showing only the recovered beam profile.

recover only the contrast function, we make the same measurement without an object, yield an image of only the intensity profile as shown in Fig. 6.16, which can then be subtracted off the original image to yield only the contrast function, as shown in Fig. 6.15.

Discussion. In the previous analysis, we've assumed that we can adequately separate in electronic frequency the positive and negative SPIFI sidebands from the carrier y pixel frequency. We have further assumed that the second harmonic of the x sidebands do not overlap with the fundamentals. However, we have operated in this data in the limiting case, where the fundamental x sideband separation is half the y pixel separation. In this case, the second harmonic of each positive SPIFI sideband will overlap with the fundamental negative sideband of the next y pixel. This could be easily eliminated by increasing the rotation rate of the fast disk or decreasing the spin rate of the slow disk, increasing the y separation or decreasing the x sideband offset, respectively.

The other issue that may arise in extension of this technique is stability or the modulator spin rate. We have looked at the impact of motor instabilities and errors in modulation mask mounting previously [39], for the case of a single modulator. Any error in mounting or drift in motor speed will cause a variation in the frequency seen by each point on the beam as the disk rotates. When the power spectrum is estimated, this will cause broadening in the spectral features, which leads to blurring in the recovered image.

To ensure the frequency bins remain separate in the case of the dual disk system, the broadening of the frequencies due to instability in the fast disk has to be small compared to the frequency separation of features in the slow masks. As the dual disk approach requires two spinning disks at very different rates, this may require very high stability in the fast disk. This effect was minimized in the data presented by using moderate resolution SPIFI modulators. This error could also be easily minimized by using a non inertial modulator, such as an Acousto-Optic Deflector (AOD) or DMD.

6.3. DMD

Thus far we have examined three approaches to two-dimensional modulation based on the spinning disk modulator. As has been show, the main limitation of the spinning disk approach for two dimensional modulation is the requirement that one disk spins much faster than the other, limiting the update rates that are achievable. In order to alleviate these issues, we look to a modulator that does not depend on a rotating disk.

Using a 2D dimensional high-speed modulated optic, such as a DMD or an AOD. The DMD is an array of small aluminum mirrors which are able to switch rapidly between two small angular deviations. These mirrors are individually controllable, allowing the formation of binary images. Such arrays are commonly used in digital movie projectors, and are finding

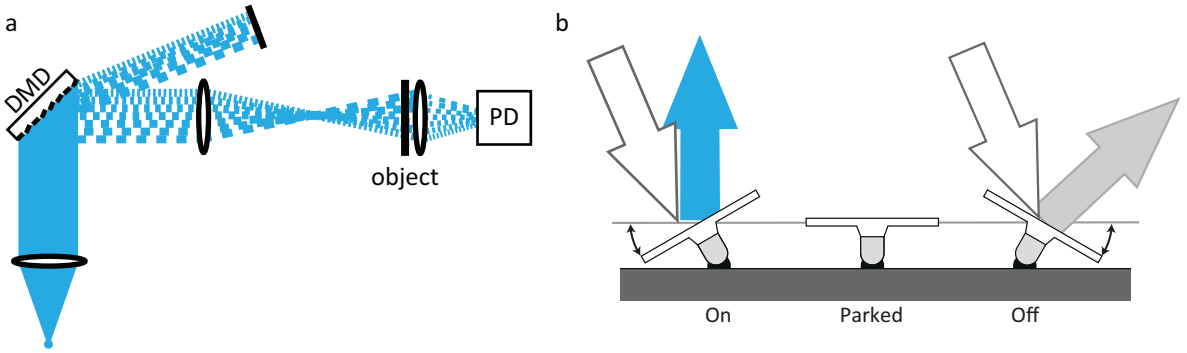

FIGURE 6.17. (a) Schematic of the DMD setup and (b) the DMD operation.

application in microscopy systems, such as confocal [54] and programmable array microscopes [55], as well as for structured illumination microscopy [56].

AOD sweep the beam path through an angular range proportional to the frequency of the acoustic wave present. The different acoustic wave periods manifest as a time dependent grating. 2D AOD systems exist, consisting of a pair of orthogonal one-dimensional AOD. The crossed gratings of different periods can be analyzed in the same way as the dual disk case, however the frequencies can be directly controlled, allowing the use of very high frequencies and sources with very good frequency stability. Such systems are not subject to the environmental perturbations of a mechanical modulator system. Such deflectors have been used in previous microscopy systems, for example for rapid raster [57] and random-access scanning [58].

We implement our 2D modulator using a DMD in an experimental setup shown in Fig. 6.17(a). The DMD is illuminated and the light reflected collected when the mirrors are in the "on" state with a lens that images the DMD to the object plane. The light transmitted by the object is collected with a condenser lens onto a single element detector. As each mirror of the DMD is modulated at a unique frequency that corresponds to its location, the temporal signal from the DMD is a sum of square waves each weighted by the object transmission function

at that location. The object transmission function can then be recovered from the electronic spectrum of the photodetector signal.

Theory. The DMD modulator divides the modulation plane into an array of pixels, with N_x pixels of width w_x in the x direction and N_y pixels of height w_y in the y dimension. The pixel function, given by

$$p(x, y; n_x, n_y) = \text{rect}\left(\frac{x - n_x w_x}{w_x}\right)\text{rect}\left(\frac{y}{w_y}\right)$$

will multiplied by the object contrast function, $g(x, y)$, and the two dimensional beam profile, $u(x, y)$ and spatially integrated on the single element detector. This then gives the weighting function of the discrete frequencies in terms of pixel number as

$$G(n_x, n_y) = \iint_{-\infty}^{\infty} g(x, y)u(x, y)p(x, y; n_x, n_y)\,\mathrm{d}x\,\mathrm{d}y \tag{6.13}$$

Using a two dimensional modulation function that can directly modulate any spatial location at any frequency (subject to limitations of the 2D modulator itself), we have a modulation function that is not necessarily separable in x and y, allowing flexibility in the modulation design. For simplicity, we choose a modulation that is a linear frequency ramp wrapped into N_x columns and N_y rows as shown in Fig. 6.18. This modulation function is given by

$$M(n_x, n_y, t) = \frac{1}{2} + \frac{1}{2}\cos\left\{2\pi\left[(n_y N_x + n_x)\kappa_p + \kappa_0\right]t\right\} \tag{6.14}$$

where n_x and n_y are the pixel indices, κ_0 is the frequency offset, and κ_p is the frequency slope in Hz/pixel, analogous to κ in Hz/mm as defined for the spinning disk modulator. If the pixels are being grouped into super-pixels, the pixel width can simply be replaced by the effective

pixel width $w_x' = w_x N_x'/N_x$, where N_x' is the number of superpixels. The y indices can be determined in the same way. The temporal signal from the photo detector is then given as the superposition of the frequencies from each pixel on the mask, Eq. 6.14, weighted by the object transmission function and beam profile on each pixel, given by Eq. 6.13. Summing the contributions from each pixel yields the total electric field

$$\begin{aligned} E(t) &= \sum_{n_x=0}^{N_x} \sum_{n_y=0}^{N_y} E_0 G(n_x, n_y) M(n_x, n_y, t) \\ &= \frac{E_0}{2} \sum_{n_x=0}^{N_x} \sum_{n_y=0}^{N_y} G(n_x, n_y) + \frac{E_0}{2} \sum_{n_x=0}^{N_x} \sum_{n_y=0}^{N_y} G(n_x, n_y) \cos\left\{2\pi \left[(n_y N_x + n_x)\kappa_p + \kappa_0\right] t\right\} \end{aligned}$$

where E_0 is the electric field amplitude. We'll again consider only the fundamental, and neglect the second harmonic. We'll also define the "DC" component as $I_0 = \left(\frac{E_0}{2} \sum_{n_x=0}^{N_x} \sum_{n_y=0}^{N_y} G(n_x, n_y)\right)^2$, allowing us to write

$$I(t) \propto I_0 + \sqrt{I_0} E_0 \sum_{n_x=0}^{N_x} \sum_{n_y=0}^{N_y} G(n_x, n_y) \cos\left\{2\pi \left[(n_y N_x + n_x)\kappa_p + \kappa_0\right] t\right\}. \tag{6.15}$$

Taking the Fourier transform of this temporal signal gives an electronic frequency spectrum given by

$$I(f) \propto \sum_{n_x=0}^{N_x} \sum_{n_y=0}^{N_y} G(n_x, n_y) \delta\left\{f - \left[(n_y N_x + n_x)\kappa_p + \kappa_0\right]\right\} \tag{6.16}$$

which allows the recovery of the object contrast function $g(x, y)$ from Eq. 6.13.

The number of unique frequencies on the mask then is simply the total number of pixels, assuming we are operating in the regime where the resolution is limited by pixel count. In order to reach this limit, the modulation bandwidth of the DMD must support a number

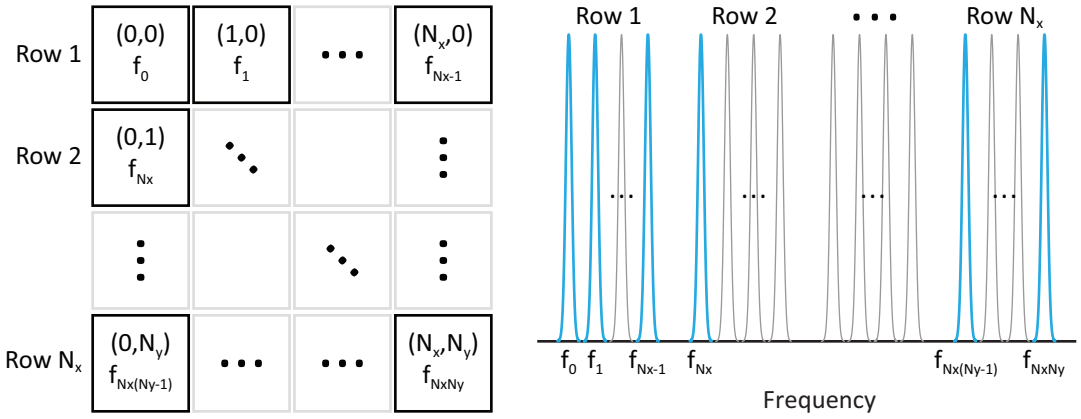

FIGURE 6.18. Diagram of the fundamental frequency distribution across the DMD, left, and the corresponding frequency spectrum, right. While the modulator produces binary modulations, and thus will produce harmonics in the electronic spectrum, only the fundamental frequency is shown. We are assuming here that the harmonics caused by the binary modulation do not overlap any of the fundamental frequencies.

of frequencies equal to the spatial resolution of the modulator. The frame rate, f_{DMD}, of the modulator supports a maximum frequency of $f_{max} = f_{DMD}/2$ per the Nyquist-Shannon sampling theorem [59, 60]. The frequency step that will be resolvable is limited by the time window of the modulator, as in the SPIFI case, to $\delta f = 1/t_r$. Assuming that we want the number of pixels in the x and y direction to be the same, we can then write the total number of supported pixels, N_{px}, as a function of these frequency parameters as

$$N_{\mathrm{px}} = \frac{f_{max}}{\delta f} \tag{6.17}$$

assuming that the entire electronic spectrum of the modulator is usable. The limiting factor for our implementation is the binary nature of our modulator. In order to support high-speed modulation, many available 2D modulators operate in a binary mode, which means that our sinusoidal modulations will appear as square waves and not true sinusoids. This will lead to harmonic content of low-frequency pixels corrupting higher frequency pixels if the

TABLE 6.1. Update rate and super-pixel resolution as a function of the number of pixels from the modulator used in this work. The resolution stated is for super-pixels distributed across the modulator, though this theory could be applied to a small subset of the modulator at full device resolution. The dashed line indicates resolutions not available on our device due to memory limitations.

Number of Pixels	Effective Resolution	Update Rate
32x32	437.8 μm	146 ms
64x64	218.9 μm	585 ms
120x120	116.7 μm	2 s
256x256	54.72 μm	9.1 s
512x512	27.36 μm	37 s
1024x768	13.68 μm	112 s

frequencies are chosen to span more than an octave. To suppress this effect, we'll choose the highest octave range present in the modulators bandwidth, namely $(f_{max}/2, f_{max}]$. The number of supported pixels is then reduced by 2 from Eq. 6.17. Assuming we want the number of pixels in the x and y dimensions to be the same, we write

$$Nx = Ny = \sqrt{\frac{f_{max}}{2\delta \mathrm{f}}} \tag{6.18}$$

While the time window of the modulator is not necessarily limited by the DMD, it is likely limited practically either by the memory of the device or the desired update rate of the experimental configuration.

Results. We implement this setup using a Texas Instruments DMD with a resolution of 1024 x 768 (Extended Graphics Array (XGA)). The frame rate of this device is 22,727 Hz and our evaluation board has 4 GB of memory allowing for storage of 43,690 images. The square aluminum mirrors are 13.68 μm on a side and tilt by $\pm 12°$ in response to the drive voltage. The array measures 20.736 mm x 11.664 mm. Following Eq. 6.18, we can use a maximum of Nx = Ny = 120 pixels (14400 total pixels). To accomplish this, we simply bin together groups of pixels on the DMD to act to move together as superpixels allowing use to confirm the

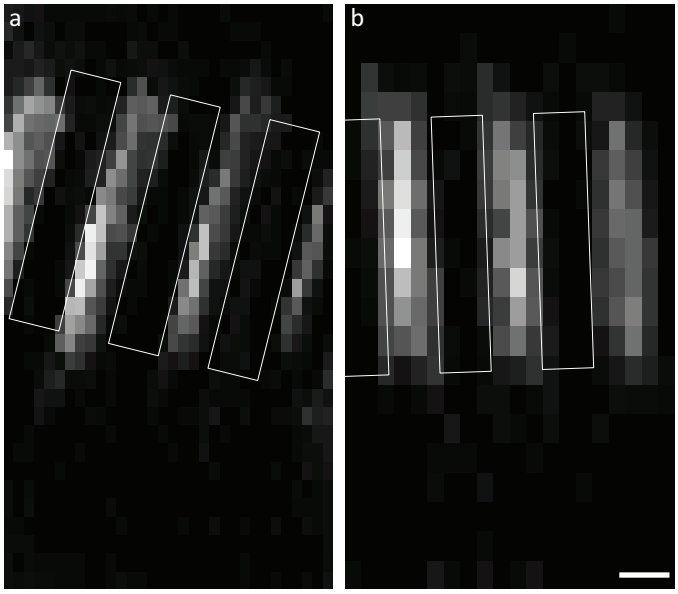

FIGURE 6.19. Images of a USAF test pattern taken using the DMD device and a single-element photodetector, for both (a) a 32×32 pixel grid and (b) a 20×20 pixel grid. The scale bar is 1 mm.

operation of this imaging technique using large superpixels. We could equivalently restrict the illuminated region of the DMD to a 120 square pixel area and use the pixels individually. The update rate for a variety of superpixel grids is given for this DMD in Table 6.1.

We illuminated the DMD using the same 405-nm CW laser as in section 6.2 with 30 mW of power. The DMD is them imaged with a single 35 mm lens in a 4–f configuration to the object plane. The object used is an absorptive 1951 USAF resolution test target, line group -2 element 1. The lines in this group have a width of 2 mm. The target was rotated to show the 2D imaging capability of the system. The light transmitted by the target was collected using a 25 mm condenser lens and measured with a large-area photodiode (Thorlabs DET100A). The photodiode signal was sampled using a digitizer board (National Instruments PCI-6110) at a sample rate of 100 kHz, oversampling the DMD update frequency of 10 kHz. The target was imaged using both a 32x32 and a 20x20 superpixel grid both of which used 10000 frames

for a SPIFI frame rate and frequency resolution of 1 Hz. The resulting images are shown in Fig. 6.19.

Discussion. While these images clearly demonstrate two dimensional imaging using a DMD, the device is limited to a fairly small number of pixels due to the update rate of the device demonstrated. However, these technologies may find application in spectral regions where array detectors are not readily available or are cost prohibitive for large arrays. This system could be used across a broad spectral range, limited by the responsivity of the single-element detector and the reflectivity of the modulator. Our modulator is aluminum coated, which allows operating with reasonable efficiency out to 20 μm, so the 2D imaging system build here and operated with blue light could, by appropriate choice of detector, operate with thousands of pixels across the near-infrared and well in to the mid-infrared.

The number of pixels available can also be quite easily expanded. The limitation in this work is based on the on-board memory of the DMD. If more memory were added, the number of pixels could be expanded. In this work, the masks are all pre-loaded into a large memory buffer and then displayed at high speed. As the masks are quite simple, one could image a system which would create the modulation patterns on the fly, displaying each shortly after it was generated and disposing of it once it has been displayed. In this way, the limitation is then not on-board memory, but rather on the desired frame rate of the setup. Alternately, if a higher speed modulator were used, the number of pixels would correspondingly increased. This would allow operation at larger pixel counts (up to the number of pixels on the device itself) while using the same amount of memory.

CHAPTER 7

Coherent Holographic Imaging by Recovered Phase from Emission Distributions (CHIRPED)

In the previous section, we looked at expanding the SPIFI line imaging system to two dimensions, providing an x–y image using a single element detector. Here, we'll also expand the line image to two dimensions, this time in x–z, so we're able to simultaneously collect information about the object contrast function along the line focus dimension x and propagation phase information that gives the location of objects axial, along the beam propagation direction. Axial phase information is of interested as, even for systems with good lateral resolution, it can be challenging to get high axial resolution as the illumination beam has to pass through the sample to reach the detector, and will excite fluorophores or be absorbed by objects on either side of the focal plane. While this will still happen in this case, by encoding axial position information through propagation phase (analogous to holography), we can recover the location of objects along the propagation direction.

Holography encodes allows the capture of propagation phase through the interference of the object field and a reference field, which produces a fringe pattern which encodes the phase information and allows the field to be determined and propagated. This interference requires that coherence be maintained between the object and the reference beams, limiting its application to fluorescence emission as it lacks the requisite coherence. Attempts have been made at holographic imaging using incoherent illumination sources dating back practically to the invention of holography [61, 62]. These techniques involve imprinting a fresnel zone plate-type structure on the illumination light, then recording the zone plates transmitted by

the sample and using the recorded intensity to determine the distance from the sample to the camera. Similar techniques have been used to image fluorescent objects more recently [63]. While such techniques allow for holographic processing of fluorescent data, they require the user to project a Fresnel zone plate onto the sample and then raster scan the sample and record the fluorescent emission. This scanning can be eliminated by using a Spatial Light Modulator (SLM) and a CCD camera, as in [64]. In this case, the spatial light modulator is used to diffract fluorescent light from an object into two beams, which interfere with each other (as they are self-coherent) on a CCD camera. This method requires an SLM and a camera, and the update rate of one frame per second is limiting in the ability to capture rapid biological dynamics.

We introduce a method based on the SPIFI, called CHIRPED, that enables encoding of spatial phase information on a fluorescent signal by transferring the burden of coherence from the collection system to the illumination system. In a traditional holography system, the sample is illuminated by a coherent source and the light is coherently scattered by a sample and collected on a camera. A reference beam, which bypasses the sample, also illuminates the camera. Since the light is coherent, the camera captures an interference pattern created by the phase difference between the two fields. Encoded in this phase difference is the distance of the object that scattered the light from the camera. While the axial phase allows the location of these scatterers to be determined, the axial resolution will still be limited by the geometry of the experiment. As the conservation of momentum will require that the light is scattered to a small set of spatial frequencies, the axial resolution will be limited. This limitation is common to all types of holography, and can be remedied by making multiple measurements

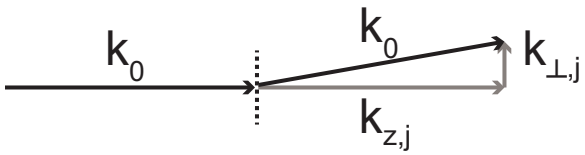

FIGURE 7.1. **k** vector depiction of plane wave grating interaction.

at a variety of incident angles (relative to the sample) and combining them, a process called diffraction tomography [65].

In CHIRPED, the phase information is encoded in by the sample as each point in the x–z plane experiences a unique temporal modulation, which encodes the position information in the fluorescence emission that faithfully follows the illumination intensity (per Sec. 5.2). The fluorescent signal from all parts of the object are then collected using a single element detector, with the fluorescence intensity from each position in x–z space also occupying a unique position in electronic frequency. The lateral position is encoded through frequency and the axial position encoded through electronic phase. Mapping these electronic frequency coordinates into spatial coordinates then allows the processing of these CHIRPED traces using standard holography techniques.

7.1. Theory

The analysis of this system begins by considering a mask, of the same form as in the one dimensional case (as shown in Fig. 5.3), illuminated by a plane wave travelling along the $\hat{z}$ direction and characterized by a wavevector $\mathbf{k}_0 = k_0\hat{z}$ with $k_0 = 2\pi/\lambda$. This wave is incident upon the mask grating, as shown in Fig. 7.1, where it is diffracted to some angle θ with respect to the optic axis. This diffracted vector can be written as the sum of its axial and transverse components, $\mathbf{k}_0' = \mathbf{k}_\perp + \mathbf{k}_z$, where $\mathbf{k}_\perp = k_x\hat{x} + k_y\hat{y}$ is the transverse k-vector. The axial and transverse components of the diffracted wavevector can be written as projections of the

incident vector

$$\mathbf{k}_{\perp} = k_0 \sin(\theta)\hat{\perp}$$

$$\mathbf{k}_z = k_0 \cos(\theta)\hat{z}$$

where the $\hat{\perp}$ is the grating direction. From geometry the axial k vector can also be written in terms of the input k vector and the transverse k vector

$$\mathbf{k}_z = k_0 \sqrt{1 - \frac{\left|\mathbf{k}_{(\perp,j)}\right|^2}{\left|\mathbf{k}_0\right|^2}}\hat{z}. \tag{7.1}$$

Here the subscript j has been introduced to signify the different k vectors corresponding to different orders of the grating diffraction. As the diffraction angle is assumed to be small, $\sin(\theta) \ll 1$ (equivalent here to $\left|\mathbf{k}_{(\perp,j)}\right| / \left|\mathbf{k}_{(z,j)}\right| \ll 1$), allowing us to write the above as an approximate

$$\mathbf{k}_z \approx k_0 \left(1 - \frac{1}{2}\frac{\left|\mathbf{k}_{(\perp,j)}\right|^2}{\left|\mathbf{k}_0\right|^2}\right)\hat{z}. \tag{7.2}$$

The mask is then imaged to the object plane, where the magnified version of the mask can be written as

$$M\mathbf{k}_z \approx k_0 \left(1 - \frac{M^2}{2}\frac{\left|\mathbf{k}_{(\perp,j)}\right|^2}{\left|\mathbf{k}_0\right|^2}\right)\hat{z} \tag{7.3}$$

with magnification M. Considering the modulator as a time varying diffraction grating, we can write the diffraction angle as $\sin(\theta) = j\lambda/d$ where d is the period of the grating and λ is the wavelength of the illuminating light. For our radially-dependent cosine mask, this grating period is time dependant and given by $d = (\kappa t)^{-1}$. This gives the transverse k vector as

$$\mathbf{k}_{(\perp,j)} = 2\pi j\kappa t\hat{\perp}. \tag{7.4}$$

Considering the mask used our imaging system, which is aligned such that the beam is focused to a thin line in x, with the modulator placed such that $\hat{x}$ and $\hat{1}$ are collinear. The modulator is defined by

$$m(r,\theta) = 1/2 + 1/2\cos(\Delta k r\theta) \tag{7.5}$$

The local spatial frequencies of this mask can then be found using the relations [42]

$$k_x = \frac{1}{2\pi}\frac{\partial}{\partial x} = \cos\theta\frac{\partial}{\partial r} - \frac{1}{r}\frac{\partial}{\partial\theta} \tag{7.6}$$

$$k_y = \frac{1}{2\pi}\frac{\partial}{\partial y} = \cos\theta\frac{\partial}{\partial r} - \frac{1}{r}\frac{\partial}{\partial\theta} \tag{7.7}$$

which gives the spatial frequencies in the x and y directions for a modulation mask in x as

$$k_{(x,j)} = 2\pi j\Delta k_x f_r t$$

$$k_{(y,j)} = \Delta k_y.$$

This allows us to write the perpendicular component as $\mathbf{k}_{(\perp,j)} = k_{(x,j)}\hat{x} + k_{(y,j)}\hat{y}$. The field of each diffracted beam j can be written in terms of $\mathbf{k}$, as

$$E_j(\mathbf{r}) = a_j \exp\left(\imath M\mathbf{k}_{(\perp,j)}\cdot\mathbf{r}_\perp\right)\exp\left[\imath k_0 z\left(1 - \frac{M^2}{2}\frac{k_{(\perp,j)}^2}{k_0^2}\right)\right] \tag{7.8}$$

which in terms of mask parameters is given by

$$E_j(\mathbf{r},t) = a_j \exp\left[\imath M\left(2\pi j\kappa t x + \Delta k y\right)\right]\exp\left[\imath k_0 z\left(1 - \frac{M^2}{2}\frac{(2\pi j\kappa t)^2 + \Delta k_y^2}{k_0^2}\right)\right] \tag{7.9}$$

The total field is then just given by the sum over all $\pm j$ gratings that can be collected by the imaging system. As there is diffraction in both x and y, we can use the fact that the positive and

negative sidebands are diffracted in opposite directions to easily block the negative sideband. By limiting our collection to only the zero and positive first diffracted order, we can write the field as

$$E(\mathbf{r},t) = \frac{1}{2}\exp(\imath k_0 z) + \frac{1}{4}\exp\left[\imath M\left(2\pi\kappa t x + \Delta k_y y\right)\right] \times \exp\left[\imath k_0 z\left(1 - \frac{M^2}{2}\frac{(2\pi\kappa t)^2 + \Delta k_y^2}{k_0^2}\right)\right]$$

If we collect this field using a lens which has been displaced slightly in $\hat{y}$, we can effectively remove the diffraction in y, allowing us to let $\Delta k_y \to 0$ and write the intensity as only a function of x and z as

$$I(x,z,t) = \frac{5}{16} + \frac{1}{4}\cos\left[2\pi\left(M\kappa t\right)x - \pi\lambda\left(M\kappa t\right)^2 z\right]. \tag{7.10}$$

Illuminating an object with contrast function $g(x,y)$ with this intensity and integrating on a single element detector we can write the temporal signal as

$$\begin{aligned} S(t) &= S_0 + S_1(t) \\ &= S_0 + \frac{1}{4}\iint_{-\infty}^{\infty}\cos\left[2\pi\left(M\kappa t\right)x - \pi\lambda\left(M\kappa t\right)^2 z\right] g(x,z)\,\mathrm{d}x\mathrm{d}z \end{aligned} \tag{7.11}$$

The signal, given by Eq. 7.11, is shown in Fig. 7.2(a) as a function of x and z for a few different times. The modulated intensity of a gaussian beam is plotted in Fig. 7.2(b) for several values of defocus, indicated by dots in Fig. 7.2(a). The instantaneous frequency of the modulation is shown for the same defocus values in Fig. 7.2(c). Selecting a single sideband transforms Eq. 7.11 simply into

$$S_{1+}(t) \propto e^{\imath 2\pi M\kappa x_0 t}\iint_{-\infty}^{\infty} e^{\imath 2\pi M\kappa x t} e^{-\imath\pi\lambda\left(M\kappa t\right)^2\left(z-z_0\right)} g(x,z)\,\mathrm{d}x\mathrm{d}z. \tag{7.12}$$

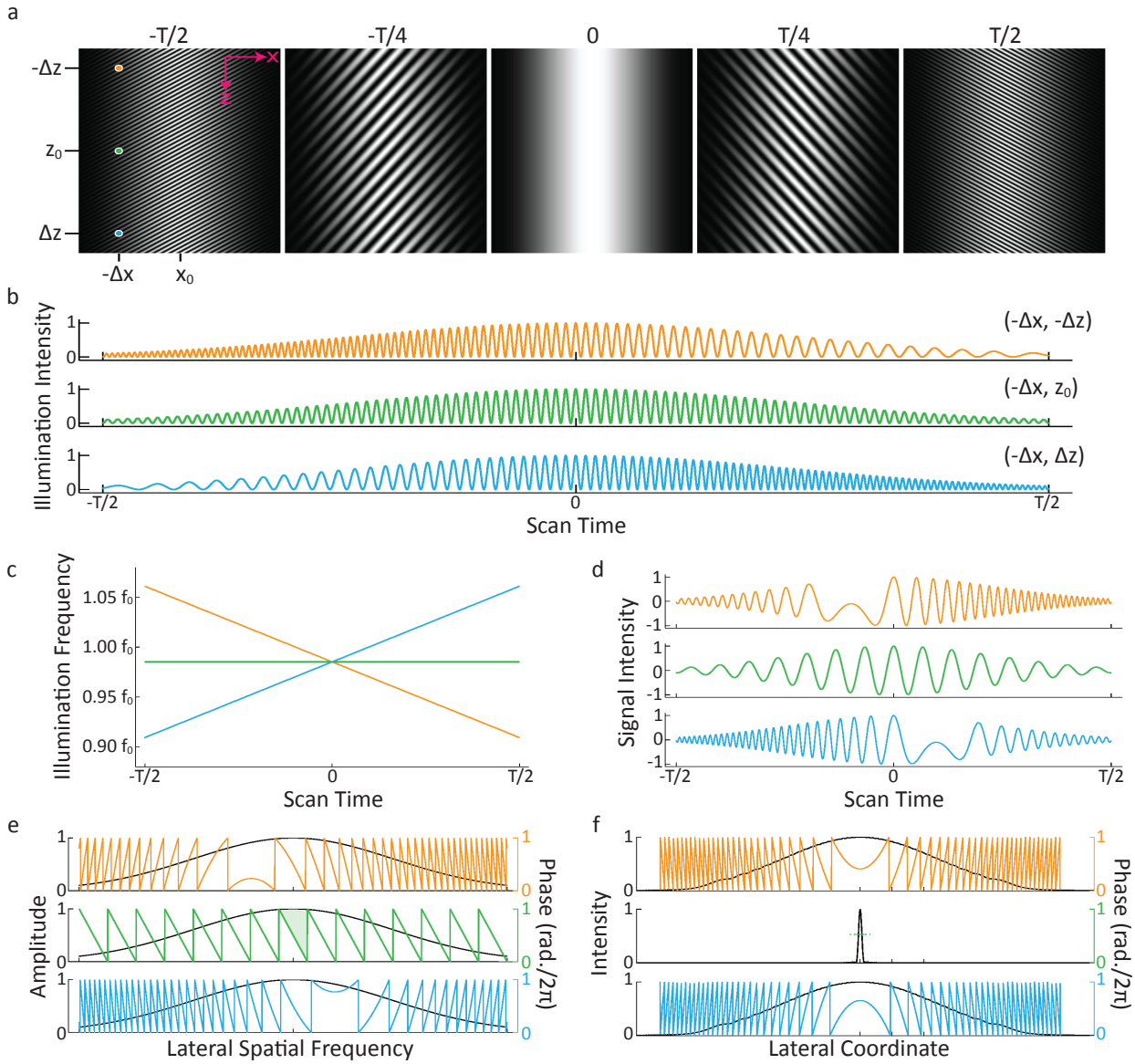

FIGURE 7.2. Spatial intensity modulation patterns over the rotation time are unique for all points in the x–z plane. (a) Illumination intensity patterns for several time instances during the time window of the modulator, T. (b) Illumination intensities and (c) instantaneous frequencies at three points with the same lateral shift but varying magnitude and sign of defocus. (d) Amplitude of the photodetector signal, $S_{1+}(t)$. (e) Amplitude and phase of the lateral spatial frequencies calculated from (d). (f) Amplitude and phase for each emitter in real space. From [66]

Where the x and z coordinates have been shifted to the beam center x_0 and focal plane z_0.

Equation 7.12 plotted for positive, negative, and no defocus is shown in Fig. 7.2(d). Making

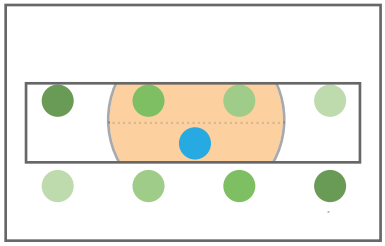

FIGURE 7.3. Diagram of the x and y diffraction and corresponding filtering. Multiple spots shown in the diffracted beams depict the scanning of diffracted beams laterally over the rotation of the modulator. The aperture, shown in gray, blocks the negative beam and the objective aperture, seen through the slit, is centered in the slit such that the y shear is eliminated.

the substitution from time to spatial frequency, $t \to f_x/(M\kappa)$, we can write

$$S_{1+}(f_x/(M\kappa)) \propto e^{\imath 2\pi f_x x_0} \int_{-\infty}^{\infty} e^{-\imath\pi\lambda(M\kappa t)^2(z-z_0)} G(f_x, z)\, \mathrm{d}z. \tag{7.13}$$

where $G(f_x, z)$ is the spatial Fourier transform in x. The amplitude and phase of the spatial frequencies are plotted in Fig. 7.2(e). Fourier transforming the temporal data gives back spatial information, shown in Fig. 7.2(f) for each defocus value.

7.2. Methods

The test setup for this experiment is a modification of the standard SPIFI setup (Fig. 5.1), where the previously discussed slit is inserted in an intermediate plane between the modulation plane and the sample plane and transmits only the positive sideband, as depicted in Fig. 7.3. The illumination source was a 532 nm diode pumped solid state continuous-wave laser with 200 mW average power (Changchun New Industries Optoelectronics Technology Co., Ltd., MGL-III-532).

The beam was spatially filtered with a 10x/0.25 NA objective lens (Zeiss A-Plan UIS) and a 10-μm pinhole before being collimated to a with of ~8.5 mm $1/e^2$ width an 80-mm focal length achromatic lens. The beam was then focused to a ~26 μm line in the mask plane using

a 300-mm focal length cylindrical lens. After passing through the modulator, the modulated line focused beam was re-imaged and demagnified with a 250-mm tube lens and a 10x/0.25 NA objective (Zeiss A-Plan UIS), which resulted in a magnification of 15.2.

An adjustable slit was placed in the focal plane between the tube lens and the objective, adjusted to block the negative diffracted order from the mask, as shown in Fig. 7.3. The fluorescent light was measured with a photomultiplier tube (Hamamatsu H9305-03). The current from the Photomultiplier Tube (PMT) was amplified and bandpass filtered (3 kHz–100 kHz) by a current pre-amplifier (Stanford Research Systems, SR570). Amplified and filtered signals were digitized with a data acquisition card (National Instruments PCI-6110).

To test the phase recovery, we imaged a single fluorescent sphere as we scanned it along the axis using a translation stage. Lateral images were taken at each axial position, and the stage position recorded. Having mapped out the amplitude of the signal in both x and z, we then select a single trace, taken at some position in z, and use this single trace to recover the amplitude and phase information using a standard Fresnel propagator for all other positions in x and z. This data is shown in Fig. 7.4, in which we can see excellent agreement between the measured and recovered images. To further show the dependence on the recovered propagation phase, we also propagate the amplitude from the same line out in z without the use of the propagation phase. This propagation deviates significantly from the measured data, demonstrating the accurate recovery of the propagation phase.

We then imaged multiple objects, distributed in both x and z. Two prepared slides of fluorescent spheres (LifeTechnologies, Focal Check Slides), stacked atop one another (and thus separated by their 1 mm thickness), and a set of lateral images were taken as a function of defocus by translating the slides along the optical axis and measuring a set of traces. A

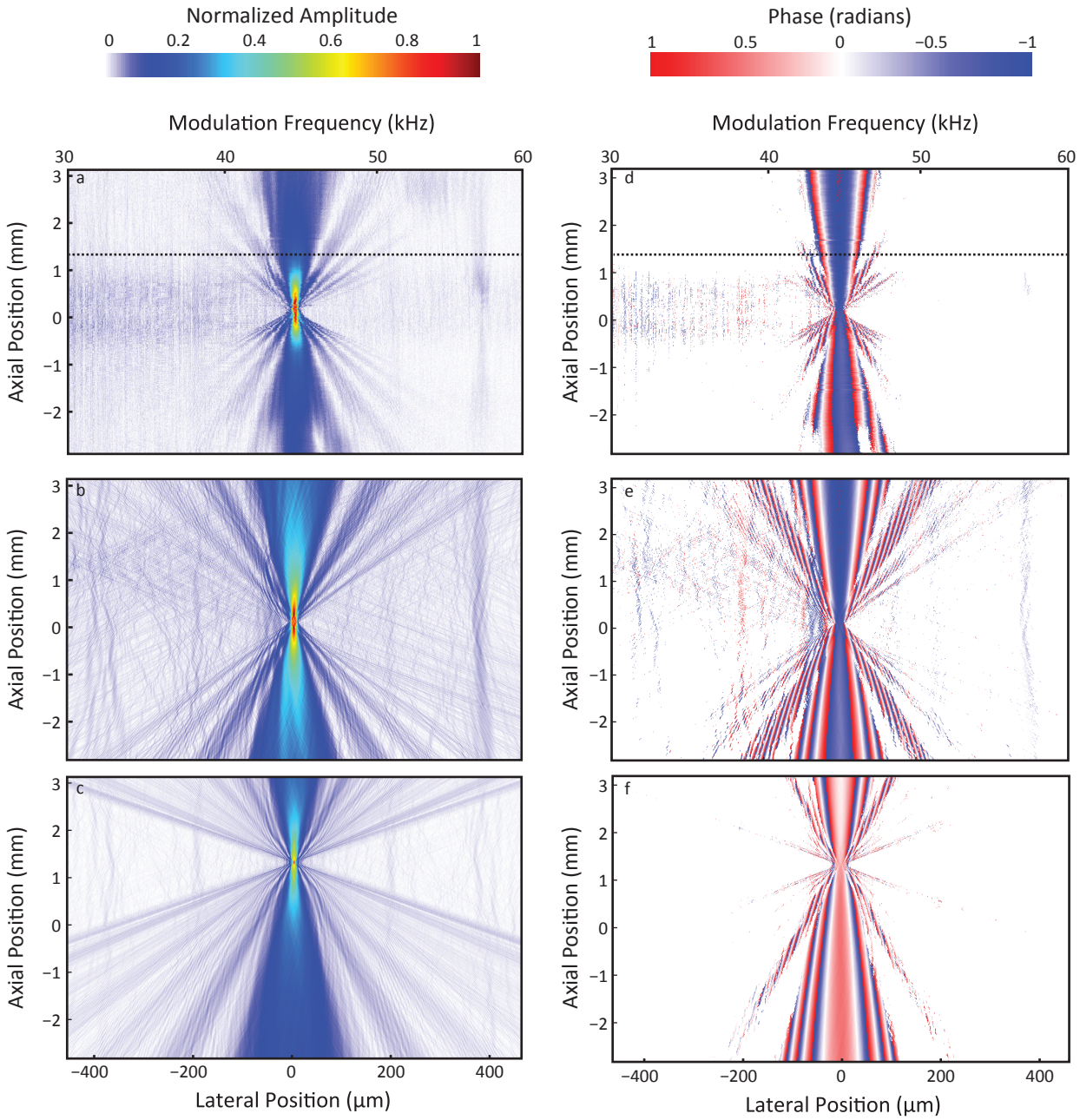

FIGURE 7.4. Amplitude and phase reconstruction of a fluorescent polystyrene bead (a) measured as a function of defocus and calculated by Fresnel propagation of the temporal data corresponding to the line in (a), both with (b) and without (c) using the recovered phase. The recovered phase corresponding to (a-c) is shown in panels (d-f). The digitally refocused image has an overall energy vs. defocus that is greater than the measured data. We attribute this to the finite depth of field of the measurement, which is not accounted for in the computed image.

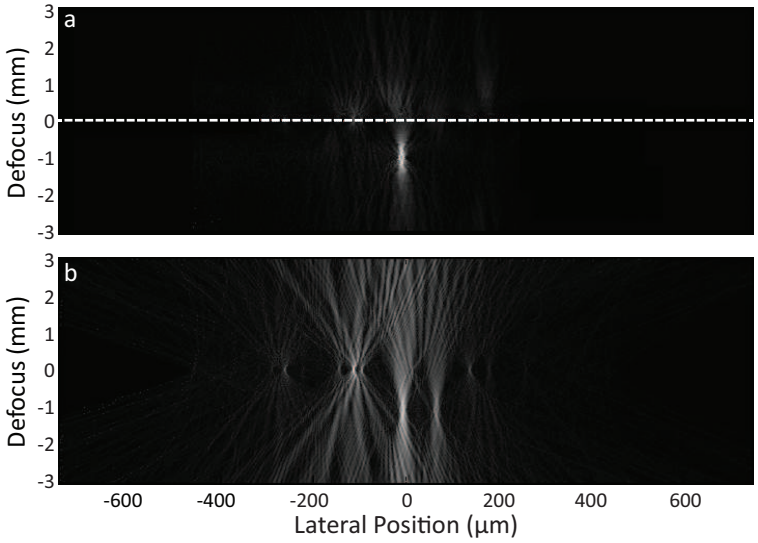

FIGURE 7.5. Image of a group of small beads axially separated from a group of large beads by 1 mm. These images were taken by (a) scanning the sample axially, then taking a single line image from the scan and (b) propagating it through the scan range.

single lateral trace is then extracted from the scan and propagated to each defocus position. Comparison of the propagated and translated traces, which are shown in Fig. 7.5, are in good agreement, demonstrating the captured phase information. As expected the axial extent of the object appears much longer that the lateral, demonstrating the expected limited axial resolution.

CHAPTER 8

Future Work

In this work, we've demonstrated new avenues for Raman detection by converting small frequency shifts born of the interaction of short probe pulse with the transient index of refraction created by impulsive interaction of a pump pulse with a Raman-active material into time delays using dispersion of a material. Also demonstrated were a series of single-pixel imaging techniques applied to one dimensional line imaging, two dimensional x–y imaging, and two dimensional x–z imaging.

The groundwork has been laid here for significant improvement in Raman sensitivity. The sensitivity in this work was limited by excess noise in locking electronics used to make the phase measurements, as well as the $1/f$ noise of the VCO themselves. To improve upon this sensitivity, we can press in two directions: improvement of the locking electronics and moving to higher modulation frequencies. Using a higher modulation frequency is the most straightforward way to improve the sensitivity. Even with the VCO we currently have, the phase noise is lower by 20 dB if we move from a modulation frequency of 100 kHz to a modulation frequency of 1 MHz. To ensure we can reach these low phase noise levels, we'll require improved locking electronics. We'll also need to ensure that the power level is sufficient to be in a regime where the noise floor will be limited by the VCO and not by shot noise.

To keep our power high, we must eliminate as many sources of loss as possible. Currently, the main sources of power loss in our probe measurement system are the amplitude modulators and the long fiber. The amplitude modulators have a loss of about 5 dB. These could be replaced with lower loss models, as 3 dB insertion loss modulators are widely available at a premium price. We could lower the fiber loss by either using a fiber with lower loss

per kilometer, or by using less fiber. As reducing the loss of the fiber is not feasible (most reasonable fibers have similar losses), we must look at reducing fiber length. Such length reductions will necessarily decrease the applied dispersion, and thus reduce the change in time delay for a given frequency shift. To compensate for this loss in timing, we can measure the signal as a function of a higher harmonic of the repetition rate, such that the time delay is divided a factor of N but the frequency is multiplied by the same factor, keeping the phase to be measured constant. In this way, we should be able to employ shorter fibers without a loss of sensitivity. This scheme may also have the added benefit of lower noise, as we may be picking up noise from fluctuations in such a long fiber.

Future work in the SPIFI experiments is also plentiful, as many applications shown here are the first demonstrations of the technology, and many refinements are possible. The SPIFI spectrometer has taken only preliminary data, and many exciting MIR spectral measurements are waiting to be made with the next generation instrument, which will feature a larger bandwidth made possible by the construction of a larger modulator. The application of the modulated spectrum to a hyperspectral measurement is another exciting avenue ready to be explored. Experiments are ongoing in both of these areas.

Two dimensional SPIFI has been demonstrated showing x–y and x–z imaging. A simple modification of the dual-disk x–y SPIFI system will be built to take advantage of some of the novel reconstruction methods described in this document, allowing higher frame rates and increased resolution. To further increase speed, a next generation system could be built using a disk to modulate in one dimension and an AOD in the other dimension, potentially allowing the slower disk to be run at several hundred hertz due to the very high bandwidth of AOD. Such a system could also be implemented using a two dimensional AOD, which would

not require any spinning disks, eliminating a potential source of error. This 2D system could also be improve with more sophisticated reconstruction algorithms, relaxing the spin rate requirement and adding flexibility to the optical setup at the cost of more advanced processing.

Further improvements on the CHIRPED imaging system could be made by increasing speed using a modulator disk printed with multiple masks per disk, relaxing the speed constraint imposed by the motor. A galvonometer could be used to rapidly scan in the alternate dimension, allowing for three dimensional scans to be completed on a time scale limited by the spinning disk. Three dimensional imaging could also be achieved by combining both two-dimensional SPIFI techniques to yield full three dimensional information using a single detector, without need for scanning. Axial resolution can also be enhanced by building diffraction tomography in to the CHIRPED setup.

Finally, the DMD could be readily applied to mid-infrared wavelength, which could readily benefit from even the 1000 pixel arrays demonstrated here. Moving to a larger number of pixels would require longer acquisition times, given the limited update rate of the DMD. We are currently limited in time duration by on-board memory, as we are generating the masks offline, loading them into memory, and the Field-Programmable Gate Array (FPGA) that controls the DMD then displays the images one at a time. As the calculation of the masks is quite simple, it may be reasonable to program the FPGA to generate the masks on the fly, just before they are displayed. This would allow the acquisition time to be made arbitrarily long, limited only by the patience of the experimenter.

REFERENCES

[1] D. Gabor, “A New Microscopic Principle,” *Nature*, vol. 161, pp. 777–778, 1948.

[2] E. N. Leith and J. Upatnieks, “Wavefront Reconstruction with Continuous-Tone Objects,” *J. Opt. Soc. Am.*, vol. 53, no. 12, pp. 1377–1381, 1963.

[3] E. V. Efremov, F. Ariese, and C. Gooijer, “Achievements in resonance Raman spectroscopy Review of a technique with a distinct analytical chemistry potential.,” *Anal. Chim. Acta*, vol. 606, no. 2, pp. 119–134, Jan. 2008.

[4] N. Bloembergen, “The Stimulated Raman Effect,” *Am. J. Phys.*, vol. 35, no. 11, p. 989, 1967.

[5] D. A. Long, *The Raman Effect: A Unified Treatment of the Theory of Raman Scattering by Molecules*. London, 2002, vol. 8, pp. 1–471.

[6] R. Boyd, *Nonlinear Optics, Third Edition [Hardcover]*. Academic Press; 3 edition, 2008, p. 640.

[7] J. X. Cheng, L. D. Book, and X. S. Xie, “Polarization coherent anti-Stokes Raman scattering microscopy.,” *Opt. Lett.*, vol. 26, no. 17, pp. 1341–3, Sep. 2001.

[8] S. O. Konorov, M. W. Blades, and R. F. B. Turner, “Non-resonant background suppression by destructive interference in coherent anti-Stokes Raman scattering spectroscopy.,” *Opt. Express*, vol. 19, no. 27, pp. 25 925–34, Dec. 2011.

[9] F. Ganikhanov, C. L. Evans, B. G. Saar, and X. S. Xie, “High-sensitivity vibrational imaging with frequency modulation coherent anti-Stokes Raman scattering (FM CARS) microscopy.,” *Opt. Lett.*, vol. 31, no. 12, pp. 1872–4, Jun. 2006.

[10] A. Rae, R. Stosch, P. Klapetek, A. R. Hight Walker, and D. Roy, “State of the Art Raman Techniques for Biological Applications.,” *Methods*, vol. 68, no. 2, pp. 338–347, Mar. 2014.

[11] C. Freudiger, W. Min, B. Saar, S. Lu, G. Holtom, C. He, J. C. Tsai, J. X. Kang, and X. S. Xie, "Label-free biomedical imaging with high sensitivity by stimulated Raman scattering microscopy," *Science (80-.).*, vol. 322, pp. 1857–1861, 2008.

[12] L. Dhar, J. A. Rogers, and K. A. Nelson, "Time-Resolved Vibrational Spectroscopy in the Impulsive Limit," *Chem. Rev.*, vol. 94, pp. 157–193, 1994.

[13] A. M. Weiner, D. E. Leaird, G. P. Wiederrecht, and K. A. Nelson, "Femtosecond Pulse Sequences Used for Optical Manipulation of Molecular Motion," *Science (80-.).*, vol. 247, no. 4948, pp. 1317–1319, 1990.

[14] R. Bartels, T. Weinacht, S. Leone, H. Kapteyn, and M. Murnane, "Nonresonant Control of Multimode Molecular Wave Packets at Room Temperature," *Phys. Rev. Lett.*, vol. 88, no. 3, p. 033 001, Jan. 2002.

[15] J. K. Wahlstrand, R. Merlin, X. Li, S. T. Cundiff, and O. E. Martinez, "Impulsive stimulated Raman scattering: comparison between phase-sensitive and spectrally filtered techniques.," *Opt. Lett.*, vol. 30, no. 8, pp. 926–8, Apr. 2005.

[16] J. W. Wilson, P. Schlup, and R. A. Bartels, "Synthetic temporal aperture coherent molecular phase spectroscopy," *Chem. Phys. Lett.*, vol. 463, no. 4-6, pp. 300–304, Oct. 2008.

[17] J. W. Wilson, P. Schlup, and R. A. Bartels, "Phase measurement of coherent Raman vibrational spectroscopy with chirped spectral holography.," *Opt. Lett.*, vol. 33, no. 18, pp. 2116–8, Sep. 2008.

[18] J. W. Wilson and R. A. Bartels, "Coherence-modulated third harmonic generation for vibrational spectroscopy: a theoretical treatment," *J. Opt. Soc. Am. B*, vol. 29, no. 8, pp. 1875–1883, 2012.

[19] X. J. Wang, T. E. Milner, and J. S. Nelson, “Characterization of fluid flow velocity by optical Doppler tomography.,” *Opt. Lett.*, vol. 20, no. 11, pp. 1337–9, Jun. 1995.

[20] D. Censor and J. Brandstatter, “Generalized doppler effect in time-varying media,” *J. Franklin Inst.*, pp. 485–490, 1974.

[21] N. N. Rozanov and A. S. Kiselev, “The Doppler frequency shift caused by the inhomogeneities of a medium induced by pulses of intense laser radiation,” *Opt. Spectrosc.*, vol. 105, no. 2, pp. 268–269, 2008.

[22] R. Merlin, “Generating Coherent THz Phonons with Light Pulses,” *Solid State Commun.*, vol. 102, pp. 207–220, 1997.

[23] T. Ideguchi, S. Holzner, B. Bernhardt, G. Guelachvili, N. Picqué, and T. W. Hänsch, “Coherent Raman spectro-imaging with laser frequency combs.,” *Nature*, vol. 502, no. 7471, pp. 355–8, Oct. 2013.

[24] P. C. Hobbs, “Reaching the Shot Noise Limit for $10,” *Opt. Photonics News*, pp. 17–23, 1991.

[25] T. R. Schibli, J. Kim, O. Kuzucu, J. T. Gopinath, S. N. Tandon, G. S. Petrich, L. A. Kolodziejski, J. G. Fujimoto, E. P. Ippen, and F. X. Kaertner, “Attosecond active synchronization of passively mode-locked lasers by balanced cross correlation.,” *Opt. Lett.*, vol. 28, no. 11, pp. 947–9, Jun. 2003.

[26] E. N. Ivanov, S. A. Diddams, and L. Hollberg, “Analysis of Noise Mechanisms Limiting the Frequency Stability of Microwave Signals Generated With a Femtosecond Laser,” *IEEE J. Sel. Top. Quantum Electron.*, vol. 9, no. 4, pp. 1059–1065, 2003.

[27] F. Quinlan, T. M. Fortier, H. Jiang, A. Hati, C. Nelson, Y. Fu, J. C. Campbell, and S. A. Diddams, "Exploiting shot noise correlations in the photodetection of ultrashort optical pulse trains," *Nat. Photonics*, vol. 17, pp. 290–293, 2013.

[28] J. Kim, F. X. Kärtner, and M. H. Perrott, "Femtosecond synchronization of radio frequency signals with optical pulse trains.," *Opt. Lett.*, vol. 29, no. 17, pp. 2076–8, Sep. 2004.

[29] J. Kim, F. X. Kärtner, and F. Ludwig, "Balanced optical-microwave phase detectors for optoelectronic phase-locked loops.," *Opt. Lett.*, vol. 31, no. 24, pp. 3659–61, Dec. 2006.

[30] K. Jung and J. Kim, "Subfemtosecond synchronization of microwave oscillators with mode-locked Er-fiber lasers.," *Opt. Lett.*, vol. 37, no. 14, pp. 2958–60, Jul. 2012.

[31] W. H. Steier, "A Push-Pull Optical Amplitude Modulator," *IEEE J. Quantum Electron.*, vol. QE-3, no. 12, pp. 664–667, 1967.

[32] S. Dubovitsky, W. H. Steier, S. Yegnanarayanan, and B. Jalali, "Analysis and Improvement of Mach–Zehnder Modulator Linearity Performance for Chirped and Tunable Optical Carriers," *J. Light. Technol.*, vol. 8724, no. May, pp. 886–891, 2002.

[33] T. M. Fortier, M. S. Kirchner, F. Quinlan, J. Taylor, J. C. Bergquist, T. Rosenband, N. Lemke, A. Ludlow, Y. Jiang, C. W. Oates, and S. A. Diddams, "Generation of ultrastable microwaves via optical frequency division," *Nat. Photonics*, vol. 5, pp. 425–429, 2011.

[34] J. Kim and F. Kärtner, "Attosecond-precision ultrafast photonics," *Laser Photon. Rev.*, vol. 4, no. 3, pp. 432–456, Apr. 2010.

[35] J. S. Sanders, R. G. Driggers, C. E. Halford, and S. T. Griffin, "Imaging with frequency-modulated reticles," *Opt. Eng.*, vol. 30, no. 11, pp. 1720–1724, 1991.

[36] J. S. Taylor, R. G. Driggers, C. E. Halford, J. S. Sanders, S. T. Griffin, and M. Wellfare, "Comparison of continuous and discrete frequency-versus-radius frequency-modulated reticles," *Appl. Opt.*, vol. 31, no. 10, pp. 1638–1640, 1992.

[37] J. S. Taylor and R. G. Driggers, "Tracking with two frequency-modulated reticles," *Opt. Eng.*, vol. 32, no. 5, pp. 1101–1104, 1993.

[38] J.-k. Bae, Y.-h. Doh, D.-s. Noh, and S.-j. Kim, "Imaging system using frequency modulation/time division multiplexing hybrid reticle," *Opt. Eng.*, vol. 37, no. 7, pp. 2119–2123, 1998.

[39] G. Futia, P. Schlup, D. G. Winters, and R. A. Bartels, "Spatially-chirped modulation imaging of absorbtion and fluorescent objects on single-element optical detector," *Opt. Express*, vol. 19, no. 2, pp. 489–503, Jan. 2011.

[40] E. E. Hoover, J. J. Field, D. G. Winters, M. D. Young, E. V. Chandler, J. C. Speirs, J. T. Lapenna, S. M. Kim, S.-Y. Ding, R. A. Bartels, J. W. Wang, and J. A. Squier, "Eliminating the scattering ambiguity in multifocal, multimodal, multiphoton imaging systems.," *J. Biophotonics*, vol. 12, pp. 1–12, Mar. 2012.

[41] D. J. Higley, D. G. Winters, G. L. Futia, and R. A. Bartels, "Theory of diffraction effects in spatial frequency-modulated imaging.," *J. Opt. Soc. Am. A*, vol. 29, no. 12, pp. 2579–90, Dec. 2012.

[42] J. W. Goodman, *Introduction to Fourier Optics*. Roberts and Company Publishers, 2005, p. 491.

[43] D. Lovell, *Electro-Optical Position Indicator System*, 1961.

[44] J. R. Lakowicz and A. Balter, "Theory of Phase-Modulation Fluorescence Spectroscopy for Excited-State Processes," *Biophys. Chem.*, vol. 16, pp. 99–115, 1982.

[45] J. R. Lakowicz, “Frequency-Domain Lifetime Measurements,” in *Princ. Fluoresc. Spectrosc.* 2010, pp. 157–204.

[46] J. M. Chalmers and P. R. Griffiths, Eds., *Handbook of Vibrational Spectroscopy*. Chichester, UK: John Wiley & Sons, Ltd, Jun. 2006.

[47] B. C. Smith, *Fundamentals of Fourier Transform Infrared Spectroscopy*. CRC Press, 2011, p. 207.

[48] C. Palmer and E. Loewen, *Diffraction Grating Handbook*, 6th ed. New York, 2005, pp. 1–265.

[49] J. F. James, *Spectrograph Design Fundamentals*. Cambridge University Press, 2007, pp. 63–88.

[50] J. M. Lerner, “Imaging Spectrometer Fundamentals for Researchers in the Biosciences –– A Tutorial,” *Cytom. Part A*, vol. 69A, pp. 712–734, 2006.

[51] P. Schlup, G. Futia, and R. A. Bartels, “Lateral tomographic spatial frequency modulated imaging,” *Appl. Phys. Lett.*, vol. 98, no. 21, p. 211 115, 2011.

[52] D. J. Higley, D. G. Winters, and R. A. Bartels, “Two-dimensional spatial-frequency-modulated imaging through parallel acquisition of line images,” *Opt. Lett.*, vol. 38, no. 11, pp. 1763–5, Jun. 2013.

[53] D. J. Thomson, “Spectrum Estimation and Harmonic Analysis,” *Proc. IEEE*, vol. 70, no. 9, pp. 1055–1096, 1982.

[54] F. P. Martial and N. A. Hartell, “Programmable illumination and high-speed, multi-wavelength, confocal microscopy using a digital micromirror.,” *PLoS One*, vol. 7, no. 8, e43942, Jan. 2012.

[55] Q. S. Hanley, P. J. Verveer, M. J. Gemkow, D. Arndt-Jovin, and T. M. Jovin, “An optical sectioning programmable array microscope implemented with a digital micromirror device.,” *J. Microsc.*, vol. 196, no. Pt 3, pp. 317–31, Dec. 1999.

[56] T. Fukano and A. Miyawaki, “Whole-field fluorescence microscope with digital micromirror device: imaging of biological samples.,” *Appl. Opt.*, vol. 42, no. 19, pp. 4119–24, Jul. 2003.

[57] J. D. Lechleiter, D.-T. Lin, and I. Sieneart, “Multi-photon laser scanning microscopy using an acoustic optical deflector.,” *Biophys. J.*, vol. 83, no. 4, pp. 2292–9, Oct. 2002.

[58] R. Salomé, Y. Kremer, S. Dieudonné, J.-F. Léger, O. Krichevsky, C. Wyart, D. Chatenay, and L. Bourdieu, “Ultrafast random-access scanning in two-photon microscopy using acousto-optic deflectors.,” *J. Neurosci. Methods*, vol. 154, no. 1-2, pp. 161–74, Jun. 2006.

[59] H. Nyquist, “Certain Topics in Telegraph Transmission Theory,” *Proc. IEEE*, vol. 90, no. 2, pp. 280–305, 2002.

[60] C. Shannon, “Communication In The Presence Of Noise,” *Proc. IEEE*, vol. 86, no. 2, pp. 447–457, Feb. 1998.

[61] A. W. Lohmann, “Wavefront Reconstruction for Incoherent Objects,” *J. Opt. Soc. Am.*, vol. 55, pp. 1555–1556, 1965.

[62] P. J. Peters, “Incoherent Holograms With Mercury Light Source,” *Appl. Phys. Lett.*, vol. 8, no. 8, p. 209, 1966.

[63] B. W. Schilling, T. C. Poon, G. Indebetouw, B. Storrie, K. Shinoda, Y. Suzuki, and M. H. Wu, “Three-dimensional holographic fluorescence microscopy.,” *Opt. Lett.*, vol. 22, no. 19, pp. 1506–8, Oct. 1997.

[64] J. Rosen and G. Brooker, “Non-scanning motionless fluorescence three-dimensional holographic microscopy,” *Nat. Photonics*, vol. 2, no. 3, pp. 190–195, Feb. 2008.

[65] A. J. Devaney, “A Filtered Backpropagation Algorithm for Diffraction Tomography,” *Ultrason. Imaging*, vol. 4, pp. 336–350, 1982.

[66] J. J. Field, D. G. Winters, and R. A. Bartels, “Phase-sensitive planar epi-fluorescent imaging with coherent diffractive reconstruction,” *Submitt. to Nat.*, 2014.

APPENDIX A

Carbon Tetrachloride Concentration

As an example of the conversion of Raman excitation into frequency shift, we'll use Carbon Tetrachloride (CCl_4), as it has well know modes and absolute cross sections. Starting with the expression for the amplitude of the sinusoidal modulation given in Eq. 2.4,

$$\delta\phi_0 = \frac{\omega\ell}{2nc}\frac{N}{\varepsilon_0}(\alpha')^2\frac{1}{\Omega_v}\left|D\left(\Omega_v\right)\right|. \tag{A.1}$$

We begin by making the substitution to convert from the differential polarizability, α' to the differential Raman cross-section, $\frac{\partial\sigma}{\partial\Omega}$, from [1]

$$\frac{\partial\sigma}{\partial\Omega} = \frac{h}{8\varepsilon_0^2 c\tilde{\nu}_Q}\left(\tilde{\nu}-\tilde{\nu}_Q\right)^4\left(\frac{45\left|\alpha'\right|^2+7\gamma'^2}{45}\right)\frac{1}{1-\exp\left(-\frac{hc\tilde{\nu}_Q}{k_BT}\right)} \tag{A.2}$$

where $\tilde{\nu}$ and $\tilde{\nu}_Q$ are the frequencies of the incident light and the vibrational mode in wavenumbers, respectively, c is the speed of light, ε_0 is the permittivity of free space, h is Planck's constant, k_B is Boltzmann's constant, T is temperature, and α' and γ' are the isotropic and anisotropic polarizability derivatives.

As Carbon Tetrachloride is isotropic [2], the anisotropic term goes to zero, $\gamma' = 0$. The temperature dependance will be dropped, as it is negligible near room temperature. We'll also convert the frequencies from wavenumbers to angular frequency and format the notation to be consistent with the Eq. A.1.

$$\frac{\partial\sigma}{\partial\Omega} = \frac{\hbar}{32\varepsilon_0^2 c^4\pi^2\Omega_v}\left(\omega-\Omega_v\right)^4\left|\alpha'\right|^2. \tag{A.3}$$

Solving this equation for $|\alpha'|^2$ and substituting into Eq. A.1, we get $\delta\phi_0$ in terms of $\frac{\partial\sigma}{\partial\Omega}$,

$$\delta\phi_0 = \omega\ell\frac{16N\varepsilon_0 c^3\pi^2}{n\hbar\left(\omega-\Omega_v\right)^4}\left|D\left(\Omega_v\right)\right|. \tag{A.4}$$

The final necessary variable is the autocorrelation $D(\Omega_v)$. To calculate this, we'll consider a Gaussian temporal pulse

$$E(t) = E_0\exp\left(at^2\right) \tag{A.5}$$

where $a = 2\log(2)/\tau_p^2$ and τ_p is the transform limited pulse duration full-width at half max. The spectrum is then given as

$$E(\omega) = \frac{E_0}{\sqrt{2a}}\exp\left(\frac{\omega^2}{4a}\right) \tag{A.6}$$

From the definition of $D(\Omega_v)$ we write the autocorrelation as

$$\begin{aligned}\left|D(\Omega_v)\right| &= \int_{-\infty}^{\infty} E(\omega)E^*(\omega-\Omega_v)\mathrm{d}\omega \\ &= \frac{E_0^2\tau}{8\log(2)}\sqrt{\frac{\log(16)}{\pi}}\exp\left(-\frac{\tau_p^2\Omega_v^2}{16\log(2)}\right)\end{aligned}$$

From the temporal intensity, we can calculate the fluence of the pulse

$$\begin{aligned}U &= \int_{-\infty}^{\infty} I(t)\mathrm{d}t \\ &= \frac{1}{2}\varepsilon_0 cnE_0^2\tau\sqrt{\frac{\pi}{\log(16)}} \\ \frac{\mathcal{E}}{\pi w^2} &= \frac{1}{2}\varepsilon_0 cnE_0^2\tau\sqrt{\frac{\pi}{\log(16)}}\end{aligned}$$

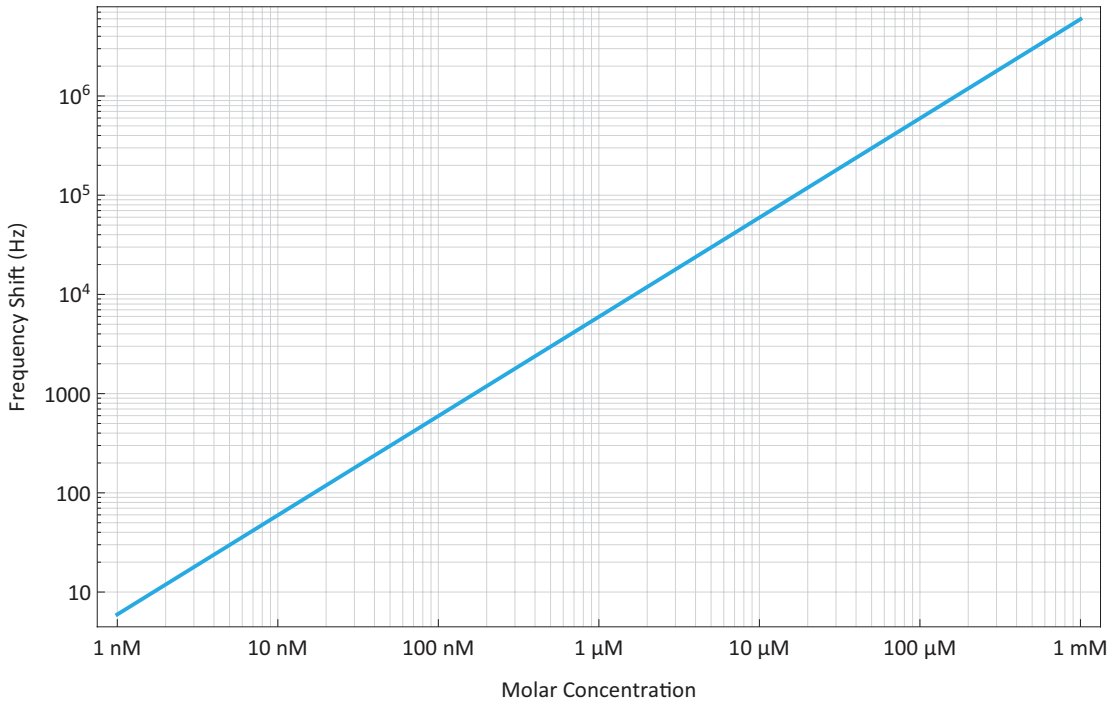

FIGURE A.1. Frequency shift as a function of molar concentration of CCl_4.

Assuming a uniform circular beam, we can write the area of the beam in terms of the width parameter w simply as $A = \pi w^2$. We can then write the fluence in terms of the pulse energy $\mathcal{E}$ and solve for E_0^2, bringing us finally to

$$\left|D(\Omega_v)\right| = \frac{\mathcal{E}}{\pi w^2}\frac{1}{cn\pi\varepsilon_0}\exp\left(-\frac{\tau_p^2\Omega_v^2}{16\log(2)}\right)$$

which allows us to write the differential phase as

$$\delta\phi_0 = \frac{\mathcal{E}}{w^2}\frac{16c^2N\ell}{\hbar n^2(\omega-\Omega_v)^4}\frac{\partial\sigma}{\partial\Omega}\exp\left(-\frac{\tau_p^2\Omega_v^2}{16\log(2)}\right). \tag{A.7}$$

To get an idea of the magnitude of the frequency shift, we'll calculated the expected shifts in terms of the laser parameters used in this work. The differential scattering cross section of pure CCl_4 is 5.6×10^{-35} m^2 and its molar concentration is 10.3 mol/L. Illuminating it with a Ti:Sapphire laser with a center wavelength $\lambda = 800$ nm, with a pulse duration $\tau = 15$ fs, and

a pulse energy of $\mathcal{E} = 1$ nJ. The beam is focus with a 0.95 NA objective, which was used to calculate the focal volume following [3]. These parameters give a frequency shift of 61 GHz for neat CCl_4. Varying the molar concentration allows us to see how concentration maps to frequency shift, as shown in Fig. A.1.

APPENDIX B

Allan Variance to Phase Noise

Allan variance, typically written as $\sigma_y^2(\tau)$, is a time-domain measure of the frequency stability of a clock. In this measurement, the average fractional frequency $\bar{y}_n$ of a clock is measured over some time period τ, where n is the measurement number [4]. The Allan variance is then calculated from the square of the difference between two adjacent measurements,

$$\sigma_y^2(\tau) = \frac{1}{2}\left\langle (\bar{y}_{n+1} - \bar{y}_n)^2 \right\rangle \tag{B.1}$$

where the angle braces, ⟨⟩, indicate the expectation value of the measurement. The τ dependence here shows that the value of the Allan variance changes with the observation time, and thus Allan variance is often plotted as a function of τ. The type of noise can then be estimated from this plot by looking at the dependence of the variance on τ.

In this work, we've previously characterized our measurement system in terms of phase noise. As both the time-domain Allan variance and the frequency-domain phase noise express the stability of frequency sources, the value of one metric can be determined from the other [5]. For an oscillator dominated by white phase noise, the Allan variance can be converted to the single-sideband phase noise using the relation

$$S_\phi(f) = \frac{4\pi^2}{3f_B}\tau^2\sigma_y^2(\tau)f^2 \tag{B.2}$$

where $\sigma_y^2(\tau)$ is the Allan variance for a nominal frequency f, τ is again the sample separation, and f_B is the measurement bandwidth.

Amplitude noise measured on the photodiode will manifest as white phase noise in the photodiode pulse train. In the shot noise limit of the photodetector, the Allan variance of the recovered RF signal is [6]

$$\sigma_y(\tau) \approx \frac{1}{2\pi\tau m f_r}\sqrt{\frac{3P_{\text{shot}}}{P_{\text{signal}}}} \tag{B.3}$$

where the approximate relation indicates this contribution is assumed to be white phase noise. In this equation, P_{signal} is the power of the microwave signal from the photodiode at the desired harmonic m of the repetition rate frequency mf_r and $P_{\text{shot}} = 2qf_B R_p P_d R$ is the shot-noise power of the incident light on the photodiode, where q is the electron charge, R_p is the photodiode responsivity, P_d is the average power incident on the photodiode, and R is the load impedance. The sample separation in the Allan variance is again τ.

As Eq. B.3 has already been assumed to be only white phase noise, we can use Eq. B.2 to convert the Allan variance given in Eq. B.3 to phase noise, yielding

$$S_\phi(f) = \frac{P_{\text{shot}}}{P_{\text{signal}} f_B} \tag{B.4}$$

where P_{signal} and P_{shot} are as above, and f_B is the measurement bandwidth.

APPENDIX C

Phase Measurement

Measurement of frequency fluctuations are made by measuring the oscillator under test against a reference oscillator using a phase sensitive detector. The detector converts the phase fluctuations into a voltage which can be easily recorded. As the time delay of the pulse through the optical fiber changes, the phase of the repetition rate frequency measured at the photodetector will also change. The magnitude of this phase change is related to the magnitude of the frequency shift, which is the desired measurement quantity.

We'll modulate the experimentally produced delay signal, giving rise to an RF phase change which varies with time. This variation in RF phase will manifest as a peak in the spectrum at a small offset from the carrier frequency, which will be easier to measure accurately than a direct phase measurement. The measurement accuracy as a function of the offset frequency is ultimately limited by the phase noise at that offset, which is to say that the measurement of the induced timing signal can be no smaller than the intrinsic jitter of the system. Thus, we're interested in the measurement not only of the signal of interest, but also the noise characteristics of both the optical system and the associated measurement electronics for offsets near the carrier frequency.

All frequency sources exhibit some fluctuation in frequency over some period of time. This instability in an assumed pure frequency can be characterized by the phase noise of the oscillator in the frequency domain [7] or by the Allan variance [4] in the time domain. For a pure sinusoidal signal $S(t) = \sin(2\pi\nu t)$ corrupted by a random time-dependant phase $\Delta\phi(t)$, we can write the phase argument as $\Phi = 2\pi\nu t + \delta\phi(t)$. The phase noise of this oscillator can

then be written in terms of the single-sided spectral density as

$$S_{\Delta\varphi}(f) = \frac{\Delta\varphi_{\text{rms}}^2}{f_{\text{BW}}} \tag{C.1}$$

where f is the positive frequency offset from the carrier frequency ν and f_{BW} is the bandwidth used in the measurement of $\Delta\varphi_{\text{rms}}$. The units of this measure are $\frac{\text{rad.}^2}{\text{Hz}}$. Another common definition of phase noise is given as the ratio of the one-sided power spectral density of the oscillator to the oscillator power. This is often denoted $\mathcal{L}(f)$, where f is again the offset frequency, and for small phase deviations can be approximated [7] as

$$\mathcal{L}(f) = \frac{P_{\text{SSB}}}{P_{\text{S}}} \approx \frac{1}{2} S_{\Delta\varphi}(f). \tag{C.2}$$

$\mathcal{L}(f)$ is typically expressed in units of dBc/Hz, decibels relative to the carrier per Hz.

This power measurement can be easily made directly using a spectrum analyzer by connecting the device to be measured to the analyzer and measuring the single-sideband power spectral density of the device. This can then be scaled by the oscillator power to yield a measure of $\mathcal{L}(f)$. While this measurement is simple to make, it is limited in sensitivity for two reasons: first, the phase noise of the device to be measured needs to significantly less than the phase noise of the spectrum analyzer, as the measured value will be the sum of the two noise contributions. Second, amplitude noise on the device under test and spurious signals will also be seen by the spectrum analyser, further corrupting the measured phase noise.

To measure oscillators with noise levels below or near the level of the spectrum analyzer, a more sophisticated measurement setup must be used. This method measures the test oscillator again against a reference oscillator, as in the case of the spectrum analyzer, and like the analyzer, requires the phase noise of the reference oscillator to be below or at the

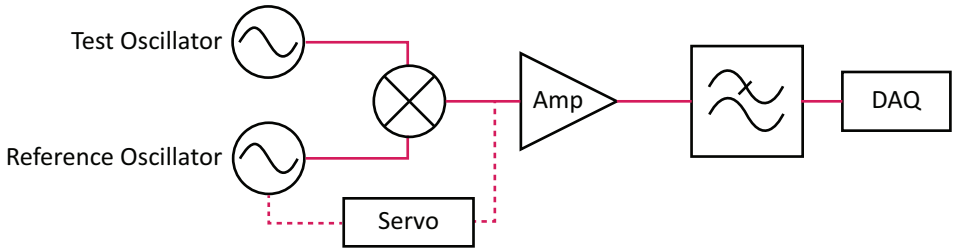

FIGURE C.1. Phase noise measurement block diagram.

noise level of the device under test at the offset of interest. The relative phase of the device under test is measured against the reference oscillator using a double balanced mixer, as shown in the block diagram in Fig. C.1. The mixer produces frequencies at the sum and difference of the two input frequencies, so when the reference and test oscillator have the same nominal frequency, the signal produced by the mixer has components near DC and near twice the oscillator frequency. A low pass filter is employed to give only the DC-centered phase signal. To ensure cancelation of the carrier, the oscillator must be held in quadrature with the reference oscillator. This may be accomplished without active feedback for very stable oscillators and/or short time scales, but to ensure quadrature we will employ a feedback loop to allow the reference oscillator to track the test oscillator.

With $\mathcal{L}(f)$ as the oscillator phase noise in dBc/Hz, and assuming an oscillator power of P_{RF} (in dBm), then the noise power in a 1 Hz band can be given by $P_{\mathrm{SB}}(f) = S(f) + P_{\mathrm{RF}} + K_m$, where the noise figure of the mixer (used here as a phase detector) is approximated by the conversion loss and added on as well. Assuming that the noise PSD is relatively flat over some reasonable filter bandwidth, we can calculate the noise power through the filter by

$$N_P = \int_{f_1}^{f_2} P_{\mathrm{SB}}(f)\,\mathrm{d}f = P_{\mathrm{SB}} \int_{f_1}^{f_2} \mathrm{d}f = P_{\mathrm{SB}}\Delta\mathrm{f} \tag{C.3}$$

where the power is expressed in dBm. Converting noise power to signal,

$$N_S = \sqrt{\frac{10^{N_P/10}}{1000}50} \tag{C.4}$$

where N_s is now in V (assuming a 50 Ω system). This voltage is related to phase through the mixer parameters. We're using a diode-based double balanced mixer, which we require the local oscillator saturate, and thus generate some harmonics. Following the notation from [8], which accounts for infinite harmonics, the temporal signal of the local oscillator is given by

$$V_{\mathrm{LO}}(t) = 2\sum_{n=1}^{\infty} \frac{\sin(n\pi/2)}{n\pi/2} \cos\left(n\omega_{\mathrm{LO}}t + \phi_{\mathrm{LO}}\right) \tag{C.5}$$

The intermediate frequencies are generated by the product of the RF and local oscillator (LO) signals,

$$\begin{aligned} V_{\mathrm{IF}}(t) &= V_{\mathrm{RF}} \cos\left(t\omega_{\mathrm{RF}} + \phi_{\mathrm{RF}}\right) V_{\mathrm{LO}}(t) \\ &= 2V_{\mathrm{RF}} \cos\left(t\omega_{\mathrm{RF}} + \phi_{\mathrm{RF}}\right) \sum_{n=1}^{\infty} \frac{\sin(n\pi/2) \cos\left(nt\omega_{\mathrm{LO}} + \phi_{\mathrm{LO}}\right)}{n\pi/2} \\ &\approx 2V_{\mathrm{RF}} \cos\left(t\omega_{\mathrm{RF}} + \phi_{\mathrm{RF}}\right) \frac{\sin(\pi/2) \cos\left(t\omega_{\mathrm{LO}} + \phi_{\mathrm{LO}}\right)}{\pi/2} \end{aligned}$$

where we're now considering only the first term (which we can easily separate by filtering)

$$\frac{2}{\pi}\left[\cos\left(\phi_{\mathrm{LO}} - \phi_{\mathrm{RF}} + t\omega_{\mathrm{LO}} - t\omega_{\mathrm{RF}}\right) V_{\mathrm{RF}} + \cos\left(\phi_{\mathrm{LO}} + \phi_{\mathrm{RF}} + t\omega_{\mathrm{LO}} + t\omega_{\mathrm{RF}}\right) V_{\mathrm{RF}}\right]. \tag{C.6}$$

After low-pass filtering, the intermediate frequency (IF) is just the RF voltage times the conversion loss, $\frac{2}{\pi} \approx -3.92\text{dB}$, leading to

$$V_{\text{IF}}(t) = \frac{2}{\pi} V_{\text{RF}} \cos\left[t\left(\omega_{\text{LO}} - \omega_{\text{RF}}\right) + \left(\phi_{\text{LO}} - \phi_{\text{RF}}\right)\right]. \tag{C.7}$$

As a phase detector, the voltage/phase slope is given by the derivative of this signal (now with respect to phase), where $\Delta\phi = \phi_{\text{LO}} - \phi_{\text{RF}}$ and the more general conversion loss term, K_m, has been introduced. For degenerate frequencies in quadrature, this can be generally given as

$$V_{\text{IF}} = -K_m V_{\text{RF}} \tag{C.8}$$

in units of V/radian.

The noise sensitivity of the measurement system will be limited by noise from the mixer, the amplifier, and the digitizer. Each components effects the noise level in a rather straightforward way. First the choice of mixer impacts not only the conversion loss of mixer, but also the level (the RF power at which the mixer operates) of the mixer is important. The higher the level of the mixer, the larger the phase to voltage slope will be. The excess conversion loss of the mixer should also be minimized. In this work, we employ a level 7 (Local Oscillator (LO) Power +7 dBm) mixer with a maximum conversion loss of 7 dB for oscillators up to 50 MHz. Noise from the amplifier used to increase the signal level of the filtered mixer signal will also limit the noise performance of the system. The amplifier in this work was an SRS SR560 voltage preamplifier with the gain set to 1000 V/V, a 1 MHz bandwidth, and noise of 4 nV/$\sqrt{\text{Hz}}$.

The measured voltage signal is just given $\delta v = 1/2 V \delta\varphi$, where V is the conversion factor of the mixer from radians to volts. This conversion factor, which is a function of the RF power and

the mixer loss, can be easily measured by tuning the reference oscillator to a frequency very close to the test oscillator and viewing the mixer output on an oscilloscope. The peak-to-peak voltage can then be read off the scope. Once the locking loop is engaged, and the oscillators held at the same frequency in quadrature, the slope will be the same and any (small) phase fluctuations will be converted to voltage through that simple linear relationship. Measuring the power spectrum of δv, and measuring the root mean square of the conversion factor as described above, we can then write [7]

$$\mathcal{L}(f) = 20\log_{10}(\delta v_{\mathrm{rms}}) - 20\log_{10}(V_{\mathrm{rms}}) - 10\log_{10}(f_{\mathrm{BW}}) - 6. \tag{C.9}$$

The final piece of the measurement is the locking loop. The reference oscillator frequency must track the frequency of the test oscillator, requiring the two to be locked together. However, the locking loop will compensate for phase noise within its bandwidth, so the bandwidth of the locking loop must be kept smaller than the smallest frequency offset at which a phase noise measurement is desired.

C.1. Measurement of Phase Noise

Practical considerations complicate the seemingly straightforward measurement of phase noise levels. Each component will impact the noise measurement, introducing noise and distorting the noise spectrum. As the noise measured will be the total noise added by all components, we must measure the noise from each component carefully to ensure that the noise measured is dominated by the noise of the target system, and not simply by the measurement system itself.

To measure the noise added by each component in turn, we start by measuring the noise floor of the component at the end of the chain and adding the other components back in until the full measurement is being made. To start, we terminate the input of the digitizer and measure the noise floor from the digitizer. Then, the input is connected to the output of the low noise amplifier, with the amplifier input terminated, and measure the noise floor of the amplifier and digitizer (making a separate record at each relevant gain setting for the variable-gain amplifier). This value can be compared to the stated noise value from the amplifier manufacturer to ensure that the amplifier is performing within specification.

Then the input of the amplifier is connected to the mixer output, with both mixer inputs terminated. This measurement, through the amplifier, should give the thermal noise of the mixer components along with the noise introduced by the amplifier. This noise floor should be flat, with a value of thermal noise (-174 dBc/Hz for a 0 dBm signal) plus the noise figure of the amplifier.

We then introduce the reference oscillator, connecting the reference oscillator output to both the LO and RF ports of the mixer, choosing cable lengths to ensure the signals are in quadrature. The control voltage of the reference oscillator can be adjusted to tune the reference frequency and correct for slight mismatch in cable length, allowing quadrature to be easily found. This configuration allows the measurement of residual amplitude noise from the oscillator, as the phase noise should be at the noise floor of the measurement system. The LO and RF powers should be attenuated as necessary to match those that will be used in the ultimate experiment.

The noise floor of the phase measurement system is thus measured, allowing higher noise levels to be measured with confidence that they reflect the true noise performance of the

device under test. Excess noise in the measurement system can be minimized by choice of low noise figure amplifiers, as well as high level mixers. The sensitivity of this system will be maximized by choosing as high a level mixer as can be driven by the desired reference oscillator. If insufficient reference oscillator power exists to drive the mixer, another low noise amplifier can be used to allow use of a reasonable mixer. While this amplifier will introduce more noise, it will likely be worth the added noise on the LO to allow the use of a higher level mixer.

The noise floor will also contain some number of spurious signals, sharp peaks at specific frequencies as opposed to a rise in the overall noise level. Many of these spurious signals come from power supplies of the amplifiers, VCO, and servo controllers. These can be eliminated if the component can be run from a battery, though this is only feasible if the component requires relatively low DC power (or has built in battery capability, as is the case of the SR560 amplifier). In this work, the VCO and amplifiers are running on battery power, but there are still a large number of spurious signals due to the servo power supplies.

With the noise floor of the measurement established, we then endeavor to measure a low phase noise source and ensure the noise measured is in reasonable agreement with the expected noise. For this, we choose a crystal oscillator, which offer attractive noise performance at quite a low cost. We select a crystal oscillator with a fixed frequency near our oscillator repetition rate, at about 21 MHz. The reference oscillator is locked to the crystal oscillator and the phase noise measured. As the noise measurement is relative, and the crystal oscillator phase noise is significantly lower than the reference oscillator, the measured noise is dominated by the reference oscillator, producing noise values consistent with the expected values for the reference oscillator. In our experiment, we will lock an oscillator to

the repetition rate our laser, then use an identical oscillator to measure the relative phase shift. To ensure we have reasonable noise performance from both oscillators, we first measure each with respect to the crystal oscillator. The phase measurement system is now well qualified and ready to be used to measure our experimental values.

Closing the loop. With the RF and LO signals conditioned, and the mixer characterized and filtered to provide the difference-frequency error signal, the final step is to monitor the error signal and adjust the local oscillator as necessary to track any drift in the RF frequency. This is accomplished using a servo controller, typically implemented using a Proportional-Integral-Derivative (PID) controller. The PID monitors the error signal, changing the control signals as a response to the current error, the accumulated past error, and the predicted future error. The creation of these three control signals are the function of the three components P, I, and D, in the controller. A weighted sum of these control signals will be fed back to the reference oscillator, causing a change which compensates for the difference between the reference oscillator and the oscillator under test, driving the error signal to zero. If the desired error signal level is non-zero, the error signal may first be summed with a set point voltage, allowing the controller to drive the system to the desired point. Some controllers have this capability built in.

Engaging the servo is as simple as connecting the error monitor signal and the control cables, and monitoring the error signal on an oscilloscope. The gain is set to a low value and the servo loop enabled. The error signal should react to this applied control signal, and the set point can be adjusted such that the error signal under locked conditions is near zero. This low gain configuration is a loose lock, in which the controller compensates for errors over a relatively small bandwidth. If this is desired, as for the phase measurement, then the loop

can be left in this configuration. However, it may be desirable to increase bandwidth. To accomplish this, the gain may be increased while making any necessary small adjustments to the set point.

APPENDIX D

Periodogram Estimation

In the analysis of the noise performance of our measurement system, we've characterized the noise in terms of its PSD. For use of the system, we desire a PSD estimate technique that allows the PSD to be displayed is quasi-real time. We also would like to observe the PSD to low frequencies, as slow fluctuations are of interest in this system. The basic method to perform this spectral estimation (first proposed by [9]), a long time series is collected and divided into a series of temporal buffers. These buffers are individually Fourier transformed and then averaged to arrive at the approximate power spectrum. The sample rate at which the buffers are gathered determines the maximum frequency in the PSD by the Nyquist sampling limit. The lowest frequency that can be resolved is the inverse of the buffer length. The averaging of multiple buffers tends toward the true PSD, with a variance the decreases linearly with the number of buffers averaged (assuming no overlap) [10]. While this technique in principle allows us to observe low frequencies, and the periodogram can be averaged as the are collected, the update still requires the collection and transform of long buffers.

To allow us to use short buffers at high sample rates, allowing rapid display update and computational speed, while still providing a spectral estimate at low frequency, we combine the above technique with cascaded decimation [11]. Following the block diagram shown in Fig. D.1, we estimate the PSD as stated above, but instead of requiring that we collect buffers to average that are as long in time as the inverse of the smallest frequency we'd like to resolve, we instead collect a large number of short buffers that we average. From these consecutive short buffers, we then harvest every Nth point and put them into a new buffer. Prior to this downsampling, a low-pass aliasing filter is employed to remove frequency content above the

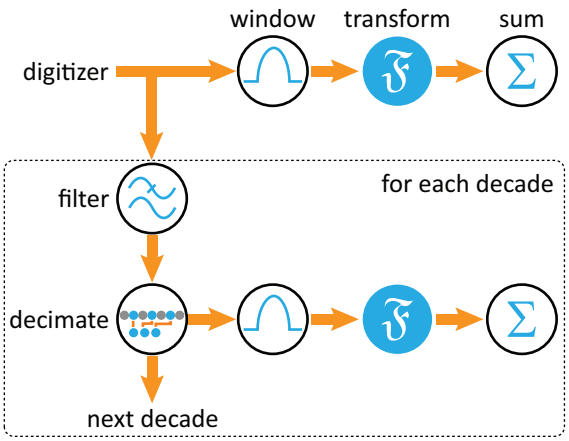

FIGURE D.1. Block diagram of decimation PSD estimation.

effective sample rate. This downsampled buffer is then effectively N times the duration of the short buffer, with a sample rate reduced by N. The reduced buffer is transformed and displayed, providing lower frequency coverage. This process can be repeated, allowing the creation of buffers as long as this process is running. While the resolution of low frequencies will still require long data runs, decimation allows update of the higher frequency data while waiting for the lower frequency data, allows a higher averaging to be done of the fast data relative to the slow data (increasing noise suppression at higher frequencies), and increasing computational efficiency.

The effective sample rate for the decimated buffers is just given by $f_s = f_{s_0}/N^D$, where f_{s_0} is the base sample rate, N is the decimation factor, and D is the decade number. The measured signal is in volts giving an array of samples in volts vs time. The data is then windowed using a Blackman-Harris window before being fourier transformed. The resulting transform gives the power spectrum of the signal, that is, how much power is contained in each frequency of the measured signal. This is more conveniently expressed as a density, which requires simply scaling the power spectrum by the appropriate effective bandwidth for the window used. The

effective noise bandwidth is given by [12]

$$ENBW = f_s \frac{S_2}{S_1^2} \tag{D.1}$$

where f_s is the sample rate, and $S_1 = \sum_{j=0}^{N-1} w_j$ and $S_2 = \sum_{j=0}^{N-1} w_j^2$ are sums of the window and the square of the window, respectively. The power spectrum, PS, can be calculated from the averaged Fourier transforms, S, as

$$PS = \frac{2\,|S|^2}{S_1^2}. \tag{D.2}$$

The PSD is then given by the power spectrum divided by the bandwidth,

$$PSD = \frac{PS}{ENBW}. \tag{D.3}$$

These can be converted to the linear spectral density and linear spectrum by $\sqrt{PSD}$ and $\sqrt{PS}$, respectively.

APPENDIX E

SPIFI Mask Generation

The masks used in SPIFI were printed by one of three companies: MAM-A, Inlight or Photosciences. The different mask producers had different requirements for the data files used for printing. MAM-A is a Compact Disc (CD) replication company that printed using a 400 Dots Per Inch (DPI) thermal printer on polycarbonate CD blanks and required a raster image file. Inlight is a theater lighting company, who printed aluminum on glass disks at 3600 DPI. They also required a raster image. Photosciences is a lithography company that can pattern a variety of metals on a glass substrate with features as small as 1 μm (25400 DPI). They required a Computer Aided Design (CAD) style vector drawing.

The first step in creating the mask files is determination of the desired mask function. The masks used in SPIFI are radially varying cosines, of the form

$$M(r,\theta) = 1/2 + 1/2\,\mathrm{sign}[\cos(\Delta k r\theta)] \tag{E.1}$$

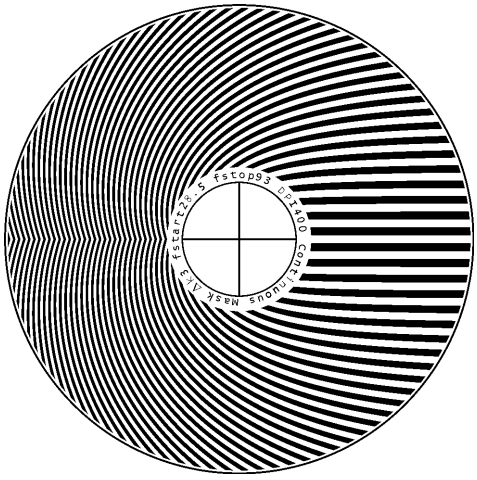

FIGURE E.1. A continuous mask with a Δk = 3/mm and an outer radius of 31 mm.

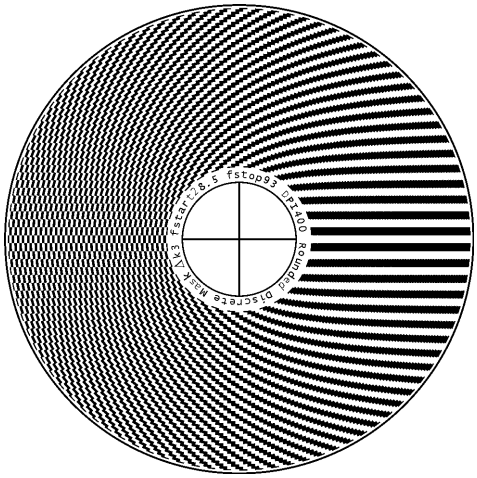

FIGURE E.2. A rounded mask with a Δk = 3/mm and an outer radius of 31 mm.

where Δk describes change in modulation as a function of radius. In this case, the mask chirp rate is continuous, subject only to the resolution of the mask printing. Such a mask is shown in Fig. E.1.

This mask is defined over the angular span of $\pm\pi$, so the there will be a phase jump in the frequencies as the disk rotates. To make a mask without a phase discontinuity, we can simply restrict the frequencies printed on the mask to be integer frequencies. The mask function is then given by

$$M(r,\theta) = 1/2 + 1/2\,\mathrm{sign}\{\cos\left[\mathrm{round}(\Delta k r\theta)\right]\}. \tag{E.2}$$

Such a mask is shown in Fig. E.2.

If simply rounding to the nearest integer frequency yields a mask with more radial bins than are desired, we can artificially restrict the number of bins to a given value N_b. The radial span of the disk is divided by the number of bins to yield the radial width of the desired bins, R_{step}. A new radius is then constructed that is a stepped approximation of the continuous version, defined $R_{\mathrm{bin}} = \mathrm{floor}\left(R/R_{\mathrm{step}}\right)$. The mask is then defined by Eq. E.1, with the replacement $R \to R_{\mathrm{bin}}$. A binned mask with 40 radial bins is shown in Fig. E.3.

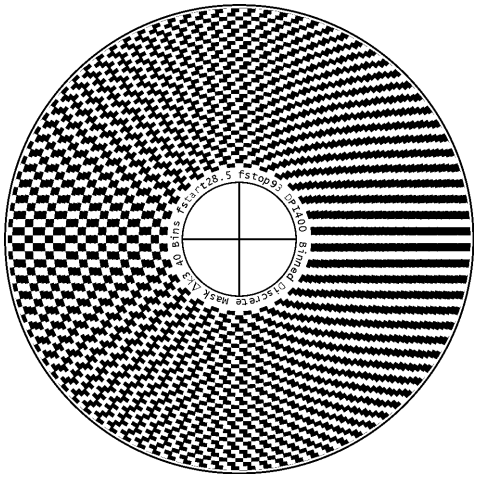

FIGURE E.3. A binned discrete mask with a Δk = 3/mm, an outer radius of 31 mm, and 40 radial bins.

The masks may need to be produced as either raster graphics or as vector graphics (in the form of CAD files, such as Caltech Intermediate Format (CIF) or Drawing Exchange Format (DXF)), depending on the printing technology and printing company being used. The simplest method is producing a raster graphics file, such as a Tagged Information File Format (TIFF) file. To generate a mask using raster graphics, we generate an array of binary values that has the same number of points as the printer has pixels. Each of these pixels will have an x and y coordinate that corresponds to a position in real space through the printer's resolution. The x and y position values are then re-cast into polar coordinates and the radially dependant cosine is then calculated. The array is filled with the cosine values, with the value of 1 being given to positive cosine values and a value of 0 being given to negative cosine values, as the printing process is binary. The mask is trimmed to the inner and outer radii by setting those values to zero as well. Example code is given in section E.1.

To create a vector graphics file, we create the mask as a series of polygons the define areas of the mask where the cosine value is greater than zero. To draw such a polygon, we calculate the edges of these positive regions, then write a file containing the vertices that define this

region and fill the polygon. The example code, given in section E.2, uses the CIF file format commonly used by photolithography companies. The list of vertices created can also be used to create a DXF file. To create the vertices, we proceed by calculating the zeros of the cosine for each period. These could be directly calculated, starting at zero and moving along the edge of the region in steps no larger than the desired resolution, but this approach proved woefully slow. Instead, we create a quantized r axis, being careful to ensure that we have sufficient r resolution such that the spacing between adjacent points on the cosine curve meets or exceeds the desired resolution. From this r vector, we generate the corresponding θ values such that the points lie along the edge of the positive cosine region. Once again, minimum and maximum radii are enforced by rejecting vertices outside the printable area.

E.1. Raster Mask Code

```
% -- Mask Parameters --
Router  = 31;               % (mm) Outer Radius
Rinner  = 8;                % (mm) hole cutout
Rdrill  = 15/2;             % (mm) Drill Size
DPI     = 400;              % (dots per inch) Print Resolution
Dk      = 3;                % (mm^-1) Chirp Rate
PhiMult = 1;                % Number of masks per disk

% -- Axes ------------
DPmm = DPI / 25.4;          % (dots per mm) Print Resolution
N    = 2*Router*DPmm;       % (#) Number of points
x = (-N/2:N/2-1)/DPmm;      % (mm) Horizontal axis
y = (-N/2:N/2-1)/DPmm;      % (mm) Vertical axis
[X, Y] = meshgrid(x,y);     % (mm) Matrices of x & y coordinates
R = sqrt(X.^2+Y.^2);        % (mm) Matrix of radius positions
Phi = atan2(Y, X);          % (rad.) Matrix of angular values
Nbin = 20;                  % (#) Number of radial bins

% -- Phase Wrapping --
Phi = (PhiMult*Phi) + (PhiMult-1)*pi;
while(sum(sum(Phi > pi)))
    Phi(Phi > pi) = Phi(Phi > pi) - 2*pi;
end

% -- Calculate Mask --
switch(maskType)
```

```
    case 'Continuous'
        PhiRadial = Dk*R.*Phi;
    case 'Discrete'
        PhiRadial = floor(Dk*R).*Phi;
    case 'Binned'
        Rspan = Router-Rinner;
        Rstep = Rspan / Nbin;
        RR = floor((R-Rinner)/Rstep)*Rstep+Rinner;
        PhiRadial = floor(Dk*RR).*Phi;
end
Z = round((0.5+0.5*cos(PhiRadial)));

% -- Clipping --------
Z(R < Rinner) = 1;
Z(R > Router) = 1;
```

E.2. Vector Mask Code

```
%--- Mask Parameters ---------------------------------------------
OD = 120;                           % Outer Diameter, mm
ID = 20;                            % Inner Diameter, mm
dk = 5;                             % Radial Chirp, 1/mm
N    = 2^8;                         % Number of r Points
qMax = pi-0.0;                      % Theta Max. (pi-Gap Width)
R = linspace(ID/2, OD/2, N);        % Radial Coordinate, mm
NumQ = ceil(dk*max(R)/2);           % Approx. Number of Patches
q = 0;

%--- Open CIF File -----------------------------------------------
tfWriteCIF = false;
if (tfWriteCIF)
    fName = fopen(sprintf('SPIFI_Mask_Dk%f.cif',dk),'w');
    fprintf(fName,'L L1;\n');
    fprintf(fName,'(Layout definition:);\n');
    fprintf(fName,'DS1 1 1;\n');
end

%--- Make Patches! -----------------------------------------------
for(iq=-NumQ : NumQ)
    q = 2*pi*iq;
    RR = [R;R];
    qq = [
        (q+pi/2)./(dk*R)
        (q-pi/2)./(dk*R)
        ];
    if((all(qq > qMax)) | (all(qq <-qMax))) continue; end;
    RR(2,:) = fliplr(RR(2,:));
    qq(2,:) = fliplr(qq(2,:));
    qq = reshape(qq',[],1);
```

```
    RR = reshape(RR',[],1);
    % Reject large angles
    indx = (qq<qMax)&(qq>-qMax);
    RR = RR(indx);
    qq = qq(indx);
    % Write file (or display)
    if (tfWriteCIF)
        fprintf(fName,['P ' sprintf('%.0f ',100000*reshape( ...
            [RR.*cos(qq) RR.*sin(qq)]',1,numel([RR.*cos(qq) ...
            RR.*sin(qq)]))) ';\n']);
    else
        patch(RR.*cos(qq), RR.*sin(qq), [0 0 0]);
    end
end

%--- Finish File ------------------------------------------------
if (tfWriteCIF)
    fprintf(fName,'DF;\n');
    fprintf(fName,'C 1;\n');
    fprintf(fName,'E;\n');
    fclose(fName);
end
```

REFERENCES

[1] H. Chen, G. C. Schatz, and M. A. Ratner, "Experimental and theoretical studies of plasmon-molecule interactions.," *Rep. Prog. Phys.*, vol. 75, no. 9, p. 096 402, Sep. 2012.

[2] S. A. Kirillov, "Dephasing of the v1 vibration of isotopic molecules of carbon tetrachloride," *J. Raman Spectrosc.*, vol. 33, no. 3, pp. 155–159, Mar. 2002.

[3] W. R. Zipfel, R. M. Williams, and W. W. Webb, "Nonlinear magic: multiphoton microscopy in the biosciences," *Nat. Biotechnol.*, vol. 21, no. 11, pp. 1369–1377, 2003.

[4] D. W. Allan, "Statistics of Atomic Frequency Standards," *Proc. IEEE*, vol. 54, no. 2, pp. 221–230, 1966.

[5] "Characterization of Frequency and Phase Noise," in *Rep. 580 Int. Radio Consult. Comm.* 1978, pp. 162–170.

[6] E. N. Ivanov, S. A. Diddams, and L. Hollberg, "Analysis of Noise Mechanisms Limiting the Frequency Stability of Microwave Signals Generated With a Femtosecond Laser," *IEEE J. Sel. Top. Quantum Electron.*, vol. 9, no. 4, pp. 1059–1065, 2003.

[7] A. Lance, W. Seal, and F. Labaar, "Phase noise and AM noise measurements in the frequency domain," *Infrared Millim. waves.*, vol. 1984, no. 11, pp. 239–289, 1984.

[8] W. A. Davis, "RF Mixers," in *Radio Freq. Circuit Des.* John Wiley & Sons, 2011, ch. 11, pp. 289–354.

[9] M. Bartlett, "Smoothing Periodograms from Time-Series with Continuous Spectra," *Nature*, vol. 161, no. 187, pp. 686–687, 1948.

[10] P. D. Welch, "The Use of Fast Fourier Transform for the Estimation of Power Spectra: A Method Based on Time Averaging Over Short, Modified Periodograms," *IEEE Trans. Audio Electroacoust.*, vol. 15, no. 2, pp. 70–73, 1967.

[11] D. Wight and F. Bostick, “Cascade decimation–A technique for real time estimation of power spectra,” in *IEEE Int. Conf. Acoust. Speech, Signal Process.*, 1980, pp. 626–629.

[12] G. Heinzel, A. Rüdiger, and R. Schilling, “Spectrum and spectral density estimation by the Discrete Fourier transform (DFT), including a comprehensive list of window functions and some new flat-top,” 2002.

LIST OF ABBREVIATIONS

AOD Acousto-Optic Deflector 93, 94, 113

AOM Acousto-Optic Modulator 11, 12

BGO Bismuth Germanium Oxide ($Bi_4Ge_3O_{12}$) viii, ix, 23–25, 47, 48

CAD Computer Aided Design 141, 143

CARS Coherent Anti-Stokes Raman Scattering 6, 7, 149

CCD Charge-Coupled Device 51, 65, 102

CD Compact Disc 141

CHIRPED Coherent Holographic Imaging by Recovered Phase from Emission Distributions vii, 88, 101–103, 114

CIF Caltech Intermediate Format 143, 144

CMOS Complementary Metal–Oxide–Semiconductor 51

CMRR Common-Mode Rejection Ratio 23

CSRS Coherent Stokes Raman Scattering 6

CW Constant Wave 11, 13, 24, 64, 66, 67, 99

DAQ Data Acquisition 23, 25

DC Direct Current 73, 74, 76, 77, 131, 136

DMD Digital Micromirror Device vi, x, xi, 93, 94, 96–100, 114

DPI Dots Per Inch 141

DXF Drawing Exchange Format 143, 144

FBG Fiber Bragg Grating 19

FFT Fast Fourier Transform 83

FM-CARS Frequency-Modulated CARS 7

FPGA Field-Programmable Gate Array 114

FROG Frequency Resolved Optical Gating 67

FWHM Full Width at Half Maximum 65

GDD Group Delay Dispersion ix, 29, 31, 32, 47

ISRS Impulsive Stimulated Raman Scattering 7

LO Local Oscillator 133, 135–137

LPSVD Linear Prediction Singular Value Decomposition 24, 25, 46

MIR Mid-Infrared x, 64, 66, 67, 113

NA Numerical Aperture 58, 108, 109

OCT Optical Coherence Tomography 11, 14

OSA Optical Spectrum Analyzer 1, 23

PID Proportional-Integral-Derivative 137

PLL Phase Locked Loop ix, 36, 37, 41, 43–49

PMT Photomultiplier Tube 109

PSD Power Spectral Density 43, 138, 140

RF Radio Frequency 12, 17, 39, 41, 42, 45, 46, 50, 62, 129, 133, 135, 137

RMS Root Mean Squared 36, 37

SLM Spatial Light Modulator 102

SPIFI Spatial Frequency Modulation for Imaging vi, ix–xi, 51–57, 59–72, 74, 75, 78, 84–86, 88, 90–93, 96, 99, 101, 102, 108, 113, 114, 141

SRG Stimulated Raman Gain 6

SRL Stimulated Raman Loss 6

SRS Stimulated Raman Scattering 6

TIFF Tagged Information File Format 143

USAF U.S. Air Force xi, 99

VCO Voltage Controlled Oscillator 42, 43, 45, 49, 112, 136

XGA Extended Graphics Array 98